



## Numerical Study of Ship Performance in Calm Water and in Waves

Mikkelsen, Henrik

*Publication date:*  
2021

*Document Version*  
Publisher's PDF, also known as Version of record

[Link back to DTU Orbit](#)

*Citation (APA):*  
Mikkelsen, H. (2021). *Numerical Study of Ship Performance in Calm Water and in Waves*. Technical University of Denmark. DCAMM Special Report No. S304

---

### General rights

Copyright and moral rights for the publications made accessible in the public portal are retained by the authors and/or other copyright owners and it is a condition of accessing publications that users recognise and abide by the legal requirements associated with these rights.

- Users may download and print one copy of any publication from the public portal for the purpose of private study or research.
- You may not further distribute the material or use it for any profit-making activity or commercial gain
- You may freely distribute the URL identifying the publication in the public portal

If you believe that this document breaches copyright please contact us providing details, and we will remove access to the work immediately and investigate your claim.

# Numerical Study of Ship Performance in Calm Water and in Waves

Henrik Mikkelsen

PhD Thesis



# Numerical study of ship performance in calm water and in waves

Henrik Mikkelsen

*Technical University of Denmark  
Department of Mechanical Engineering  
Section for Fluid Dynamics, Coastal and Maritime Engineering*





*Published in Denmark by*  
Technical University of Denmark

Copyright © Henrik Mikkelsen 2021  
All rights reserved

Section for Fluid Mechanics, Coastal and Maritime Engineering  
Department of Mechanical Engineering  
Technical University of Denmark  
Niels Koppels Allé, Building 403, DK-2800 Kgs. Lyngby, Denmark  
Phone +45 45 25 19 60, Telefax +45 45 25 19 61  
WWW: <https://www.mek.dtu.dk/>

Publication Reference Data  
Mikkelsen, H.

Numerical study of ship performance in calm water and in waves

PhD Thesis

Technical University of Denmark

Department of Mechanical Engineering

December, 2021

ISBN: 978-87-7475-667-5

**Keywords:** CFD, Speed trial validation, Self-propulsion simulation, Hull Roughness, Added resistance in waves, Oblique waves, Wake field in waves



# Preface

## Ph.D. project and thesis

This thesis is submitted in partial fulfillment of the requirements for obtaining the PhD degree from the Technical University of Denmark.

The work has been carried out over the period July 1, 2018 - December 3, 2021. The work has mostly been performed in the section for Fluid Mechanics, Coastal and Maritime Engineering under the supervision of Professor Jens H. Walther, Associate Professor Yanlin Shao and Dr. Henrik O. Madsen. The period January 2, 2019 - April 20, 2019 was spent as an external stay at the Section for hydrodynamics and stability in DNV GL in Høvik in Norway under the supervision of Dr. Cosmin Ciortan. The research is funded by the Danish Maritime Fund under grant 2018-11.

## List of publications

The thesis is based on the work contained in the following papers:

**Paper A:** Mikkelsen, H. and Walther, J. H. (2020) Effect of roughness in full-scale validation of a CFD model of self-propelled ships. *Appl. Ocean Research* 99, 1-14.

**Paper B:** Mikkelsen, H., Shao, Y. and Walther, J. H. (2021) CFD verification and validation of added resistance and seakeeping response in regular oblique waves with varying wave length. *MARINE 2021 Computational Methods in Marine Engineering IX*, page number 1-24.

**Paper C:** Mikkelsen, H., Shao, Y. and Walther, J. H. (2021) Numerical study of nominal wake fields of a container ship in oblique regular waves. *Accepted by Appl. Ocean Research (In production)*

## Authorship declarations

For paper A, B, and C, H. Mikkelsen has performed the majority of the work including, designing the research, conducting the CFD simulations, analyzing the results, creating the figures, writing the manuscript, and implementing the comments from the other authors.

## Conferences and additional publications

The results obtained during the Ph.D. project were presented at a number of national and international conferences and resulted in the following conference contributions. An oral presentation was given by the H. Mikkelsen unless otherwise specified.

- Mikkelsen, H. and Walther, J. H. (November 2019) Effect of surface roughness on numerical modeling of a full-scale self-propelled ship. *The 72nd Annual Meeting of the American Physical Society's Division of Fluid Dynamics*. Seattle, USA.

- Mikkelsen, H. and Walther, J. H. (November 2020) Prediction of Full Scale Ship Performance Using Computational Fluid Dynamics and Model Tank Tests. *The Danish Society for Industrial Fluid Dynamics Research seminar 2020*. Copenhagen, Denmark.
- Mikkelsen, H., Shao, Y. and Walther, J. H. (November 2020) CFD verification and validation of added resistance in oblique waves. *The 73rd Annual Meeting of the American Physical Society's Division of Fluid Dynamics*. Chicago, USA.
- Mikkelsen, H., Shao, Y. and Walther, J. H. (June 2021) CFD verification and validation of added resistance and seakeeping response in regular oblique waves with varying wave length. *MARINE 2021 Computational Methods in Marine Engineering IX*. Edinburgh, UK.

## Acknowledgements

First and foremost, I would like to extend my sincere thanks to my main supervisor Jens H. Walther. It has been an honor being supervised by you on and off for the last 10 years. Furthermore, I am very grateful for the freedom you allowed me to pursue my own ideas during the PhD project. I would also like to thank my co-supervisors Yanlin Shao and Henrik O. Madsen. It has been a privilege having leading experts available for technical discussions.

I also wish to thank The Danish Maritime Fund for funding the project. Many thanks to Cosmin Ciortan, Olav Rognebakke, Jaecouk Sun, Daniel Nordås, Eivind Ruth, Tormod Gjestland and the rest of the Hydrodynamic section in DNV GL for invaluable insight into CFD and the maritime industry.

Special thank to the shipyard, who shared rare and unique data with me. Thanks also to Jakob Roar Bentzon and Seyed Saeed Asadzadeh for making the time at the office fun and interesting. I would also like to thank the rest of my colleagues at the Section for Fluid Mechanics, Coastal and Maritime Engineering for many good technical discussions and support. Thanks should also go to Ruth Svane Vestergaard. Without her, the section would not have been functioning well.

I would also like to thank my wife Charlotte for the endless patience and support. Without her, I would never have been able to do my thesis. Finally, I would like to thank my son Benjamin for teaching me to work intensively and efficiently in the slots he allowed me to work.

Henrik Mikkelsen

Kgs. Lyngby, December 2021

# Abstract

Traditionally, most ship hulls are optimized for ideal conditions, where the ships are sailing in calm water with full speed in full load. In the last decade, some ships have been designed for a range of draughts and speeds in calm water. However, there is still a large gap between the ideal conditions the ships are designed for and conditions (waves, wind, currents, hull roughness etc.) the ships will operate in. The target for the thesis is to develop accurate numerical models that can help ship designers narrow a part of this gap.

The main body of this thesis is three papers. The first papers compares the speed/power performance of full-scale CFD simulations, towing tank predictions, and high quality speed trial measurements from six sister vessels. Much research have been conducted comparing model-scale CFD with towing tank results. However, very few studies have compared full-scale CFD with speed trial measurements. The study includes both a ro-ro vessel and a general cargo vessel. The present study finds that including the hull and propeller roughness directly into the CFD simulations by modifying the wall-functions provides more accurate results than the traditional approach of estimating the effect of roughness using an empirical formula.

Today, most ships are designed for sailing in calm water. However, very few ships sail entirely in calm water. Before numerical simulations can be used to predict added resistance in waves and seakeeping responses, a systematic verification and validation is required to ensure the accuracy. The second paper presents such a systematic verification and validation for the KCS container ship in oblique waves. Five wave headings and six wavelengths are studied. The estimated spatial and temporal discretization errors are found by an extensive verification study to be less than 5 %. Results from the verified CFD model are compared with existing potential flow and CFD results from the literature, as well as up to three experimental data sets. The comparison shows that the present CFD results in general show significantly better agreement with the experiments than previously published CFD results.

This CFD set-up is used in the third paper to study how sailing in oblique regular waves influences the nominal wake field of the KCS ship. Five different headings are studied and the waves have a steepness of  $1/60$  and a wave length equal to the ship length. The present study finds that the studied incident waves make the nominal wake field highly transient. Especially the transient bilge vortex and shadow from the skeg have a significant influence on the nominal wake field. The results show that the nominal wake fraction fluctuates up to 39 % of the mean nominal wake fraction for the studied waves. The mean nominal wake fraction is higher than in calm water for all headings besides head sea waves. It is found that the stern quartering sea waves has the maximum mean nominal wake fraction, with a 16 % higher mean nominal wake fraction than in calm water. Finally the study finds that the modified advance angle on the  $r/R = 0.7$  circle in the propeller plane varies 3.5 degrees more in stern quartering than in calm water. This increases the risk of cavitation leading to potential vibrations and loss of propulsive efficiency.

The three papers show that CFD simulations can deliver highly accuracy results, when the CFD simulations are set-up very carefully and systematic verification and validation are conducted. The results from the three papers shows that numerical simulations have a massive potential as useful tools when designing ships for the conditions, the ship will operate in.



# Resumé (In Danish)

Traditionelt er alle skibsskrog optimeret til ideelle forhold, hvor skibet sejler fuldt lastet i stille vand med maksimal hastighed. I det seneste årti, er nogle skibe blevet designet til en operationsprofil med forskellige dybgange og hastigheder. Der er dog stadig stor forskel på de ideelle forhold skibe er designet til og de reelle forhold (bølger, vind, strøm, ruhed af skrog etc.) skibet vil operere i. Formålet med denne afhandling er at udvikle nøjagtige numeriske beregningsværktøjer, der kan hjælpe skibsdesignere med at designe skibe til forhold, der er tættere på de forhold, skibet vil operere i.

Afhandlingen består af tre videnskabelige artikler. Den første artikel sammenligner effektkurverne fra CFD beregninger i fuldskala med modeltankforsøg og højkvalitets søprøvemålinger fra seks søsterskibe. Der er tidligere lavet utallige sammenligningsstudier af CFD beregninger i modelskala og modeltankforsøg, men meget få studier har sammenlignet CFD beregninger i fuldskala og søprøvemålinger. Artiklen i denne afhandling undersøger både et ro-ro skib og et fragtskib. Traditionelt inkluderes effekten af ruheden af skroget og propelleren ved brug af en empirisk formel. Studiet i denne afhandling viser at nøjagtigheden af CFD beregningerne øges signifikant, hvis ruheden af skroget og propelleren inkluderet direkte i CFD beregningen ved at modificere vægfunktionerne.

Langt størstedelen af verdens skibsflåde er optimeret til at sejle i stille vand. Dog er det de færreste skibe der udelukkende sejler i stille vand. Før numeriske beregninger kan bruges til at estimere bevægelser og den ekstra modstand et skib vil opleve i bølger, er det nødvendigt at lave systematiske sammenligningsstudier for at sikre nøjagtigheden og troværdigheden af disse beregninger. Den anden artikel i denne afhandling præsenterer netop sådan et systematisk sammenligningsstudie af KCS containerskibet i forskellige bølgeretninger. I alt undersøges fem bølgeretninger og seks bølgelængder. Den estimerede diskretiseringsfejl i tid og sted er i et omfangsrigt verificeringsstudie fundet til at være under 5 %. Resultater fra den verificerede CFD model er sammenlignet med eksisterende potential flow og CFD resultater fra litteraturen samt op til tre set af eksperimentel data. Sammenligningen viser at de udførte CFD resultater generelt rammer eksperimenterne bedre end de i litteraturen publicerede CFD resultater.

CFD modellen fra ovennævnte studie er brugt i den tredje artikel til at studere hvordan sejlads i forskellige bølgeretninger påvirker det nominelle medstrømsfelt af KCS container skibet. Studiet er lavet i fem bølgeretninger med en regulær bølge med en stejlnhed på  $1/60$  og en bølgelængde lig skibets længde. Studiet viser at den indkommende bølge medfører at medstrømsfelt varierer meget over en bølgeperiode. Især konkluderes det at den tidsvarierende kinningshvirvel har en stor påvirkning på det nominelle medstrømsfelt. Resultaterne viser at det nominelle medstrømskoefficient varierer op til 39 % af den gennemsnitlige medstrømskoefficient for den studerede bølge. Bortset fra i modsø, er den gennemsnitlige medstrømskoefficient højere for alle bølgeretninger end i stille vand. For det studerede skib og bølger, er den maksimale gennemsnitlige medstrømskoefficient fundet til at være, når bølgerne kommer skråt bagfra. Her er den gennemsnitlige medstrømskoefficient 16 % højere end i stille vand. Endvidere viser studiet at den modificerede forspringsvinkel på  $r/R = 0.7$  cirklen i propellerplanen varierer 3.5 grader mere når bølgerne kommer skråt bagfra, end når skibet sejler i stille vand. Dette øger risikoen for kavitation, hvilket potentielt kan medføre vibrationer og reducere af fremdrivningseffektivitet.



De tre artikler viser at CFD beregninger kan levere nøjagtige og brugbare resultater, når CFD modellen opsættes, verificeres og valideres minutiøst. Resultaterne fra de tre artikler viser at numeriske værktøjer har et enormt potentiale som værktøj, når skibe skal designes til de forhold, skibene kommer til at operere i.

# Contents

<b>Abstract</b>	<b>vii</b>
<b>Resumé (In Danish)</b>	<b>ix</b>
<b>1 Introduction</b>	<b>1</b>
1.1 Research motivation . . . . .	1
1.1.1 Full-scale validation . . . . .	1
1.1.2 Sailing in waves . . . . .	2
1.2 The state of the art and theory . . . . .	3
1.2.1 Ship resistance in calm water and in waves . . . . .	3
1.2.2 Scaling of ship resistance from model scale to full scale . . . . .	4
1.2.3 Added resistance in waves . . . . .	8
1.2.4 Wake field when sailing in waves . . . . .	9
1.2.5 CFD simulations of ship resistance . . . . .	10
1.3 Research objectives . . . . .	11
<b>2 Paper A</b>	<b>13</b>
<b>3 Paper B</b>	<b>29</b>
<b>4 Paper C</b>	<b>55</b>
<b>5 Conclusions and future work</b>	<b>91</b>
5.1 Conclusions . . . . .	91
5.2 Future work . . . . .	92



# Chapter 1

## Introduction

This chapter is partially based on the three papers presented in this thesis.

### 1.1 Research motivation

Shipping by sea accounts for an estimated 80 % of the world’s trade and is by far the most energy efficient and environmental friendly mode of transportation (UNCTAD, 2019). Traditionally, the performance of a ship design is predicted by conducting towing tank experiments on a downscaled version of the ship (model scale). This has been the procedure since the first towing tank was built in 1883 (McKenna, Stuart A. et al., 2013). The results from these towing tank tests are then extrapolated to the scale of the actual ship (full-scale). An alternative to model test is numerical simulations of the flow around the ship using Computational Fluid Dynamics (CFD). Fig. 1.1 illustrates a resistance test by both a towing tank and by using CFD. CFD simulations can be performed in full-scale, eliminating scale effects and the need for extrapolation. Furthermore, CFD allows studying conditions, which are very difficult to study in a tank, e.g., sailing in oblique waves. However, a disadvantage of using CFD is the modelling errors e.g., free surface modelling and turbulence models.

#### 1.1.1 Full-scale validation

Verification and validation of CFD models are important in order to obtain accurate and consistent results. Much work has been done on validating model scale CFD simulations by comparing with towing tank measurements, cf. e.g., Kim et al. (2005), which showed good agreement with experimental results of the research ship Kryo Container Ship (KCS). Furthermore, validation workshops have been hosted where the participants submit CFD results to be compared with towing tank results (Larsson et al., 2010, 2015; Hino et al., 2020). The conclusions from these workshops are that carefully conducted CFD simulations can accurately estimate the resistance and performance of model scale ships. The next step is validation of full-scale CFD simulations. However, very few publicly available studies have been conducted due to limited access of accurate validation data. A large contribution to full-scale validation is the Lloyd’s Register (LR) workshop from 2016 (Ponkratov, 2017). However, further research is required, especially related to the influence of hull and propeller roughness. Therefore part of the scope of this thesis is to investigate this. If the research conducted in this thesis can demonstrate that full-scale CFD is sufficiently accurate, then it could change the way the maritime industry predicts the resistance and propulsion of ships in the design phase in the future. Towing tank tests are expensive and waiting time for a slot can be significant. Many design iterations are needed with the increasing demand for fuel efficiency from the shipowners’ contractual requirements and from regulation such as the Energy Efficiency Design Index (EEDI) requirements from the International Maritime Organization (IMO, 2011). Testing of multiple hull designs in the towing tank is very

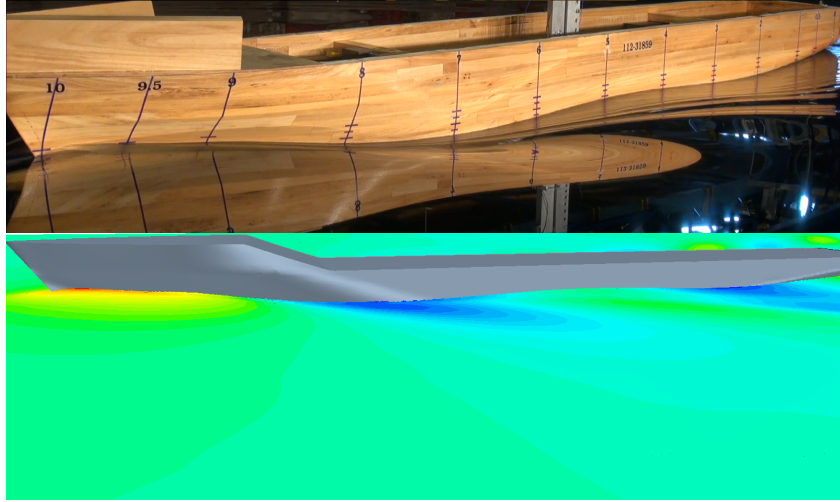


Figure 1.1: Example of resistance test for a container vessel. Top: Towing tank (©FORCE Technology). Bottom: CFD.

time-consuming and costly since a new wooden model needs to be manufactured for each design. When using CFD, the design can be changed very quickly in the CAD software. It can even be done without human interaction if a fully automated design procedure is made by coupling the CFD code with a parametric CAD model and an optimization algorithm tool. The user will only need to specify the design exploration space and one or multiple objectives, such as minimum power for a speed profile or minimum EEDI. After the optimal design has been found, the geometry can be tested and validated in the towing tank.

### 1.1.2 Sailing in waves

For the last decades most commercial ship hulls have been optimized for sailing fully loaded with full speed in calm water. Traditionally, the effects of wind and waves have been included by adding a sea margin of 15 percent (Molland et al., 2011) to the required engine power. Over the last 10 years, this single design point approach has started to change by including more draughts and speeds into the design matrix (Psaraftis and Kontovas, 2014). This has narrowed the gap between the conditions ships are design for and the conditions the ships will operate in. However, almost all ship hulls are still designed using a combination of experience, towing tank tests and CFD, mostly in calm water. The next natural step is to include the influence of interaction with waves into the ship hull design phase. Since almost no ships are constantly sailing in calm water, optimizing the ship hull to realistic sea states in the future has significant potential to reduce fuel costs and emissions. Seakeeping tests of motion responses and added resistance in towing tanks can be expensive, time demanding and dependent on the availability of the tanks. If numerical approaches are verified and validated to become trustworthy, they could be used with confidence in the design phase of new ship hulls. Since numerical simulations only require an available computer and not a large manufactured wooden ship model or a free towing tank slot, ship designers can easily test the seakeeping capabilities of tens or hundreds of ship hulls in the design phase. The knowledge of a ship's seakeeping properties is also important from both a comfort and safety point of view. Most often, the comfort limit is reached before the motion limit for safety, especially for passenger ships. For non-passenger ships, comfort limits related to ship motions in waves are not as strict. For these ships, the safety can sometimes be the limiting factor, e.g., for container ships, where containers can fall into the sea, if motions become too large as illustrated in Fig. 1.2. However, the added resistance in waves are important for all ships, since the added resistance increases fuel consumption and potentially limits the ship speed.



Figure 1.2: Example of container ship, which lost 1,816 units overboard after the vessel encountered severe weather on Monday, November 30, 2020 (©Maritime Bulletin).

Most seakeeping and added resistance research has been focusing on head waves by e.g., Sadat-Hosseini et al. (2013); Kim et al. (2017); Park et al. (2016). Fewer validation studies have been conducted in oblique waves by e.g. Fujii and Takahashi (1975); Valanto and Hong (2015); Park et al. (2019); Sadat-Hosseini et al. (2015). Studying the ship-wave interaction in oblique waves is important in order to quantify the added power and maneuverability in a realistic sea.

The majority of the published studies of ships sailing in oblique waves, focused on the seakeeping, maneuvering and added resistance. Very few studies focused on how the sailing in oblique waves influences the operation of the propeller, even though the propeller is a crucial part of the ship. The starting point when considering the operation of the propeller is the wake field, i.e. the flow field in the propeller disk. A few studies have investigated wake fields in waves by e.g., Longo et al. (2007); Wu et al. (2020); Kim et al. (2021); Saettone et al. (2020). However, these are only for head and following waves. To the best of the author's knowledge, no systematic study investigating the nominal wake field in multiple headings has been published. Therefore, a part of the scope of this thesis is to study how the nominal wake field is influenced by sailing in oblique waves.

## 1.2 The state of the art and theory

### 1.2.1 Ship resistance in calm water and in waves

The total resistance of a ship consists of two contributes. Firstly, the pressure resistance, which is the integrated forces normal to the hull. Secondly, the frictional resistance, which is the integrated forces tangential to the hull. From an energy perspective, the total resistance can also be split into the wave resistance, which is the energy lost in the wave pattern, and the viscous resistance, which is the energy lost in the wake (Molland et al., 2011). In calm water, the wave resistance, also called wake-making resistance is caused by the created Kelvin waves. When a ship is sailing in incident waves, the total resistance of ship is often higher than in calm water. This additional resistance or added resistance in waves consists of the three contributes: radiation, diffraction and viscous effects (Pérez Arribas, 2007). The radiation and diffraction effects by the ship cause a drift force, which is second order in terms of wave steepness in nature (Faltinsen, 1993). For relatively longer waves where ship motions are large, is mainly caused by the wave radiation from the ship motions. This contributor is significant in the resonance region,

where the incident wave encounter frequency is similar to the natural frequencies of the ship causing large motions. The diffraction force is significant, when ship motions are small, which is often the case in short waves. The third contributor is the viscous effects, which is also called the damping forces. This contributor is often small compared to the two other contributions.

### 1.2.2 Scaling of ship resistance from model scale to full scale

When conducting towing tank tests of ships, a scaled down model of the ship is used. Since it is practically impossible to keep the Reynolds number  $Re = \frac{UL}{\nu}$  constant from model-scale to full-scale, an artificial decoupling of the pressure and frictional resistance is required, when scaling the ship resistance. Opposite to the Reynolds number, the Froude number  $Fn = \frac{U}{\sqrt{gL}}$  is kept constant. By keeping the Froude number constant from model scale to full scale, the generated wave pattern and the non-dimensional wave making resistance is the same. The International Towing Tank Committee (ITTC) provides guide lines how the extrapolation from model-scale to full-scale can be made (ITTC, 2021). The fundamental principal of the artificial decoupling of the pressure and frictional resistance is used by all towing tanks. However, each towing tank has their own extrapolation procedure. One of the challenges of the extrapolation procedure is the hull and propeller roughness of the full scale ship, which cannot be assumed smooth. The resistance from surface roughness is very important. Even for new ships with little or no biofouling, the paint roughness, welding seams, variation in plate thickness etc. increase the hull resistance. The traditional approach is using empirical formulas to predict the roughness and apply it as a concentrated point force. The alternative method is to account for the surface roughness by modifying the wall functions in the turbulence model as proposed by Cebeci and Bradshaw (1977). By modifying the wall functions, the boundary layer thickness is increased, which increases the wake fraction as shown by Song et al. (2019). A validation study in model scale by Song et al. (2019) showed good agreement between the CFD with modified wall functions and a towing tank experiment of a ship with a rough hull. The effect of biofouling has been studied by Song et al. (2020), who used CFD to study the effect of biofouling on the self-propulsion parameters and propulsive efficiencies. In full-scale, the roughness on most areas of the hull and propeller cannot be assumed smooth. Paper A presented in Chapter 2 studies the effect on roughness, when validating full-scale CFD simulations. Since it is computationally impractical to include the discrete roughness elements into the CFD simulation and mesh, the effects of hull roughness has to be implemented using a different approach. Paper A presented in Chapter 2 uses two different approaches, which are explained in the following section.

#### Inclusion of surface roughness

One approach is to estimate the roughness resistance using empirical formulas and apply it as a point force in the center of gravity. The first widely used correlation formula was proposed by Bowden and Davison (1974):

$$\Delta C_{F,Bowden-Davidson} = \left[ 105 \left( \frac{AHR}{L_{WL}} \right)^{\frac{1}{3}} - 0.64 \right] \times 10^{-3} \quad (1.1)$$

where  $\Delta C_{F,Bowden-Davidson}$  is the correlation factor and AHR is the average hull roughness. If there are no measured data, ITTC recommends using  $AHR = 150 \mu\text{m}$  (ITTC, 2008).

The Bowden-Davidson correlation formula includes both the effect of roughness and a general model-ship correlation. The formulae is based on thrust and roughness measurements on 14 ships. Hence, Bowden and Davison (1974) calculated the discrepancy between the sea trial measurements and the model tank prediction using six different form factor methods. For each form factor method, a fitted mean curve describing the relation between the discrepancy and the measured hull roughness was found based on the 14 measurements. A final correlation was

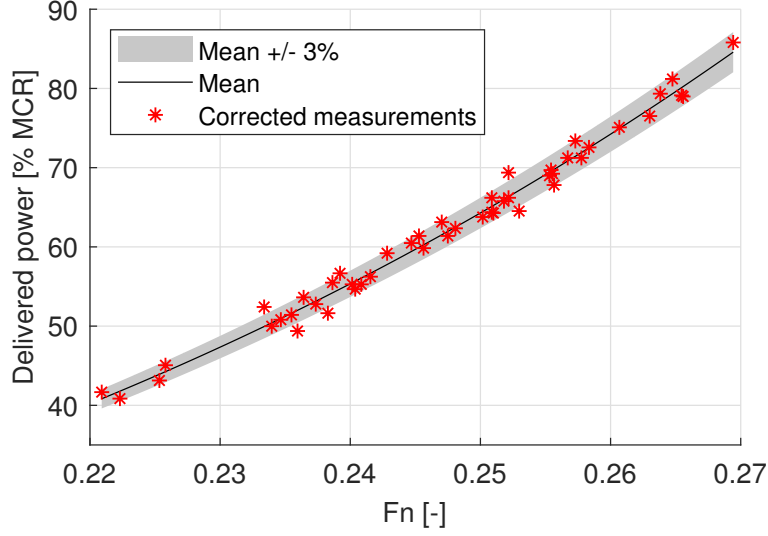


Figure 1.3: Corrected speed trial measurements for the six ro-ro vessels including mean curve presented in Paper A.

found as the mean of the six mean curves illustrated in Fig. 1.3. The relation for this final mean curve is the relation shown in Eq. (1.1). Townsin and Mosaad (1985) proposed the following new empirical relation which only includes the effect of roughness:

$$\Delta C_{F,Townsin} = 0.044 \left[ \left( \frac{AHR}{L_{WL}} \right)^{\frac{1}{3}} - 10 \times Re^{-\frac{1}{3}} \right] + 0.000125 \quad (1.2)$$

The correlation factor ( $C_A$ ) accounts for everything not included in the extrapolation procedure, e.g., 3D-effects and scaling effects. The Townsin formulas ( $\Delta C_{F,Townsin}$  and  $C_A$ ) replaced the Bowden-Davidson formula in the ITTC-recommended procedure in 2008. The definition of  $C_A$  as formulated by ITTC (ITTC, 2008) is:

$$C_A = (5.68 - 0.6 \log(Re)) \times 10^{-3} \quad (1.3)$$

It should be noted that based on a questionnaire by ITTC (ITTC, 2017), almost no towing tanks are using the ITTC standard  $C_A$ -value (Eq. (1.3)). Instead towing tanks are mainly using their own  $C_A$  formula or the older Bowden-Davidson formula (Eq. (1.1)). In the latest ITTC conference (ITTC, 2021), ITTC recommends each towing tank to use and maintain their own model-full scale correlation based on systematic comparison between prediction and sea trial test results.

An alternative method is to model the effects of roughness in the CFD calculation by applying a roughness function and modify the wall functions as proposed by Cebeci and Bradshaw (1977). In the logarithmic region of the turbulent boundary layer, the mean velocity profile for a smooth surface is described as:

$$U^+ = \frac{1}{\kappa} \ln y^+ + B \quad (1.4)$$

where  $U^+ = \frac{U}{U_\tau}$  is the non-dimensional velocity in the boundary layer,  $\kappa$  is the von Karman constant equal to 0.42,  $y^+ = \frac{y U_\tau}{\nu}$  is the non-dimensional normal distance to the wall,  $\nu$  is the kinematic viscosity,  $U_\tau = \sqrt{\tau_w / \rho}$  is the friction velocity,  $\tau_w$  is the shear stress at the wall and  $B$  is the smooth wall log-law intercept.

The roughness elements on the surface increase the turbulence in the boundary layer. Clauser (1954) showed that the effects of surface roughness results in a downwards shift in



the velocity profile. This downward shift is termed a “roughness function”. Hence, for a rough surface, the mean velocity profile can be described as:

$$U^+ = \frac{1}{\kappa} \ln y^+ + B - \Delta U^+ \quad (1.5)$$

where  $\Delta U^+$  is the roughness function. There is no universal roughness function. Normally the roughness function is determined experimentally for a given flow over a rough surface. The roughness function can be expressed as a function of the roughness Reynolds number  $R_s^+$ , which is defined as:

$$R_s^+ = \frac{R_s U_\tau}{\nu} \quad (1.6)$$

where  $R_s$  is the equivalent sand-grain roughness height. The roughness function used in the present study is proposed by Demirel et al. (2017), based on the experiments by Schultz and Flack (2017), and can be expressed as:

$$\Delta U^+ = \begin{cases} 0, & \text{if } R_s^+ < 3. \\ \frac{1}{\kappa} \ln (0.26 R_s^+)^{p(R_s^+)}, & \text{if } 3 < R_s^+ < 15. \\ \frac{1}{\kappa} \ln (0.26 R_s^+), & \text{if } R_s^+ > 15. \end{cases} \quad (1.7)$$

where  $p(R_s^+) = \sin \left[ \frac{\pi}{2} \frac{\log(R_s^+/3)}{\log(5)} \right]$ . A well-known problem with surface roughness is the difficulty to describe the roughness parameters such as height, density and shape of the roughness elements as one parameter, cf. Leer-Andersen and Larsson (2003). Furthermore, the height, density, and shape of the roughness elements often vary across the surface. Unlike describing the roughness height as the mean roughness height  $R_a$ , root-mean-square  $R_{rms}$  or maximum peak-to-through height  $R_t$ , the equivalent sand-grain roughness height  $R_s$ , which is also denoted  $k_s$ , (Nikuradse, 1933) cannot be directly measured on the surface. Instead,  $R_s$  describes the influence of the surface roughness on the wall-bounded flow and can be found experimentally using a Moody diagram or from literature values. Lindholdt et al. (2015) present an extensive literature study on biofouling on ships and experimental methods used to quantify the drag penalty of the hull coating. They conclude that knowledge about the relation between surface roughness and hydrodynamic drag is very limited. However, the drag penalty from hard macro-fouling is better understood than soft biofouling. In the study presented in Chapter 2, the vessels are newly cleaned and painted, thus hard macro-fouling is unlikely. If some areas of the ship hull get fouling from the time between launch and speed trial, the expected type of biofouling type will be soft. The fouling is especially expected in the vessel side facing the sun and the area near the free surface. Unfortunately, the exact roughness of the vessel and propeller is unknown. This includes the height, shape, skewness and kurtosis of the roughness elements as well as the density and distribution of these on the hull and propeller. Since this is unknown, a literature study on the measured roughness of newly painted ships is conducted. Utama et al. (2017) measured the surface roughness on a newly painted ship hull using a silicone rubber surface imprint. The results of the scanning of the imprint can be seen in Table 1.1. These roughness measurements were a factor of two to three higher than the measurement by Schultz (2004), who measured the roughness of different paint types on plates. For the two silicone paints, the roughness heights are shown in Table 1.1. This significant difference between roughness height on a painted ship and a painted plate could indicate that the paint roughness is highly dependent on the way the paint is applied. A study by Niebles Atencio and Chernoray (2019) who painted three plates with the same paint but with different paint application quality supports this. As seen in Table 1.1, the quality of the paint application has a significant influence on the paint roughness height with a factor of up to ten. Schultz et al. (2015) have conducted a study where three plates were painted with different anti-fouling paints. The plates were exposed to an environment similar to a ship hull. The roughness height was measured before the exposure

Study	Comment	$R_a$ [ $\mu\text{m}$ ]	$R_{rms}$ [ $\mu\text{m}$ ]	$R_t$ [ $\mu\text{m}$ ]
(Utama et al., 2017)	Newly painted ship	41.3	51.9	479.1
(Schultz, 2004)	Painted plates	10–19	13–23	66–142
(Niebles Atencio and Chernoray, 2019)	Optimal airless application		8.5	56
	Poor application		41	214
	Very poor application		85	420
(Schultz et al., 2015)	Clean painted plate	0.4–1.0	0.5–1.2	2.2–4.7
	After 3 months exposure	443–574		
	After 6 months exposure	98–520		
(Usta and Korkut, 2013)	Painted plates	1.8–4.5	2.1–5.2	8.4–18.6

Table 1.1: Comparison of measured roughness heights from various studies.  $R_a$  is the mean roughness height,  $R_{rms}$  is the root-mean-square, and  $R_t$  is the maximum peak-to-through height.

and after three and six months of exposure and a mean roughness height up to  $574 \mu\text{m}$  was measured. The results are shown in Table 1.1, and the roughness heights were for the areas covered by biofouling. The surface coverage of biofilm was between 6.4%–48.2%. A study by Usta and Korkut (2013) measured five plates painted with anti-fouling paint. The surface properties were measured using four different measuring lengths also called "cut-off" in the range from 0.008 mm–2.5 mm. Only the measurements from the 2.5 mm are shown in Table 1.1 since most of the other studies have a cut-off of up to 50 mm. Usta and Korkut (2013) found that the length of the cut-off has an influence on the measured roughness heights with a factor of up to two. The conclusion is similar to the study by Howell and Behrends (2006), who compared surface roughness measurements of anti-fouling coatings from different studies where the cut-off length is available. Howell and Behrends (2006) found that the factor can be even larger than two.

It is not only on the ship hull that surface roughness affects the performance of the vessel. The propeller is also a non-smooth surface where fouling occurs in operation. A CFD study by Owen et al. (2018) showed that roughness significantly decreases the efficiency of the propeller. The influence of roughness on the propeller performance explains why propeller polishing has been a widely used treatment for many years. Based on this literature study it is found that the peak-to-through height  $R_t$  for a newly painted plate or ship is in the range of  $2.2 \mu\text{m}$ – $479.1 \mu\text{m}$ . This range is very wide due to the different types of paint, quality of application and potential underlying imperfections from previous paintings etc.. It is important to mention that the  $R_t = 479.1 \mu\text{m}$  by Utama et al. (2017) is a measurement on a real ship. The other roughness measurements are performed on painted flat plates in the laboratory. The measurements by Utama et al. (2017) are conducted in the dry dock before the launch. From the time the newly painted ship is launched, the ship is moored several months at the quayside for outfitting. During these months, slime starts to develop on the hull increasing the hull roughness. Especially in the areas near the free surface at the side facing away from the quay. When transforming the measurable  $R_t$  to non-measurable  $R_s$ , unfortunately no universal relation is available. The study by Adams et al. (2012) showed that  $R_t$  is approximately equal to  $R_s$  if the surface roughness is a monolayer of closely packed spheres of uniform diameter. The relations are shown in Table 1.2. Schultz (2007) found that the relation between  $R_t$  and  $R_s$  is dependent on the roughness height. For a newly applied paint, Schultz (2007) found that the  $R_t$  is approximately five times larger than  $R_s$ . For very rough surfaces,  $R_t$  and  $R_s$  become equal, cf. Schultz (2007).

Roughness parameter	Estimated $R_s$
$R_a$	$R_s = 5.863R_a$
$R_{rms}$	$R_s = 3.1R_{rms}$
$R_t$	$R_s = 0.978R_t$

Table 1.2: Estimated relation between measured roughness height and equivalent sand-grain roughness height.  $R_a$  is the mean roughness height,  $R_{rms}$  is the root-mean-square,  $R_t$  is the maximum peak-to-through height and  $R_s$  is the equivalent sand-grain roughness height (Adams et al., 2012).

### 1.2.3 Added resistance in waves

One of the first studies of added resistance in waves is by Storm-Tejsen et al. (1973), who conducted added resistance experiments of the series 60 ships. Fujii and Takahashi (1975) compared experiments and strip theory simulations on the S175 container ship. Most seakeeping and added resistance research has been focusing on head sea waves. Added resistance in head sea waves using CFD, has been studied intensively by e.g., Sadat-Hosseini et al. (2013), who numerically studied the KRISO Very Large Crude Carrier 2 (KVLCC2). Kim et al. (2017) have also studied the KVLCC2 using both CFD and 3D potential flow theory. Park et al. (2016) studied the added resistance of a tanker in head sea waves at different drafts using the Salvesen-Tuck-Faltinsen (STF) strip theory (Salvesen et al., 1970) and a B-spline based time-domain Rankine panel method (Kim et al., 2011). Simonsen et al. (2013) and Wu et al. (2020) studied the added resistance of the KRISO Container Ship (KCS) in head sea waves both experimentally and using CFD.

Fewer validation studies have been conducted in oblique waves. Studying the ship-wave interaction in oblique waves is important in order to quantify the added power and maneuverability in a realistic sea, where the waves are seldomly uni-directional. Fujii and Takahashi (1975) experimentally studied the added resistance on the S175 container ship in various headings relative to the incident waves. More recently, experimental studies of the Duisburg Test Case (DTC) and the KVLCC2 were conducted by Sprenger et al. (2016). Valanto and Hong (2015) experimentally tested the added resistance of a confidential cruise ship in seven different headings identifying the  $45^\circ$  heading to give maximum added resistance. Park et al. (2019) investigated the added resistance of a confidential tanker both experimentally and numerically in oblique waves. Both strip theory and a 3D Rankine panel method were used and the 3D Rankine panel method predicted the motion in oblique waves with fair agreement. The accuracy of the 3D Rankine panel method was found to be low in predicting the added resistance. The strip method was overestimating the added resistance significantly. A study by Liu and Papanikolaou (2016) predicted the added resistance in oblique waves with a far-field method using Kochin function for a bulk carrier and the Duisburg Test Case (DTC) container ship with fair agreement with the experiments. In general the agreement between numerical results and experiments were better for the longer waves than the shorter waves. Yang et al. (2019) used a frequency-domain hybrid Higher Order Boundary Element Method (HOBEM) to predict the motion responses and added resistance of different ship types sailing in head and oblique waves. In general, good agreement between numerical and experimental results were found. Liu et al. (2018) studied the wave forces and motions of the DTC ship in oblique waves for a single short wave length. They found that the diffraction and radiation effects have significant influence on the non-linearity of wave forces. Gong et al. (2020) numerically studied added resistance and seakeeping performance of trimarans in oblique waves. The results showed that the trends of the added resistance and motion amplitudes of the trimaran in waves are significantly affected by the wave steepness and wave incident angles, which are also different from those of traditional mono-hull ships. Chuang and Steen (2013) studied the speed loss of a vessel sailing

in oblique waves both numerically and experimentally. They found that the speed reduction due to added resistance and due to steering are at almost the same level for head sea and bow quartering sea conditions for the studied tanker with twin azimuth propulsors. Mousavi et al. (2020) studied the motion responses in two wave headings in oblique irregular using both CFD and a strip theory. Jin et al. (2017) experimentally and numerically studied the wave induced loads and motions on two gas carriers in a regular head wave and an oblique wave, both at zero forward speed. The study found that wave diffraction around the ship becomes less profound and the water depth starts to influence the wave loads and ship motions, when increasing the wave length. The added resistance and motions responses of the S175 container ship in multiple wave headings were studied numerically by Kim et al. (2017). Both 2D and 3D potential-flow methods were used for all headings and CFD was used for head and following seas. The study predicted the sea margin in head sea waves to be 17.2 %. However, none of the above studies systematically compared experimental and numerical results for seakeeping and added resistance for multiple headings and multiple wave lengths. A study by Sadat-Hosseini et al. (2015) presented experiments, potential flow, and CFD computations for added resistance for variable headings and wave lengths for the KCS. However, CFD simulations were only conducted for one wave length. They found that the applied potential-flow method captures the heave and pitch motions well. However, surge, roll, and added resistance were not well predicted for most cases. In general, the accuracy of the CFD simulations was better. The reason why CFD simulations were only conducted for one wave length, is that only one wave length was studied at the Tokyo 2015 CFD workshop (Hino et al., 2020). The Tokyo 2015 CFD workshop had a test case, where participants submitted CFD results of motion responses and added resistance for 5 headings and a single wavelength. Only two participants presented their CFD simulations. The first was Iowa Institute of Hydraulic Research (IIHR) using the CFD code CFDSHIP-Iowa (Sadat-Hosseini et al., 2015). The second was University of Zagreb (UZ) using Naval Hydro Pack (Vukcevic and Jasak, 2016). Both participants showed fair prediction of the motions responses, but the discrepancy of added resistance between the CFD simulations and experiments were up to 100 %. Considering the increasing popularity of CFD modelling in ship hydrodynamics and its potential capacity to model a more complex phenomenon than an ordinary PF approach cannot handle, e.g., water entry and exit, local wave breaking, viscosities etc., there is a strong need of dedicated verification and validation studies for ships in waves with various heading and wave lengths. This will be covered in Paper B in Chapter 3.

#### 1.2.4 Wake field when sailing in waves

Most published studies of the influence of sailing in oblique waves focuses on the seakeeping, maneuvering and added resistance. Very few studies focused on how the sailing in oblique waves influences the operation of the propeller, even though the propeller is a crucial part of the ship. The starting point when considering the operation of the propeller is the wake field, i.e. the flow field in the propeller disk. In the present study only the nominal wake field is considered. The nominal wake field of a ship can be considered to comprise three components: the potential wake, the frictional wake, and the wave-induced wake (Carlton, 2012). CFD simulations offer to include all three of these components. The wave-induced wake is due to the gravity waves generated by the ship and not related to the incident waves. The effective wake field is the nominal wake field including the hull-propeller interaction velocities. The total wake field is the effective wake field including the propeller induced velocities. Regener et al. (2018) showed that the nominal and effective wake fields are quite similar with the axial velocities being slightly higher in the effective wake field.

A few studies have investigated wake fields in waves. Longo et al. (2007) studied the nominal wake of the DTMB model 5415 ship in regular head sea waves using Particle Image Velocimetry (PIV). Wu et al. (2020) investigated the forces, ship motions, and wake field for the KCS model in head sea waves both with and without a propeller. They found that CFD results

agreed well with the experiments. Kim et al. (2021) studied the propulsion coefficients of the KCS numerically and experimentally in regular waves with different headings. Their CFD predicted the stern quartering sea waves as the heading with maximum effective wake fraction. However, their experiments showed that the maximum effective wake fraction was present in following sea waves. The studies by Kim et al. (2021), Longo et al. (2007), and Wu et al. (2020) showed that wake field becomes transient, when the ship was sailing in waves. Transient wake fields are normally not considered in the propeller design phase, since a wake field in calm water was almost entirely steady-state. Two of the main objectives when designing a propeller are maximum efficiency and minimum cavitation. Cavitation can lead to vibration causing discomfort and increased wear. Furthermore, cavitation decreases the propeller thrust and can cause erosion of the blade material. When the wake field becomes transient in waves, it is interesting to investigate how sailing in waves influences the propeller efficiency, cavitation and the propeller-hull interaction. The effective wake fraction was studied by Sanada et al. (2018) and Kim et al. (2021), where simulations and experiments of the added powering of the KCS ship in multiple headings and wave lengths was conducted. Saettone et al. (2020) compared a fully-unsteady and a quasi-steady approach for the prediction of the propeller performance in waves. They found a good agreement between the approaches demonstrating that the less demanding quasi-steady approach can be used to compute the propeller performance in waves. Chuang and Steen (2013) experimentally and numerically studied the speed loss of a 8000DWT tanker in oblique waves. Even though converged speed was not be achieved in every run, due to the limited length of the ocean basin, they found that maximum speed loss occurs when the wave length is equal to the ship length. Saettone et al. (2021) studied experimentally the propulsive factors in following and head sea waves. They found that the effective wake fraction in head sea waves is lower than in calm water and that the effective wake fraction in following sea waves is higher than in calm water.

To the best of the authors' knowledge, no systematic study investigating the nominal wake field in multiple headings had been published before Paper C presented in Chapter 4.

### 1.2.5 CFD simulations of ship resistance

The simulations in this thesis are unsteady Reynolds Averaged Navier-Stokes (URANS) CFD performed with the commercial CFD-code STAR-CCM+ v.2020.1 (Siemens, 2020). STAR-CCM+ discretizes the governing equations using an unstructured finite-volume method. The code is widely used in the marine industry and is well known for its capabilities within marine applications

**Governing equations** The governing equations of an incompressible Newtonian fluid are the Navier-Stokes equations (Ferziger and Peric, 2002):

$$\frac{\partial u_j}{\partial x_j} = 0 \quad (1.8)$$

$$\rho \frac{\partial u_i}{\partial t} + \rho u_j \frac{\partial u_i}{\partial x_j} = -\frac{\partial p}{\partial x_i} + \frac{\partial}{\partial x_j} \left( 2\mu S_{ij} - \rho \overline{u'_j u'_i} \right) + f_i \quad (1.9)$$

where  $u_i$  is the velocity vector,  $t$  is time,  $p$  is pressure,  $\mu$  is dynamic viscosity,  $S_{ij} = \frac{1}{2} \left( \frac{\partial u_i}{\partial x_j} + \frac{\partial u_j}{\partial x_i} \right)$  is the mean strain rate tensor,  $u'_i$  is the turbulent fluctuating part of the velocity, and  $f_i$  is body forces.

In order to close the problem the Reynolds stresses ( $\rho \overline{u'_i u'_j}$ ) are modeled using a linear eddy viscosity model. The linear constitutive relationship (Wilcox, 1998) is:

$$-\rho \overline{u'_i u'_j} = 2\mu_t S_{ij} - \frac{2}{3}\rho k \delta_{ij} \quad (1.10)$$

where  $\mu_t$  is the turbulent viscosity,  $k$  is the turbulent kinetic energy, and  $\delta_{ij}$  is Kronecker's delta function.

In this study the turbulent viscosity is calculated using the realizable  $k$ - $\epsilon$  turbulence model (Shih et al., 1995; Siemens, 2020). The  $k$ - $\epsilon$  model is a two equations model based on the turbulent kinetic energy  $k$  and the turbulent dissipation rate  $\epsilon$  (Wilcox, 1998) where:

$$\mu_t = \rho C_\mu \frac{k^2}{\epsilon} \quad (1.11)$$

where  $C_\mu$  is an empirical constant.

The free surface is resolved using the volume of fluid (VOF) method in STAR-CCM+ (Hirt and Nichols, 1981; Siemens, 2020). Hence, the volume fraction  $\alpha$  is assigned and evolves in time with the following transport equation:

$$\frac{\partial \alpha}{\partial t} + \frac{\partial}{\partial x_j} (\alpha u_j) = 0 \quad (1.12)$$

The transport equation is solved using the High-Resolution Interface Capturing scheme (Muzaferija and Perić, 1997). The effective fluid properties are weighted using the volume fraction:

$$\rho = \alpha \rho_w + (1 - \alpha) \rho_a \quad (1.13)$$

$$\mu = \alpha \mu_w + (1 - \alpha) \mu_a \quad (1.14)$$

where  $\rho_w$  is the density of the water phase,  $\rho_a$  is the density of the air phase and  $\mu_w$  and  $\mu_a$  are the corresponding dynamic viscosities. For all simulations, the schemes for the convective and diffusive terms are 2<sup>nd</sup>-order.

### 1.3 Research objectives

The research objectives of this thesis are:

1. Conduct a full-scale validation of a self-propulsion CFD simulation in calm water.
  - (a) Identify ideal ship yard partner and conduct highly accurate sea trial tests and analyze the data.
  - (b) Develop, verify and validate a full-scale CFD model simulating self-propulsion in calm water.
  - (c) Compare the full-scale CFD results and sea trial results and assess the importance of roughness modelling in the CFD model.
2. Investigate how sailing in oblique waves influences the nominal wake field.
  - (a) Develop, verify and validate a CFD model of a wave basin with regular waves.
  - (b) Develop, verify and validate a CFD model simulating the motion responses and added resistance of a ship in regular waves.
  - (c) Expand the CFD model to include the nominal wake field and verify and validate the results.
  - (d) Analyze the influences of sailing in oblique waves on the nominal wake field.

Research objective 1 is studied in Paper A, which is presented in Chapter 2. Research objectives 2a and 2b are studied in Paper B, which is presented in Chapter 3. Finally, research objectives 2c and 2d are studied in Paper C, which is presented in Chapter 4.



## Chapter 2

### Paper A

# Effect of roughness in full-scale validation of a CFD model of self-propelled ships

The paper entitled "Effect of roughness in full-scale validation of a CFD model of self-propelled ships" is published in Applied Ocean Research:

Mikkelsen, H. and Walther, J. H. (2020) Effect of roughness in full-scale validation of a CFD model of self-propelled ships. *Appl. Ocean Research* 99, 1-14.

The paper is here reproduced with permission from Elsevier, not for further re-distribution or re-use.





Contents lists available at ScienceDirect

Applied Ocean Research

journal homepage: [www.elsevier.com/locate/apor](http://www.elsevier.com/locate/apor)

# Effect of roughness in full-scale validation of a CFD model of self-propelled ships

Henrik Mikkelsen<sup>a</sup>, Jens Honoré Walther<sup>a,b</sup>

<sup>a</sup> Technical University of Denmark, Department of Mechanical Engineering, Nils Koppels Allé, Building 404, 2700 Kgs. Lyngby, Denmark

<sup>b</sup> Swiss Federal Institute of Technology Zurich, Computational Science & Engineering Laboratory, Clausiusstrasse 33, CH-8092 Switzerland

## ARTICLE INFO

### Keywords:

CFD  
Full-scale ship propulsion  
Speed trial validation  
Self-propulsion simulation  
Roughness

## ABSTRACT

This paper presents a comparison of full-scale computational fluid dynamics (CFD) simulations with speed trial measurements for a ro-ro vessel and a general cargo vessel. Significant work has been done on validating CFD simulation in model scale. However, in full-scale very few publicly available studies have been conducted due to limited access of validation data. The present study includes extensive validation and verification of both resistance, propeller open-water and self-propulsion simulations in both model and full-scale. The self-propulsion simulations include modelling of the free surface and rotation of the 3D propeller. Full-scale resistance and propeller open-water as well as model scale self-propulsion simulations show good agreement with towing tank measurements and predictions. However, the full-scale self-propulsion simulations using the traditional approach of including the roughness as a point force estimated by an empirical formula significantly underestimate the power from the speed trial measurements. By including the effect of hull and propeller roughness directly into the CFD model, by modifying the wall functions, the discrepancy between CFD and speed trial measurements decreases significantly. This indicates that inclusion of a roughness model directly into the CFD simulation could be a more accurate method than the traditional approach of using empirical formulas originally designed for towing tank extrapolation.

## 1. Introduction

Traditionally, the performance of a ship design is predicted by conducting towing tank experiments on a downscaled version of the ship (model scale). The results from these towing tank tests are then extrapolated to the scale of the actual ship (full-scale). An alternative to testing in a towing tank is to numerically simulate the flow around the ship using computational fluid dynamics (CFD). CFD simulations can be performed in full-scale, eliminating scale effects and the need for extrapolation. However, a disadvantage of using CFD is the modelling errors e.g. free surface and turbulence models.

Towing tank testing is expensive and waiting time for a slot can be significant. Many design iterations are needed with the increasing demand for fuel efficiency from the shipowners' contractual requirements and from regulation such as the Energy Efficiency Design Index (EEDI) requirements from the International Maritime Organization [1]. Testing of multiple hull designs in the towing tank is very time-consuming and costly since a new wooden model needs to be manufactured for each design. When using CFD, the design can be changed very quickly in the CAD software. It can even be done without human interaction if a fully automated design procedure is made by coupling the CFD code with a

parametric CAD model and an optimization algorithm tool. The user will only need to specify the design exploration space and one or multiple objectives, such as minimum power for a speed profile or minimum EEDI. After the optimal design has been found, the geometry can be tested and validated in the towing tank.

Validation and verification of CFD simulations are important. Much work has been done on validating model scale CFD simulations by comparing with towing tank measurements, cf. e.g. Kim et al. [2], which showed good agreement with experimental results of the research ship Krisko Container Ship (KCS). Furthermore, validation workshops have been hosted where the participants submit CFD results to be compared with towing tank results [3,4]. The conclusions from these workshops are that carefully conducted CFD simulations can accurately estimate the resistance and performance of model scale ships. The next step is validation of full-scale CFD simulations. However, very few publicly available studies have been conducted due to limited access of validation data. A large contribution to full-scale validation is the Lloyd's Register (LR) workshop from 2016 [5]. The participants of the workshop blindly submitted twenty-four sets of full-scale self-propulsion calculations. It is important to note that the LR workshop participants used a wide range of methods and some have including

E-mail address: [jhw@mek.dtu.dk](mailto:jhw@mek.dtu.dk) (J.H. Walther).

<https://doi.org/10.1016/j.apor.2020.102162>

Received 7 November 2019; Received in revised form 7 April 2020; Accepted 10 April 2020

0141-1187/ © 2020 Elsevier Ltd. All rights reserved.

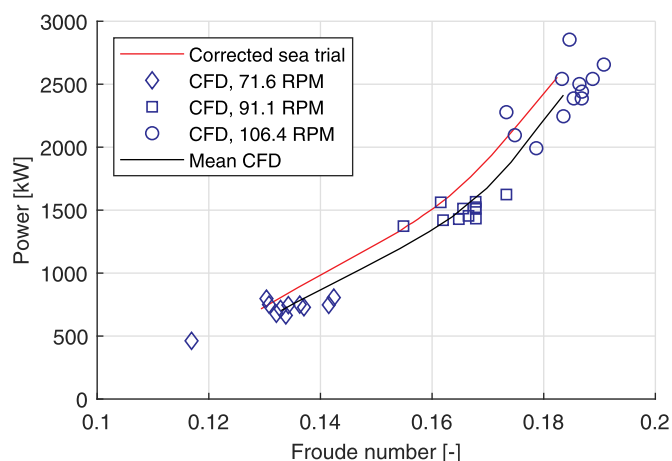


Fig. 1. Comparison of CFD results from workshop participants and speed trial measurements for the LR workshop vessel REGAL.[5]

roughness and air resistance and some have not. The comparison of the submitted CFD results with the speed trial measurements is shown in Fig. 1.

As seen, some of the CFD results show good agreement with the speed trial measurements, and some show large discrepancies. However, in average the CFD simulations underpredict the power. In CFD workshops in model scale [3,4], the participants in general obtain a much more accurate power prediction. The main difference between model-scale and full-scale is the roughness of the hull and propeller, wind loads on the superstructure and the difference in Reynolds number. Another comparison between full-scale CFD and speed trial measurements of a car carrier has been conducted by Jasak et al. [6] using an actuator disc to model the propeller showing apparent good correspondence. For both studies [5,6], the speed trial data were for a single ship. In the present study, the speed trial reference is based on the average of six sister vessels. The conducted self-propulsion CFD simulations in this study include the geometric propeller. A third full-scale validation study conducted by Mikkelsen et al. [7] showed that full-scale CFD and towing tank predictions had similar accuracy in prediction of the delivered power from the speed trial. However, in this study the sea trial power measurement was obtained from an inaccurate engine formula. The study by Sun et al. [8] compares model tank test, CFD simulations and speed trial for a bulk carrier. Both the studies by Mikkelsen et al. [7] and Sun et al. [8] does not resolve the surface. Instead, a double body approach is used and a correction is added for account for free surface effect.

When predicting the full-scale performance of a vessel, the resistance from surface roughness is very important. Even for new ships with little or no biofouling, the paint roughness, welding seams, variation in plate thickness etc. increase the hull resistance. In the present study, the effects of full-scale hull and propeller roughness is implemented and compared using two different approaches, and comparisons will be made. The traditional approach is using empirical formulas to predict the roughness and apply it as a concentrated point force. The alternative method is to account for the surface roughness by modifying the wall functions in the turbulence model as proposed by Cebeci and Bradshaw [9]. By modifying the wall functions, the boundary layer thickness is increased, which increases the wake field fraction as shown by Song et al. [10]. A validation study in model scale by Song et al. [11] showed good agreement between the CFD with modified wall functions and a towing tank experiment of a ship with a rough hull. The effect of biofouling has been studied by Song et al. [12], who using CFD studied the effect of biofouling on the self-propulsion parameters and propulsive efficiencies. To the authors' knowledge, the present study is the first where speed trial measurements are compared with full-scale CFD simulations with geometrically rotating propeller,

Table 1

Principal particulars of the general cargo ship.

Length p.p.	$L_{pp}$	138m
Beam	$B$	23.00m
Draft	$TA/TF$	5.6m/4.9m
Design dead weight	$DW_{scantling}$	16, 890DWT

resolved free surface and hull and propeller roughness modelled using a modified wall function approach.

The paper starts with a short presentation of the studied vessels and measurements in Sec. 2 followed by Sec. 3 describing the methods and CFD set-up in detail. In Sec. 4, the results are presented and discussed. Finally, conclusions are drawn in Sec. 5.

## 2. The studied vessel and measurements

In the present study, two vessels are studied. The main study involves an approximately 200m ro-ro vessel built by a European shipyard where six sister vessels of the same design have been built. Since towing tank tests and speed trial test has been conducted on vessel, it can be used to study resistance, propulsion and scale effects separately. However, only limited data can be shared about this vessel due to confidentiality agreements. To include an open source vessel, a secondary vessel is studied. The secondary vessel is the 138m general cargo vessel REGAL used for the 2016 LR Workshop on Ships Scale Hydrodynamics Computer Simulation [5]. The principal particulars of the vessel are shown in Table 1. The REGAL vessel is to the authors' knowledge the only case where all necessary geometry and speed trial data are publicly available. The general cargo vessel will only be considered in Sec. 4.3.1. The geometries consist of a hull, rudders, and propellers. The ro-ro vessel geometry also consists of appendages.

### 2.1. Hull

The ro-ro hull including rudders and shaft arrangements has been provided as a 3D geometry by the shipyard. The effect of the bilge keel is neglected in the study since it is small for this vessel. The displacement of the vessels during the speed trials condition is approximately 70% of the displacement in the design condition. All comparisons will be conducted in sea trial condition. The vessels are sailing at a Reynolds number  $Re = \frac{UL_{PP}}{\nu}$  of approximately and a Froude number  $Fn = \frac{U}{\sqrt{gL_{PP}}}$  of approximately 0.2 – 0.3, where  $U$  is the vessel speed,  $L_{PP}$  is the length between perpendiculars,  $\nu$  is the kinematic viscosity of the water and  $g$  is the gravitational acceleration.

### 2.2. Propeller

The geometries of the four bladed controllable pitch propellers for the ro-ro vessel used in the towing tank test and the ones manufactured to the actual vessels are slightly different. Both propeller designs have been delivered as a 3D geometry by the propeller manufacturer. The CFD simulations in model scale have been conducted with the propeller geometry used in the towing tank. However, the full-scale CFD simulations have been conducted with the propeller geometry which is used to manufacture the propellers to the actual vessels.

### 2.3. Towing tank testing

Towing tank tests of the vessel have been conducted by Hamburgische Schiffbau-Versuchsanstalt GmbH (HSVA) in Hamburg, Germany. The test types conducted by the towing tank are resistance tests, propeller open-water tests and self-propulsion. The measurements from the towing tank have been extrapolated to full-scale predictions by HSVA using confidential in-house correlations. Only one set of towing tank tests have been conducted for the vessel, since the hull and

propellers are the same for the sister vessels.

#### 2.4. Speed trial

Speed trials have been conducted for each of the six sister vessels. In 2015, IMO and ITTC released ISO15016:2015 [13], which is an updated version of the ISO 15016:2002 standard procedure for carrying out and correcting speed trials. The speed trials of all vessels has been conducted according to the ISO15016:2015 standard [13].

The main measurements at the speed trials are speed, propeller rate of rotation, and the delivered power to the propeller.

##### 2.4.1. Speed measurement and corrections

The speed of the vessel during the speed trial is measured using a GPS. From the GPS data, the ship speed over ground is calculated, and a mean is calculated by assuming no lateral drift.

The wave height and direction were estimated by visual observations and agreed upon on the bridge during the speed trial with representatives from both captain, owner, classification society and yard.

##### 2.4.2. Power measurement and correction

The delivered power is calculated from strain gauges mounted on the shafts. The strain gauges are of the type 3/350LE VY11S-3 by HBM. The strain gauges are mounted for the sole purpose of the speed trial. The mounting and power analysis have been conducted by DNV GL as a third party.

Corrections due to wind, waves, current, water salinity, water temperature and deviating displacement have been conducted after the speed trial as specified in ISO15016:2015 [13].

### 3. Computational fluid dynamics

This section describes the CFD set-ups developed and used in this study. All the CFD simulations are performed in the commercial CFD-code STAR-CCM+ v.2019.1.1 from Siemens [14]. STAR-CCM+ discretizes the governing equations using an unstructured finite-volume method. The code is widely used in the marine industry and is well-known for its capabilities within marine applications.

In total three CFD set-ups are developed: resistance set-up, propeller open-water set-up, and self-propulsion set-up. All set-ups are used in both model and full-scale.

The used computational power and number of cells for calculating one speed for the different test types can be seen in Table 2.

#### 3.1. Governing equations and CFD output

The governing equations of an incompressible Newtonian fluid are the Navier-Stokes equations [15]:

$$\frac{\partial u_i}{\partial x_i} = 0 \quad (1)$$

$$\rho \frac{\partial u_i}{\partial t} + \rho u_j \frac{\partial u_i}{\partial x_j} = -\frac{\partial p}{\partial x_i} + \frac{\partial}{\partial x_j} (2\mu S_{ij} - \rho \overline{u'_j u'_i}) \quad (2)$$

where  $u_i$  is the velocity vector,  $t$  is time,  $p$  is pressure,  $\mu$  is dynamic

**Table 2**

Number of cells and required computational cost for a single simulation. OW is open-water. All simulations are performed on 16-core nodes (Xeon E5-2650 running at 2.60GHz)

Simulation	No. of cells	Comp. cost
Resistance	4.4M	3 hours on 112 cores
Propeller OW	7.5M	30 min on 112 cores
Self-propulsion	10.0M	2 days on 112 cores

viscosity,  $S_{ij} = \frac{1}{2} \left( \frac{\partial u_i}{\partial x_j} + \frac{\partial u_j}{\partial x_i} \right)$  is the mean strain rate, and  $u'_i$  is the turbulent fluctuating part of the velocity.

In order to close the problem the Reynolds stresses are modelled using a linear eddy viscosity model. The linear constitutive relationship [16] is:

$$-\rho \overline{u'_i u'_j} = 2\mu_t S_{ij} - \frac{2}{3} \rho k \delta_{ij} \quad (3)$$

where  $\mu_t$  is the turbulent viscosity,  $k$  is the turbulent kinetic energy, and  $\delta_{ij}$  is Kronecker's delta.

In this study, besides the model scale propeller open-water simulations, the turbulent viscosity is calculated using the realisable  $k - \epsilon$  turbulence model [14,17]. The  $k - \epsilon$  model is a two equations model using  $k$  and the turbulent dissipation rate  $\epsilon$  [16]:

$$\mu_t = \rho C_\mu \frac{k^2}{\epsilon} \quad (4)$$

where  $C_\mu$  is a combination of constants and available flow parameters.

For the propeller open-water simulations in model scale, the actual flow on the propeller blade goes from laminar regime to transitionally turbulent and finally to fully turbulent. The turbulence model is derived assuming a fully turbulent flow. In order to model the influence of transition, the Gamma ReTheta approach is used [14,18]. This adds the two transport equations for the intermittency and transition momentum thickness Reynolds number. The model scale propeller open-water simulations use the  $k - \omega$  SST turbulence model since the transition model Gamma ReTheta only is compatible with the  $k - \omega$  SST.

For all simulations the schemes for the convective and diffusive terms are 2nd-order. For the resistance and self-propulsion simulations, damping is applied on side and outlet boundaries to avoid wave reflections.

All simulations are conducted in calm water. The calm free surface in the resistance and self-propulsion simulations is resolved using the volume of fluid (VOF) method in STAR-CCM+ [14,19]. Hence, the volume fraction  $\alpha$  is assigned and evolves in time with the following transport equation:

$$\frac{\partial \alpha}{\partial t} + \frac{\partial}{\partial x_i} (\alpha u_i) = 0 \quad (5)$$

The transport equation is solved using the High-Resolution Interface Capturing scheme [20]. The effective fluid properties are weighted using the volume fraction:

$$\rho = \alpha \rho_w + (1 - \alpha) \rho_a \quad (6)$$

$$\mu = \alpha \mu_w + (1 - \alpha) \mu_a \quad (7)$$

where  $\rho_w$  is the density of the water phase,  $\rho_a$  is the density of the air phase and  $\mu_w$  and  $\mu_a$  are the corresponding dynamic viscosities.

The solver for the temporal discretization is a first-order scheme, and the convective Courant number is kept below 1 in most of the domain. The heave and pitch motions of the vessel are solved using the Dynamic Fluid Body Interaction (DFBI) model in STAR-CCM+ cf. [14] and is applied as a rigid translation and rotation of the mesh.

The convergence of the simulations has been closely monitored by visual expectation for each simulation. This has been done to ensure that the changes to the solution and the running-means of the results are negligible at the end of the simulation.

The propeller thrust coefficient  $K_T$  is defined as:

$$K_T = \frac{T}{\rho_w n^2 D^4} \quad (8)$$

where  $n$  is the propeller rate of revolution in  $s^{-1}$  and  $D$  is the propeller diameter.

The propeller torque coefficient  $K_Q$  is defined as:

$$K_Q = \frac{Q}{\rho_w n^2 D^5} \quad (9)$$

The propeller open-water efficiency  $\eta_o$  is defined as:

$$\eta_o = \frac{JK_T}{2\pi K_Q} \quad (10)$$

where  $J = \frac{V_A}{nD}$  is the advance ratio, and  $V_A$  is the advance speed. The delivered power  $P$  is calculated as:

$$P = 2\pi nQ \quad (11)$$

### 3.2. Grid convergence index

For the verification study of each CFD set-up, the discretization error is estimated using the Grid Convergence Index (GCI) method [21] which is based on Richardson extrapolation, cf. [22,23]. The apparent order ( $p$ ) is calculated by:

$$p = \frac{1}{\ln(r_{21})} |\ln|\epsilon_{32}/\epsilon_{21}| + q(p)| \quad (12)$$

$$q(p) = \left( \frac{r_{21}^p - s}{r_{32}^p - s} \right) \quad (13)$$

$$s = \text{sgn}(\epsilon_{32}/\epsilon_{21}) \quad (14)$$

where  $r$  are refinement ratios,  $\epsilon_{32} = \phi_3 - \phi_2$ ,  $\epsilon_{21} = \phi_2 - \phi_1$ , and  $\phi_k$  denotes the solution on the  $k$ -th mesh.  $q(p) = 0$  for  $r = \text{const}$ . The extrapolated asymptotic value is calculated as:

$$\phi_{ext}^{21} = \frac{r_{21}^p \phi_1 - \phi_2}{r_{21}^p - 1} \quad (15)$$

Different error estimates can now be calculated. The approximate relative error is:

$$e_a^{21} = \left| \frac{\phi_1 - \phi_2}{\phi_1} \right| \quad (16)$$

The extrapolated relative error is:

$$e_{ext}^{21} = \left| \frac{\phi_{ext}^{12} - \phi_1}{\phi_{ext}^{12}} \right| \quad (17)$$

The GCI for the fine and medium mesh is calculated as follows using the safety factor of 1.25 recommended by Roache [24]:

$$GCI_{fine}^{21} = \frac{1.25 e_a^{21}}{r_{21}^p - 1} \quad (18)$$

$$GCI_{medium}^{32} = \frac{1.25 e_a^{21} r_{21}^p}{r_{21}^p - 1} \quad (19)$$

The GCI value will be used to indicate the discretization error, since the GCI value is a measure of the discrepancy between the computed value and the asymptotic numerical value.

### 3.3. Modelling of roughness on the hull and propeller

In full-scale, the roughness on most areas of the hull and propeller cannot be assumed smooth. The effects of hull roughness are implemented using two different approaches. One approach is to estimate the roughness resistance using empirical formulas and apply it as a point force in the center of gravity. The first widely used correlation formula was proposed by Bowden and Davidson [25]:

$$\Delta C_{F,Bowden-Davidson} = \left[ 105 \left( \frac{AHR}{L_{WL}} \right)^{\frac{1}{3}} - 0.64 \right] \times 10^{-3} \quad (20)$$

where  $\Delta C_{F,Bowden-Davidson}$  is the correlation factor and AHR is the average

hull roughness. If there are no measured data, ITTC recommends using AHR = 150  $\mu\text{m}$  [26].

The Bowden-Davidson correlation formula both includes the effect of roughness and a general model-ship correlation. The formulae is based on thrust and roughness measurements on 14 ships. Hence, Bowden and Davidson [25] calculated the discrepancy between the sea trial measurements and the model tank prediction using six different form factor methods. For each form factor method, a fitted mean curve describing the relation between the discrepancy and the measured hull roughness was found based on the 14 measurements. A final correlation was found as the mean of the six mean curves was found. The relation for this final mean curve is the relation shown in Eq. 20. Townsin and Mosaad [27] proposed the following new empirical relation which only include the effect of roughness:

$$\Delta C_{F,Townsin} = 0.044 \left[ \left( \frac{AHR}{L_{WL}} \right)^{\frac{1}{3}} - 10 \times \text{Re}^{-\frac{1}{3}} \right] + 0.000125 \quad (21)$$

The correlation factor ( $C_A$ ) accounts for everything not included in the extrapolation procedure, e.g. 3D-effects and scaling effects. The Townsin formulas ( $\Delta C_{F,Townsin}$  and  $C_A$ ) replaced the Bowden-Davidson formula in the ITTC-recommended procedure in 2008. The definition of  $C_A$  as formulated by ITTC [26] is:

$$C_A = (5.68 - 0.6 \log(\text{Re})) \times 10^{-3} \quad (22)$$

It should be noted that based on a questionnaire by ITTC [28], almost no towing tanks are using the ITTC standard  $C_A$ -value (Eq. 22). Instead towing tanks are mainly using their own  $C_A$  formula or the older Bowden-Davidson formula (Eq. 20).

In the CFD simulations where the roughness resistance is empirically estimated, Eq. 21 will be used with the recommended roughness height of 150  $\mu\text{m}$ . A correlation allowance  $C_A$  will not be used since the CFD simulations will be conducted in full-scale. The roughness resistance from the empirical formula is added to the ship resistance in the force balance as a concentrated point force. Propeller roughness is not considered when using the empirical formula.

An alternative method is to model the effects of roughness in the CFD calculation by applying a roughness function and modify the wall functions as proposed by Cebeci and Bradshaw [9]. In the logarithmic region of the turbulent boundary layer, the mean velocity profile for a smooth surface is described as:

$$U^+ = \frac{1}{\kappa} \ln y^+ + B \quad (23)$$

where  $U^+ = \frac{U}{U_\tau}$  is the non-dimensional velocity in the boundary layer,  $\kappa$  is the von Karman constant equal to 0.42,  $y^+ = \frac{y U_\tau}{\nu}$  is the non-dimensional normal distance to the wall,  $\nu$  is the kinematic viscosity,  $U_\tau = \sqrt{\tau_w/\rho}$  is the friction velocity,  $\tau_w$  is the shear stress at the wall and  $B$  is smooth wall log-law intercept.

The roughness elements on the surface increase the turbulence in the boundary layer. Clauser [29] showed that the effects of surface roughness results in a downwards shift in the velocity profile. This downward shift is termed a "roughness function". Hence, for a rough surface, the mean velocity profile can be described as:

$$U^+ = \frac{1}{\kappa} \ln y^+ + B - \Delta U^+ \quad (24)$$

where  $\Delta U^+$  is the roughness function. There is no universal roughness function. Normally the roughness function is determined experimentally for a given flow over a rough surface. The roughness function can be expressed as a function of the roughness Reynolds number  $R_s^+$ , which is defined as:

$$R_s^+ = \frac{R_s U_\tau}{\nu} \quad (25)$$

where  $R_s$  is the equivalent sand-grain roughness height. The roughness



function used in the present study is proposed by Demirel et al. [30], based on the experiments by Schultz and Flack [31], and can be expressed as:

$$\Delta U^+ = \begin{cases} 0, & \text{if } R_s^+ < 3. \\ \frac{1}{\kappa} \ln(0.26 R_s^+) \sin \left[ \frac{\pi \log(R_s^+/3)}{2 \log(5)} \right], & \text{if } 3 < R_s^+ < 15. \\ \frac{1}{\kappa} \ln(0.26 R_s^+), & \text{if } R_s^+ > 15. \end{cases} \quad (26)$$

A well-known problem with surface roughness is the difficulty to describe the roughness parameters such as height, density and shape of the roughness elements as one parameter, cf. [32]. Furthermore the height, density and shape of the roughness elements often vary across the surface.

Unlike describing the roughness height as the mean roughness height  $R_a$ , root-mean-square  $R_{rms}$  or maximum peak-to-through height  $R_t$ , the equivalent sand-grain roughness height  $R_s$ , which is also denoted  $k_s$ , [33] cannot be directly measured on the surface. Instead,  $R_s$  describes the influence of the surface roughness on the wall-bounded flow and can be found experimentally using a Moody diagram or from literature values.

Lindholdt et al. [34] present an extensive literature study on biofouling on ships and experimental methods used to quantify the drag penalty of the hull coating. They conclude that knowledge about the relation between surface roughness and hydrodynamic drag is very limited. However, the drag penalty from hard macro-fouling is better understood than soft biofouling.

In the present study, the vessels are newly cleaned and painted and hard macro-fouling is unlikely. If some areas of the ship hull get fouling from the time between launch and speed trial, the expected type of biofouling type will be soft. The fouling is especially expected in the vessel side facing the sun and the area near the free surface.

Unfortunately, the exact roughness of the vessel and propeller is unknown. This includes the height, shape, skewness and kurtosis of the roughness elements as well as the density and distribution of these on the hull and propeller. Since this is unknown, a literature study on the measured roughness of newly painted ships is conducted.

Utama et al. [35] measured the surface roughness on a newly painted ship hull using a silicone rubber surface imprint. The results of the scanning of the imprint can be seen in Table 3. These roughness measurements were a factor of two to three higher than the measurement by Schultz [36], who measured the roughness of different paint types on plates. For the two silicone paints, the roughness heights are shown in Table 3. This significant difference between roughness height on a painted ship and a painted plate could indicate that the paint roughness is highly dependent on the way the paint is applied. A study by Niebles Atencio and Chernoray [37] who painted three plates with the same paint but with different paint application quality supports this. As seen in Table 3, the quality of the paint application has a significant influence on the paint roughness height with a factor of up to

**Table 3**

Comparison of measured roughness heights from various studies.  $R_a$  is the mean roughness height,  $R_{rms}$  is the root-mean-square, and  $R_t$  is the maximum peak-to-through height.

Study	Comment	$R_a[\mu\text{m}]$	$R_{rms}[\mu\text{m}]$	$R_t[\mu\text{m}]$
[35]	Newly painted ship	41.3	51.9	479.1
[36]	Painted plates	10 – 19	13 – 23	66 – 142
[37]	Optimal airless application		8.5	56
	Poor application		41	214
	Very poor application		85	420
[38]	Clean painted plate	0.4 – 1.0	0.5 – 1.2	2.2 – 4.7
	After 3 months exposure	443 – 574		
	After 6 months exposure	98 – 520		
[39]	Painted plates	1.8 – 4.5	2.1 – 5.2	8.4 – 18.6

ten.

Schultz et al. [38] have conducted a study where three plates were painted with different anti-fouling paints. The plates were exposed to an environment similar to a ship hull. The roughness height was measured before the exposure and after three and six months of exposure and a mean roughness height up to  $574\mu\text{m}$  was measured. The results are shown in Table 3, and the roughness heights were for the areas covered by biofouling. The surface coverage of biofilm was between 6.4% – 48.2%.

A study by Usta and Korkut [39] measured five plates painted with anti-fouling paint. The surface properties were measured using four different measuring lengths also called "cut-off" in the range from 0.008mm – 2.5mm. Only the measurements from the 2.5mm are shown in Table 3 since most of the other studies have a cut-off of up to 50mm. Usta and Korkut [39] found that the length of the cut-off has an influence on the measured roughness heights with a factor of up to two. The conclusion is similar to the study by Howell and Behrends [40], who compared surface roughness measurements of anti-fouling coatings from different studies where the cut-off length is available. Howell and Behrends [40] found that the factor can be even larger than two.

It is not only on the ship hull that surface roughness affects the performance of the vessel. The propeller is also a non-smooth surface where fouling occurs in operation. A CFD study by Owen et al. [41] showed that roughness significantly decreases the efficiency of the propeller. The influence of roughness on the propeller performance explains why propeller polishing has been a widely used treatment for many years.

Based on this literature study it is found that the peak-to-through height  $R_t$  for a newly painted plate or ship is in the range of  $2.2\mu\text{m}$  –  $479.1\mu\text{m}$ . This range is very wide due to the different types of paint, quality of application and potential underlying imperfections from previous paintings etc.. It is important to mention that the  $R_t = 479.1\mu\text{m}$  by Utama et al. [35] is a measurement on a real ship. The other roughness measurements are performed on painted flat plates in the laboratory. The measurements by Utama et al. [35] are conducted in the dry dock before the launch. From the time the newly painted ship is launched, the ship is moored several months at the quayside for outfitting. During these months, slime starts to develop on the hull increasing the hull roughness. Especially in the areas near the free surface at the side facing away from the quay. When transforming the measurable  $R_t$  to non-measurable  $R_s$ , unfortunately no universal relation is available. The study by Adams et al. [42] showed that  $R_t$  is approximately equal to  $R_s$  if the surface roughness is a monolayer of closely packed spheres of uniform diameter. The relations are shown in Table 4. Schultz [43] found that the relation between  $R_t$  and  $R_s$  is dependent on the roughness height. For a newly applied paint, Schultz [43] found that the  $R_t$  is approximately five times larger than  $R_s$ . For very rough surfaces,  $R_t$  and  $R_s$  become equal, cf. Schultz [43]. Since the actual roughness of the vessels on the day of the speed trial is not available, CFD simulations are conducted using a range of roughness heights. Based on the literature described above, the chosen roughness heights used in the CFD simulations presented in Sec. 4.3 are  $R_s = 100\mu\text{m}$ ,  $R_s = 120\mu\text{m}$  and  $R_s = 150\mu\text{m}$ . The roughness of the propeller is set to  $R_s = 30\mu\text{m}$  for all simulations presented in Sec. 4.3.

**Table 4**

Estimated relation between measured roughness height and equivalent sand-grain roughness height.  $R_a$  is the mean roughness height,  $R_{rms}$  is the root-mean-square,  $R_t$  is the maximum peak-to-through height and  $R_s$  is the equivalent sand-grain roughness height [42].

Roughness parameter	Estimated $R_s$
$R_a$	$R_s = 5.863R_a$
$R_{rms}$	$R_s = 3.1R_{rms}$
$R_t$	$R_s = 0.978R_t$

### 3.4. Validation and convergence test

It is of uppermost importance to ensure the accuracy of the CFD set-up before conclusions are based on the results of the set-up. In this study, both convergence studies for verification and comparison studies for validation are performed for each CFD set-up. The most important of the convergence studies and comparison studies for the ro-ro vessel are presented in the following sections.

#### 3.4.1. CFD resistance

All resistance simulations are performed in the speed trial condition, as described in Sec. 2.1, similar to the towing tank tests and speed trials. Both the rudders and shafts are included. The initial CFD set-up used to estimate the calm water resistance is an automated CFD set-up originally developed by OSK-ShipTech A/S. The set-up has been developed further in the present study.

In the CFD resistance set-up a number of different physics models are used to model the flow around the ship. Free surface waves are modelled using VOF, as described in Sec. 3.1. The hull is allowed dynamic pitch and heave motions. The simulations are solved using a first-order implicit unsteady solver.

The shape of the domain is a rectangular box. Only one half of the twin screw ro-ro vessel is modelled since the flow is considered to be symmetrical. A test simulation with a larger domain is conducted to ensure that the domain is significantly large to not affect the results. The domain can be seen in Fig. 2 and the boundary conditions can be seen in Table 5. The top and bottom boundaries are inlets, since fluid will flow through these when the pitch is non-zero. The volume mesh consists of hexahedrons in a unstructured grid. The mesh is generated using the trimmer-mesh function in STAR-CCM+. The boundary layer mesh, also called the prism layer mesh, is used on the hull surface in order to ensure accurate estimation of the wall shear stress within the wall function approximation. Fifteen prism layers are used on the ship hull and appendages. The wall  $y^+$  values on the hull are mostly in the range of 50–200. The mesh is refined in the important zones including the free surface, transom, bulbous bow etc.. The mesh on the free surface can be seen in Fig. 3. The full-scale resistance set-up is created by scaling up the model scale resistance set-up with the scaling factor. The boundary layer is changed so the wall  $y^+$  is still mostly in the range of 50–200. The air resistance is calculated using the standard ITTC method, [26], with the recommended drag coefficient of 0.8 and is added to the ship resistance. The magnitude of the air resistance is approximately 5 percent of the total resistance. The drag from the bow thrusters is estimated using the method proposed by ITTC [26] and is added to the ship resistance. The magnitude of the bow thruster drag is approximately 1 percent of the total resistance.

For all resistance simulations, the empirical formula from Townsin (Eq. 21) is used to estimate the roughness resistance which is applied as a point force in the center of gravity. The propeller open-water test using CFD is less complex than modelling the self-propulsion test because the hull-propeller interaction is not included in the propeller open-water set-up.

The single phase propeller open-water set-up uses two domains: a stationary domain and a rotating domain. The two domains are connected by an interface. The shape of the stationary domain is a

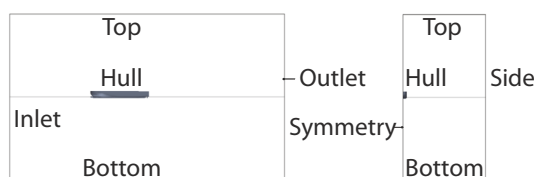


Fig. 2. Domain of the resistance set-up and self-propulsion, with boundary names. Thin line is the free surface. Seen from starboard side (left) and from the front (right).

Table 5

Boundary conditions of the CFD resistance set-up.

Name of boundary	Boundary condition
Inlet	Velocity inlet
Top	Velocity inlet
Bottom	Velocity inlet
Outlet	Pressure outlet
Symmetry	Symmetry plane
Side	Slip wall
Hull	No-slip wall

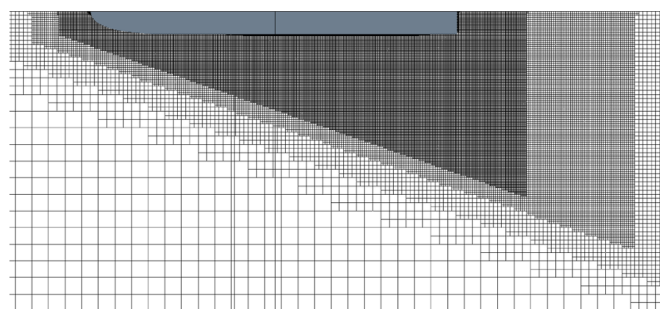


Fig. 3. Close-up of mesh on the free surface for resistance simulation seen from top.

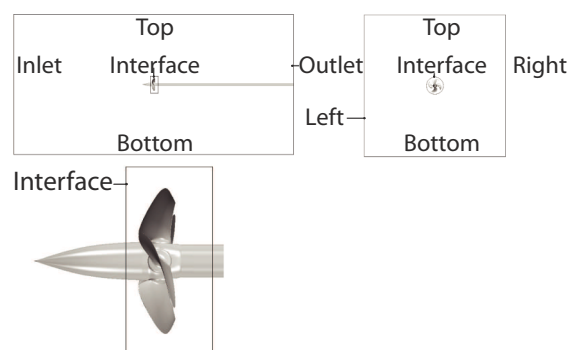


Fig. 4. Domain of the CFD propeller open-water set-up for the ro-ro vessel, with boundary names. Seen from the side (upper left and bottom) and from the front (upper right).

rectangular cubeoid. The shape of the rotating domain is a cylinder which is located inside the static domain and around the propeller. The size of the rotating domain is the same as in the self-propulsion simulation. An illustration of the domains can be seen in Fig. 4 and boundary conditions of the domains are listed in Table 6. The volume mesh in the stationary domain consists of hexahedrons in an unstructured grid. In the rotating domain, the mesh is polyhedral due to the complex propeller geometry. Fifteen prism layers are used on the shaft, blades and hub. In order to better resolve the flow around the propeller, two refinement zones are used to refine the mesh in the volume around the

Table 6

Boundary conditions of the CFD propeller open-water set-up.

Name of boundary	Boundary condition
Inlet	Velocity inlet
Outlet	Pressure outlet
Top	Symmetry plane
Bottom	Symmetry plane
Left	Symmetry plane
Right	Symmetry plane
Interface	Internal interface
Shaft, Blades, Hub	No-slip wall

propeller. In model scale, the rotation rate and advance speed of the propeller in the CFD simulation are equal to the rate of rotation and advance speed used in the towing tank. In full-scale, the rotation rate and advance speed of the propeller is set similar to what the actual ship will experience. The propeller movement can be modelled using two different methods: the moving reference frame method (MRF) or the sliding mesh (SM).

The MRF method works by changing the reference system from a stationary coordinate system to a rotating coordinate system moving with a constant rotational velocity. This is also called a "frozen rotor" approach. SM works by rotating the propeller geometry and surrounding cylindrical mesh region in increments at each new time step. The rotational cylindrical mesh region has a sliding interface to the surrounding stationary mesh. This method requires more computational time, but is a better model of the actual propeller physics compared to the MRF method. The SM method models the hull-propeller interaction while the MRF method does not. Since there is no hull in the propeller open-water simulations, the MRF method is used.

In model scale, the Gamma ReTheta transition model (see Sec. 3.1) is used to estimate the laminar to turbulent transition on the propeller. In full-scale, the transition model is not used since the flow is assumed fully turbulent due to the high Reynolds number. On the inlet boundary condition, the turbulence intensity is set to 1%, and the turbulent viscosity ratio is set to one.

The propeller open-water CFD set-up uses wall functions, and the  $y^+$  values on the propeller are mostly in the range of 100–250 in the full-scale simulations. In model scale the  $y^+$  values on the propeller are mostly below one, which is required when using the transition model.

### 3.4.2. CFD self-propulsion

The self-propulsion set-up is created by combining the verified and validated resistance CFD set-up with the verified and validated propeller open-water CFD set-up. As in the propeller open-water set-up, the domain consists of two domains. The mesh in the stationary domain consists of hexahedrons in an unstructured grid. In the rotating domain, the mesh is polyhedral cells. Using two separate meshes allows mesh settings from the resistance set-up to be used for the static domain and mesh options from the propeller open-water set-up to be used for the rotating domain. The static domain can be seen in Fig. 2. Isotropic mesh refinement zones are used in the self-propulsion set-up to better resolve the flow between the hull and propeller. The mesh near the aft ship can be seen in Fig. 5. The boundary conditions of the domains can be seen in Table 7. The rotating domain and the interface can be seen in Fig. 5 where the mesh is polyhedral. All self-propulsion simulations are conducted in speed trial condition, and only half of the twin screw ship is simulated since the flow is considered symmetric. The resolved flow

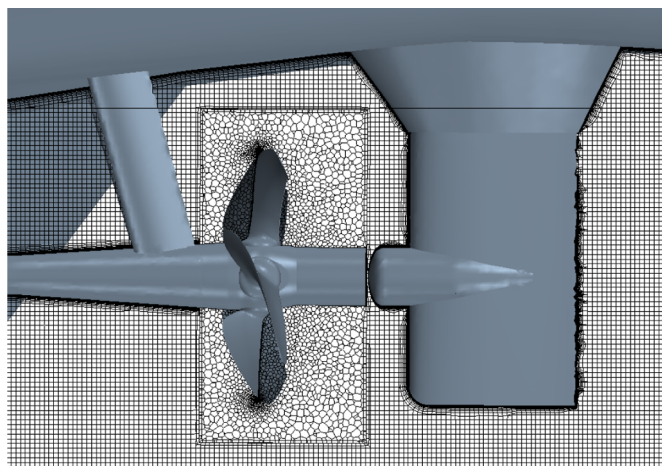


Fig. 5. Side view of self-propulsion mesh in shaft plane of the ro-ro vessel.

Table 7

Boundary conditions of the CFD self-propulsion set-up.

Name of boundary	Boundary condition
Inlet	Velocity inlet
Bottom	Velocity inlet
Outlet	Pressure outlet
Top	Velocity inlet
Symmetry	Symmetry plane
Port Side	Slip wall
Interface	Internal interface
Hull and propeller	No-slip wall

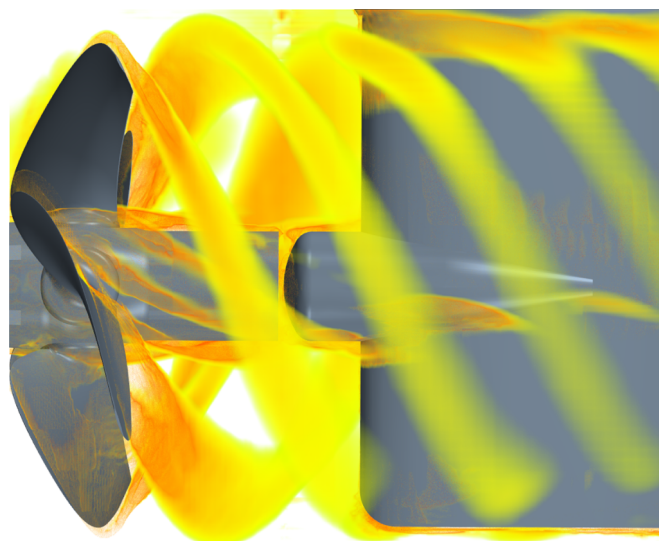


Fig. 6. Vorticity downstream of the ro-ro vessel propeller in a self-propulsion simulation.

around the propeller is illustrated in Fig. 6.

As in the resistance CFD set-up, the free surface is resolved using the VOF method. An illustration of the wave elevation in a self-propulsion simulation is shown in Fig. 7.

The dynamic pitch and heave are calculated in a separate simple self-propulsion simulation where the propeller is modelled using an actuator disc, and the hull and propeller are free to heave and pitch. The actuator disc is a simplified axis-symmetric model of the propeller. The actuator disc accelerates the flow over the disc area based in the propeller open-water characteristics. The presence of the actuator disc creates a pressure distribution in the aft ship required to accurately estimate the dynamic heave and pitch. The thrust from the actuator disc is added as a concentrated force on the shaft. The dynamic pitch and heave from this simplified self-propulsion simulation are used as fixed in the self-propulsion simulation with the geometrically rotating propeller. The self-propulsion simulation using the actuator disc only requires a fraction of the computational cost of the self-propulsion simulation with the sliding mesh approach.

For the self-propulsion simulations a combination of transient MRF and SM is used for increased computational efficiency. For 200 physical seconds, corresponding to approximately 400 propeller revolutions, the propeller is modelled using MRF to efficiently develop the flow around the ship and free surface. For the first 100 seconds, the time step is equal to the time step used for the resistance simulations. For the next 100 seconds a finer time step is used. After 200 seconds of using the MRF approach, the SM approach is used for the remaining part of the simulation. The SM uses a time step corresponding to two degrees of propeller rotation.

The rate of revolution of the propeller is changed using a p-controller until a force balance is obtained in the sailing direction within



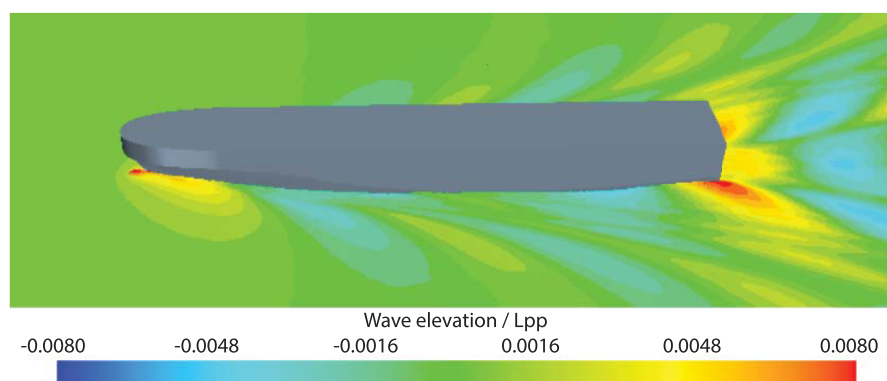


Fig. 7. Wave elevation from full-scale self-propulsion simulation of the ro-ro vessel in speed trial condition at  $Fn = 0.268$

0.5%, which is half the 1% tolerance recommended by ITTC [44]. The force balance is taken in the direction parallel to the shaft axis. The drag from the bow thruster and wind loads is also included in the force balance.

The model scale CFD self-propulsion set-up is carried out using the same principle with the exact same tow rope force as used by the towing tank. The full-scale self-propulsion set-up is created by scaling up the model scale self-propulsion set-up according to the scaling factor. The prism layers are changed so the wall  $y^+$  is mostly in the range of 30–200 on the hull and propeller. The force balance in full-scale is slightly different from model scale since the effect from air resistance and roughness on the hull and propeller is included. The two different approaches of including the roughness on the hull and propeller are explained in Sec. 3.3.

For the self-propulsion simulations using the Townsin roughness allowance (Eq. 21), the force balance is including the total drag on the ship, the propeller thrust, the empirically estimated wind and bow thruster resistance and the empirically estimated roughness resistance. The results of these simulations can be seen in Sec. 4.2. The total drag is found by integrating the pressure and shear distribution on all ship surfaces besides the propeller. When roughness is included using modified wall functions, the force balance only includes the total drag on the ship, the propeller thrust and the empirically estimated wind resistance and the bow thruster drag. The results of these simulations are shown in Sec. 4.3.

All power results for the ro-ro vessel are presented as delivered power as a percentage of Maximum Continuous Rating (MCR). Therefore, the loss in gears and shaft bearings are not included. This is considered reasonable, since the power is measured aft of the gear during the speed trial.

## 4. Results and discussion

In the following sections, the results of the speed trial measurements for the ro-ro vessel will be presented followed by a comparison with the towing tank prediction. Afterwards the CFD set-ups will be verified and validated, and finally the full-scale self-propulsion CFD results will be compared with the speed trial results. Only Sec. 4.3.1 presents results on the general cargo vessel. All other sections present results of the ro-ro vessel.

### 4.1. Speed trial measurements and comparison with towing tank prediction

The speed trial results provided by the shipyard are the measured values corrected for wind and current. The procedures of the speed trial and corrections are briefly described in Sec. 2.4. The results of the corrected delivered power as function of Froude number from the speed trials of the six sister vessels are shown in Fig. 8. It is challenging to choose a regression type to fit the results to a mean curve. The obvious

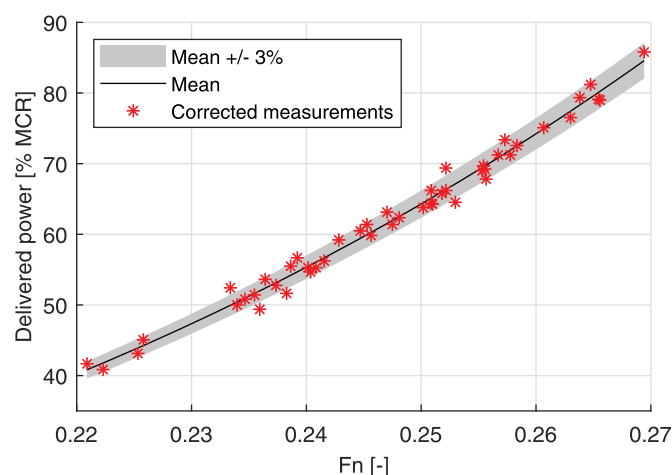


Fig. 8. Corrected speed trial measurement for the six ro-ro vessels including mean curve.

choice would be a power regression of the form  $P_d = aFn^b$  where  $a$  and  $b$  are constants and  $P_d$  is the delivered power in percentage of MCR. In classical fluid mechanics, the power is proportional with the speed to power of three. However, for ship resistance  $b$  is not constant and mostly higher than three. Without the consideration of humps and hollows,  $b$  is increasing when the ship speed is increasing, due to the wave generation. However, in this study,  $a$  and  $b$  are considered constant in the limited speed range. The fitted mean curve valid for the speed range  $Fn = 0.22 - 0.27$  is found to be  $P_d = 0.228Fn^{3.560}$ . The  $R^2$ -value of the fit is 0.9981. Most of the corrected speed trial measurements are within 3% of the mean curve, as seen in Fig. 8. It is very satisfactory with such a low scatter of the data points considering construction tolerances and measurements uncertainties when building and testing six 200m sister vessels. This indicates that the accuracy of the speed trial data is high and therefore a good reference for the validation study.

In order to validate the three different CFD set-ups in both model and full-scale in systematic steps, a more detailed set of accurate data is required. A full set of towing tank measurements and predictions is a good data set for this purpose. More details on the towing tank testing are found in Sec. 2.3. However, before these data are used, the full-scale towing tank prediction is compared with the mean speed trial curve. The discrepancy is within 1 percent for all speeds as seen in Table 8. This is considered very good and within the uncertainty of both the prediction and the speed trials. It should be noted that HSVA have used their own confidential correction formula for roughness and not the one recommended by ITTC. This excellent agreement indicates that the towing tank measurements and predictions are a good data set for validating the different CFD set-ups.



**Table 8**

Discrepancy of ro-ro vessel full-scale self-propulsion results from speed trial compared to towing tank prediction.

Froude number	Delivered power
0.222	− 0.9%
0.245	0.1%
0.268	0.5%

**Table 10**

Discrepancy of ro-ro vessel full-scale total resistance from CFD compared to towing tank prediction.

Froude number	Total resistance
0.222	− 2.5%
0.245	− 1.9%
0.268	− 1.5%

#### 4.2. CFD with empirical roughness

The following sections present the validation and results of the resistance, propeller open-water and self-propulsion CFD simulations. All results in Sec. 4.2 have been submitted to the shipyard without knowing the towing tank measurement and predictions and sea trial results. After the submission of the CFD results, the shipyard shared the full towing tank report with the authors. In this section, the hull roughness is estimated using the empirical Townsin formula (Eq. 21) and applied in the center of gravity as discussed in Sec. 3.3. Roughness on the propeller is not considered in this section.

##### 4.2.1. Verification and validation of the resistance simulations

The mesh convergence study of the resistance set-up, described in Sec. 3.4.1, is conducted at the lowest Froude number, because a lower Froude number gives shorter distance between the generated waves. The shorter the distance is, the finer mesh is required. Conversely, the time step convergence study is conducted at the highest Froude number since simulations at higher speeds have the highest Courant number. The spatial and temporal discretization error is estimated using the GCI method described in Sec. 3.2. The summary is presented in Table 9. It can be seen that the spatial and temporal GCIs for the medium mesh is 1.3% and 0.3% respectively. Both are within the uncertainty of the model test experiments and are therefore considered acceptable. Resistance simulations are conducted using the medium mesh and medium time step and the total resistance coefficients are compared with extrapolated towing tank results in Table 10. The comparison with extrapolated towing tanks results shows good agreement with underestimation in total resistance in CFD of up to 2.5% compared to towing tank extrapolation.

##### 4.2.2. Verification and validation of propeller open-water simulations

The result of the convergence study of the model scale propeller open-water CFD set-up shown in Table 11. It is seen that the spatial GCIs for thrust, torque and efficiency are lower than 2.5% for the medium mesh. It is therefore decided to use the medium mesh in the comparison studies. The exact uncertainty from the propeller open-water towing tank test is unknown. However, the difference between the measured propeller open-water characteristics in the towing tank

**Table 9**

Estimation of spatial and temporal discretization error in total resistance coefficient for full-scale resistance simulations of the ro-ro vessel.

	Spatial	Temporal
$r_{21}$	1.49	2
$r_{32}$	1.55	2
$\phi_1$	0.002056	0.002723
$\phi_2$	0.002074	0.002718
$\phi_3$	0.002224	0.002698
$p$	4.73	1.9
$\phi_{ext}^{21}$	0.002053	0.002725
$e_a^{21}$	0.889%	0.194%
$e_{ext}^{21}$	0.158%	0.071%
$GCI_{fine}^{21}$	0.197%	0.089%
$GCI_{medium}^{32}$	1.309%	0.330%

**Table 11**

Estimation of spatial discretization error for model scale propeller open-water simulation of the ro-ro vessel.

	KT	KQ	ETA <sub>0</sub>
$r_{21}$	1.33	1.33	1.33
$r_{32}$	1.35	1.35	1.35
$\phi_1$	0.3090	0.0512	0.5769
$\phi_2$	0.3073	0.0510	0.5749
$\phi_3$	0.3047	0.0509	0.5717
$p$	1.1994	0.8036	1.4485
$\phi_{ext}^{21}$	0.3131	0.0516	0.5806
$e_a^{21}$	0.555%	0.218%	0.337%
$e_{ext}^{21}$	1.324%	0.828%	0.647%
$GCI_{fine}^{21}$	1.677%	1.044%	0.813%
$GCI_{medium}^{32}$	2.370%	1.316%	1.235%

report of the port and starboard propeller was up to 4%. It is known that exact pitch setting of the model scale propeller is subject to some uncertainty. To study the sensitivity of pitch setting, a sensitivity study is conducted and it is found that 1 degree of pitch changes the thrust and torque with up to 15% and the efficiency with up to 4%. For both model and full-scale, the model scale propeller open-water CFD results are compared with the measured towing tank results in Table 12. The discrepancy in the propeller open-water characteristics between towing tank measurements and CFD is less than 5.5% for the advance ratio of approximately 0.86 where the propeller is operating. At the lower advance ratio where the propeller is normally not operating thrust and torque are overestimated with up to 10.1% and efficiency with up to 3.5%.

The results for the full-scale mesh convergence study show that the spatial GCIs for thrust, torque and efficiency are lower than 1.0% for the medium mesh, cf. Table 13. It is therefore decided to use the medium mesh. When comparing the full-scale propeller open-water CFD results with the towing tank predictions, as shown in Table 14, it is seen that the discrepancy in the propeller open-water efficiency is less than 1% for the advance ratio of approximately 0.86 where the propeller is operating. The thrust and torque are overestimated with up to 6.3% at these advance ratios. At the lower advance ratio where the propeller is normally not operating, thrust and torque are overestimated with up to 7.9%, and the propeller open-water efficiency is overestimated with up to 1.2%.

##### 4.2.3. Verification and validation of self-propulsion simulations

The medium mesh and time step at the self-propulsion CFD set-up

**Table 12**

Discrepancy of ro-ro vessel model scale propeller open-water characteristics from CFD compared to towing tank prediction.

Advance ratio	Thrust coefficient	Torque coefficient	Open-water efficiency
0.5	10.1%	8.5%	1.4%
0.6	9.7%	6.8%	2.7%
0.7	8.3%	4.6%	3.5%
0.8	5.4%	2.1%	3.3%
0.9	3.7%	0.9%	2.8%
1.0	2.6%	− 0.4%	3.0%

**Table 13**

Estimation of spatial discretization error for full-scale propeller open-water simulation of the ro-ro vessel.

	KT	KQ	ETA <sub>0</sub>
$r_{21}$	1.4687	1.4687	1.4687
$r_{32}$	1.3214	1.3214	1.3214
$\phi_1$	0.3269	0.0552	0.5656
$\phi_2$	0.3255	0.0551	0.5637
$\phi_3$	0.3237	0.0552	0.5605
$p$	1.9227	4.2094	2.6369
$\phi_{ext}^{21}$	0.3281	0.0552	0.5667
$e_d^{21}$	0.413%	0.078%	0.336%
$e_{ext}^{21}$	0.376%	0.019%	0.191%
$GCI_{fine}^{21}$	0.472%	0.024%	0.239%
$GCI_{medium}^{32}$	0.988%	0.121%	0.658%

**Table 14**

Discrepancy of ro-ro vessel full-scale propeller open-water characteristics from CFD compared to towing tank prediction.

Advance ratio	Thrust coefficient	Torque coefficient	Open-water efficiency
0.5	7.8%	7.1%	0.6%
0.6	7.9%	6.8%	1.0%
0.7	7.4%	6.2%	1.2%
0.8	6.3%	5.5%	0.8%
0.9	5.3%	5.2%	0.1%
1.0	5.3%	5.3%	− 0.1%

**Table 15**

Estimation of spatial and temporal discretization error in delivered power for model scale self-propulsion simulations of the ro-ro vessel.

	Spatial	Temporal
$r_{21}$	1.1613	1.5000
$r_{32}$	1.2070	2.0000
$\phi_1$	112.7	107.8
$\phi_2$	113.1	107.2
$\phi_3$	113.4	106.8
$p$	3.6029	4.3142
$\phi_{ext}^{21}$	112.1	107.9
$e_d^{21}$	0.342%	0.544%
$e_{ext}^{21}$	0.481%	0.114%
$GCI_{fine}^{21}$	0.599%	0.143%
$GCI_{medium}^{32}$	1.026%	0.824%

**Table 16**

Discrepancy of ro-ro vessel model scale self-propulsion results from CFD compared to towing tank measurements.

Froude number	Mean thrust	Mean torque	Propeller RPM	Delivered power
0.222	0.4%	− 0.8%	− 1.6%	− 2.4%
0.245	− 1.3%	− 0.1%	− 1.5%	− 1.6%
0.268	− 3.2%	0.0%	− 1.5%	− 1.5%

corresponds to the medium mesh and time step from the resistance CFD set-up and propeller open-water CFD set-up. Table 15 shows that the spatial and temporal GCI for delivered power for model scale self-propulsion simulations each is approximately 1% for the medium mesh and time step, which is acceptable. Therefore, it is decided to use the medium mesh and medium time step corresponding to two degrees of propeller rotation in the following calculation. The self-propulsion CFD results in model scale have been compared with the towing tank measurements and a very good agreement is found. A general underestimation is observed with a maximum discrepancy of 3.2% for both thrust, torque, RPM and delivered power as presented in Table 16. The

**Table 17**

Estimation of spatial and temporal discretization error in delivered power for full-scale self-propulsion simulations of the ro-ro vessel.

	Spatial	Temporal
$r_{21}$	1.306	2.000
$r_{32}$	1.411	2.000
$\phi_1$	26.239	25.438
$\phi_2$	25.802	25.390
$\phi_3$	32.256	25.039
$p$	7.9549	2.88
$\phi_{ext}^{21}$	26.299	25.445
$e_d^{21}$	1.668%	0.188%
$e_{ext}^{21}$	0.226%	0.030%
$GCI_{fine}^{21}$	0.283%	0.037%
$GCI_{medium}^{32}$	2.369%	0.272%

achieved advance ratio for the three self-propulsion points is approximately 0.86.

Mesh and time step convergence studies have also been conducted in full-scale as seen in Table 17. The temporal CGI is 0.3% when using the medium time step corresponding to two degrees of propeller rotation. For the medium mesh the spatial CGI is 2.4%. As shown in Table 2, each self-propulsion simulation takes approximately two days on 112 cores using the medium mesh. For the fine mesh the spatial GCI is 0.3%, but the required computational effort is impractically large for this study. Therefore, it has been decided to use the medium mesh and medium time step corresponding to two degrees of propeller rotation for the full-scale self-propulsion simulations.

The comparison between the full-scale CFD simulations and the towing tank prediction is shown in Table 18. As seen all parameters are significantly underestimated when using the traditional approach with the roughness allowance by Townsin (Eq. 21). This is surprising since the agreement between CFD and model tank for the previous simulations including full-scale resistance and model scale self-propulsion has been good. There are multiple contributors to the observed discrepancy. In terms of modelling errors, the use of realisable  $k - \epsilon$  RANS turbulence modelling can influence the results. A turbulence model sensitivity study is conducted by changing the turbulence model to  $k - \omega$  SST. This changed the power with 2.7% (not shown). Modelling the wind resistance using the ITTC recommended procedure is another source of error. However, since the wind resistance account for less than 7% of the total resistance, any uncertainty of the wind resistance will only have a marginal effect on the estimated power. The temporal and spatial discretization error is also present and is attempted quantified in the GCI study to 2.4% and 0.3% respectively. Furthermore, the "to-be-built" hull and propeller geometry used in the CFD simulations are not identical to real ship. Lastly, the sea trial measurements do also have uncertainties. However, the sea trial results from the six sister vessels presented in Fig. 8 showed that by using the mean of these the contribution from building tolerances and sea trial measurements becomes small. So none of these contributes can explain the large discrepancies in full-scale.

#### 4.3. Inclusion of roughness using wall functions

If the surface roughness of the hull and propeller is included in the

**Table 18**

Discrepancy of ro-ro vessel full-scale self-propulsion results from CFD compared to towing tank prediction.

Froude number	Mean thrust	Mean torque	Propeller RPM	Delivered power
0.222	− 2.9%	− 6.6%	− 6.1%	− 12.2%
0.245	− 4.4%	− 5.5%	− 5.9%	− 11.1%
0.268	− 4.1%	− 3.1%	− 5.5%	− 8.4%

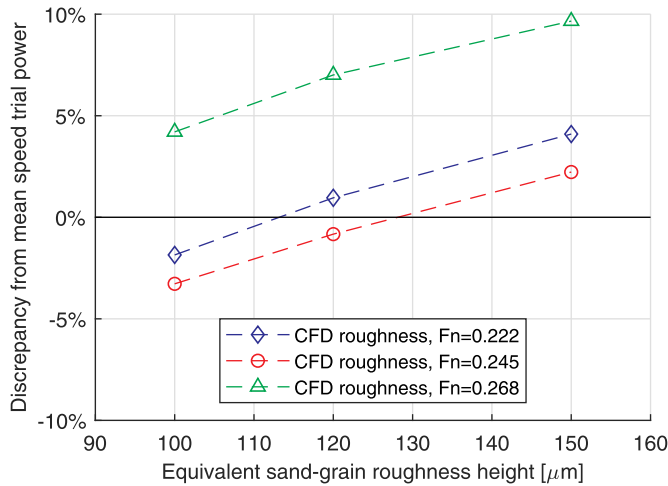


Fig. 9. Discrepancy of the ro-ro vessel CFD results compared to delivered power from speed trials as function of hull roughness height.

CFD simulation by modifying the wall functions, as described in Sec. 3.4.2, the discrepancy is significantly reduced, cf. Fig. 9. For the two lowest speeds the discrepancies between the delivered power from CFD and mean speed trial curve are within 4% for equivalent sand grain roughness heights between  $100\mu\text{m}$ – $150\mu\text{m}$ . These discrepancies are significantly smaller than the up to 12.2% found when using the Townsin roughness allowance. For the Froude number equal to 0.268, the delivered power is overestimated by 4.2% when  $R_s = 100\mu\text{m}$  and by 9.6% when  $R_s = 150\mu\text{m}$ . The discrepancies for the two lowest speeds are very similar, but the discrepancies for the larger speed is higher. This speed dependence is also seen in Table 18, where there is almost 3% difference in the delivered power discrepancy between  $Fn = 0.245$  and  $Fn = 0.268$ . The reason for this gap is due to the unwanted flow around the aft part of the ship as shown in Fig. 10b. Fig. 10b shows that the flow is much worse seen from a hydrodynamic point of view compared to the flow in model scale as shown in Fig. 10a. When comparing the wave elevation at the aft part in a model scale self-propulsion simulation (not shown) and a full scale resistance simulation (not shown), it is seen that the wave elevation is very similar. This is as expected when having identical Froude number. However, in full-scale self-propulsion the propeller is rotating at a much higher Reynolds number affecting the flow field near the propeller. At the lower speeds  $Fn = 0.222$  and  $Fn = 0.245$ , the flow is much smoother (not shown). This is believed to be the reason for the significant speed dependence at the highest speed ( $Fn = 0.268$ ) in full scale cf. Table 18 and Fig. 9 and not in model scale cf. Table 16. This shows that the influence of the propeller Reynolds number can affect the wave elevation near the aft, if the water line comes close to the propeller. This is the case at the very light sea trial condition. It is important to note that the ship is not likely to sail at such a light condition at this very high speed other than at the sea trial. The  $R_s^+$  is approximately 10–60 on both the hull and propeller as seen in Figs. 11 and 12. Thus, the  $R_s^+$  is smaller than the wall  $y^+$  in all cells. This is done in order to avoid under-prediction of the frictional resistance as discussed by Eca and Hoekstra [45].

These results indicate that modelling of the roughness using modified wall functions can significantly improve the accuracy of the full-scale CFD prediction compared to the traditional approach.

#### 4.3.1. LR workshop vessel

To test the method of including the roughness by changing the wall functions, a second vessel is studied. For the second vessel the rate of revolution of the propeller was predefined by the LR workshop and the workshop participants submitted, among other results, the speed and power, without knowing the measured speed and power. The comparison of the CFD calculations and speed trial measurements are shown in

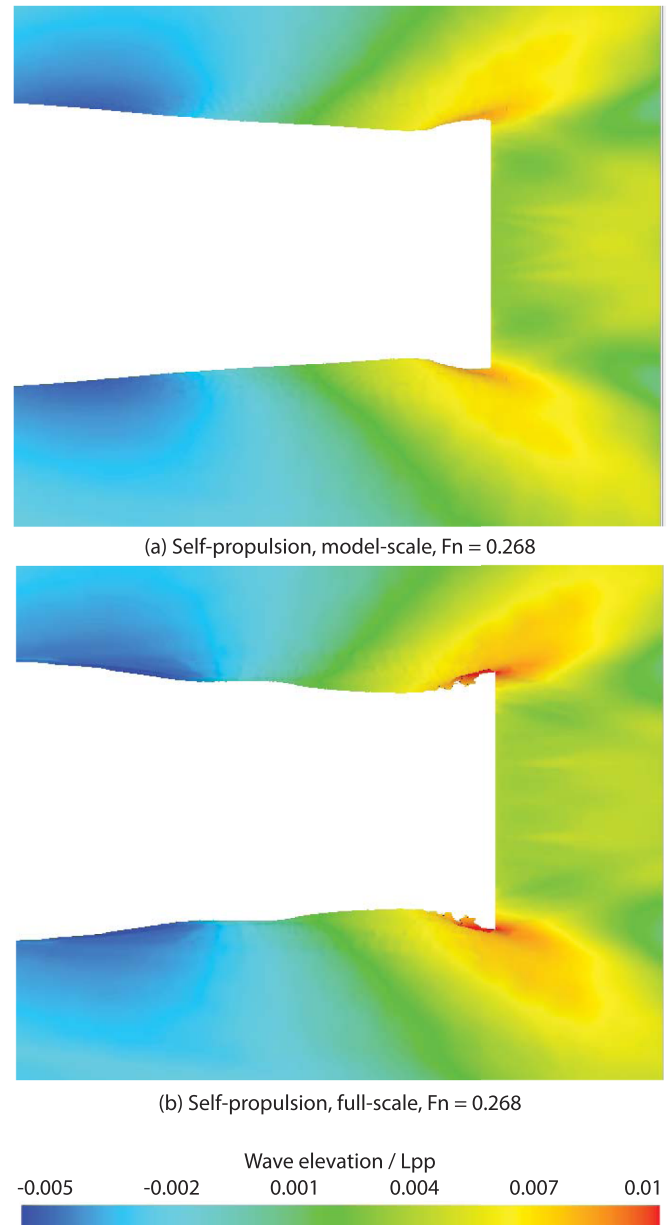


Fig. 10. Wave elevation non-dimensionalized with length between perpendiculars at aft seen from top. The hull and propellers are smooth for all shown conditions.

Fig. 1. It can be seen that the scatter of the CFD results are increasing when the RPM is increasing. Since the scatter at  $Fn = 0.182$  is quite large, only the speed range of  $Fn = 0.140$ – $0.168$  is considered in this study. It can be seen that CFD results from some participants are very similar to the speed trial measurements and some are far off. The host of the workshop calculated a mean curve of the CFD results showing that the CFD simulations are under-predicting the power with up to 11.7%. This is consistent with the CFD results for ro-ro vessel, when using the empirical Townsin roughness approach.

By using the self-propulsion set-up described in Sec. 3.4.2, CFD calculations have been conducted for the three fixed speeds  $Fn = 0.140$ ,  $Fn = 0.154$ , and  $Fn = 0.168$ . The mesh validated for the ro-ro vessel has been adapted to the REGAL vessel, and a mesh convergence study was conducted for the vessel showing a smaller spatial discretization error than for the ro-ro vessel cf. Table 17. A time step corresponding to two degrees of propeller rotation is used for the general cargo vessel. Since the vessel only has one propeller, both sides of the vessel are included in

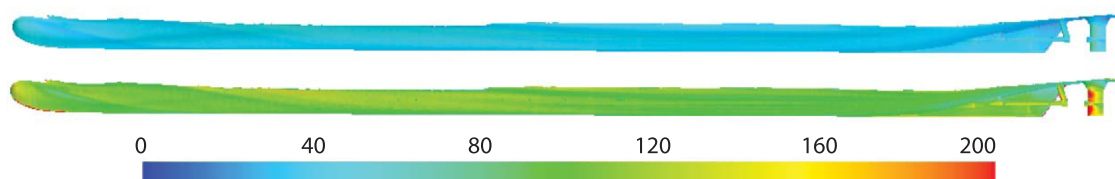


Fig. 11.  $R_s^+$  (top) and wall  $y^+$  (bottom) on the wetted surface of the ro-ro vessel with  $R_s = 120\mu\text{m}$  at  $\text{Fn} = 0.245$ .

the CFD simulations. The discrepancies between the speed trial measurement and both the CFD from the LR Workshop participants and CFD conducted by the authors using the Townsin empirical roughness are shown in Table 19. It is seen that the results of the present CFD simulations using the empirical Townsin roughness approach provide results similar to the LR Workshop mean curve. In both cases the power is underestimated by 10–14%.

CFD simulations are now conducted for the general cargo vessel, where the roughness is taken into account using the modified wall functions. Unfortunately, the roughness of the hull and propeller is unknown. It is assumed that the roughness of the propeller is  $R_s = 30\mu\text{m}$ . Three different hull roughness heights are tested in the range of  $R_s = 100\mu\text{m}$ – $150\mu\text{m}$  based on the literature study presented in Sec. 3.3. The discrepancies between the CFD results and speed trial measurement are shown in Fig. 13. Using this approach the power is underestimated with 6.1–11.1% for  $R_s = 100\mu\text{m}$  and with 3.1 – 0.1% for  $R_s = 150\mu\text{m}$ . These discrepancies are generally smaller than when using the empirical Townsin roughness approach. The speed dependence tendency is clearly seen in Fig. 13. For the lowest to highest speed there is an approximately 5 percentage points off-set. The monotonic behaviour of the speed dependence for the general cargo vessel is not observed for the ro-ro vessel in Fig. 9. The offset of approximately 5 percentage points is believed to come from other uncertainty contributors that roughness as discussed in Sec. 4.2.3.

The larger underestimation of for the general cargo vessel than for the ro-ro vessel could indicate that the surface roughness of the general cargo vessel is larger than for the ro-ro vessels, even though the ro-ro vessels have been in the water longer time before the speed trial. Since the general cargo vessel is an older vessel with multiple previous dry dockings in its history, the paint roughness is potentially higher as seen in Table 3 where the results from Atencio and Chernoray [37] show that old underlying roughness accumulated from many dry dockings can have a large impact on the roughness height. However, it is important to remember that modelling of roughness is only one of the discrepancy contributors. The trend of higher accuracy when including the

Table 19

Discrepancy in delivered power between LR speed trial measurements and CFD calculations both from LR workshop mean curve and present CFD results using the ITTC roughness.

Froude number	0.140	0.154	0.168
LR workshop mean	– 11.7%	– 10.5%	– 11.1%
Present CFD results	– 13.8%	– 12.4%	– 13.1%

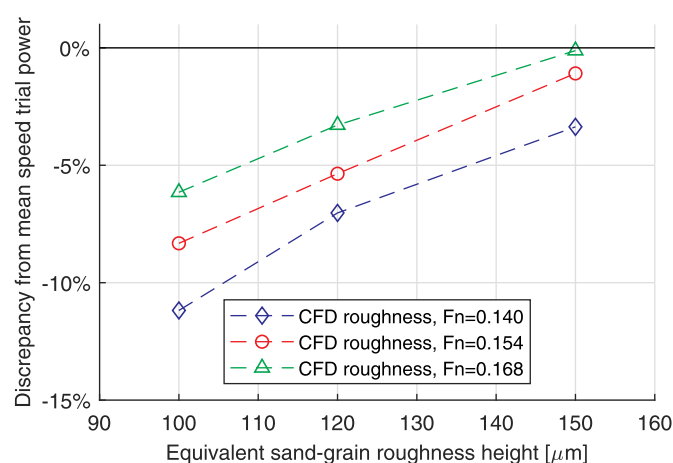


Fig. 13. Discrepancy of CFD results compared to delivered power from speed trials as function of hull roughness height for the LR workshop vessel REGAL.

roughness of the hull and propeller instead of using the Townsin roughness allowance is similar for both the low block ro-ro vessel and the high block general cargo vessel. This gives the clear indication that including the roughness by modifying the wall functions can significantly improve the accuracy of the CFD simulation.

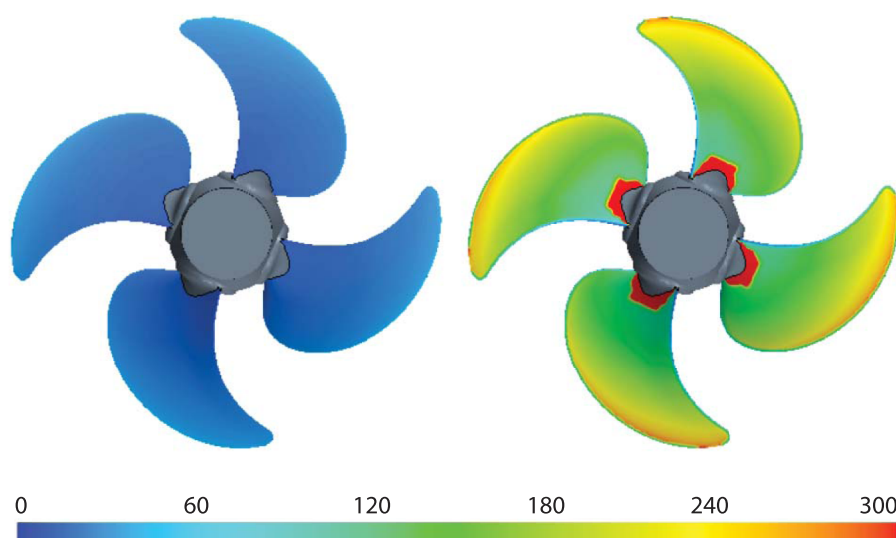


Fig. 12.  $R_s^+$  (left) and wall  $y^+$  (right) on the ro-ro vessel propeller with  $R_s = 30\mu\text{m}$  at  $\text{Fn} = 0.245$ .



## 5. Conclusions

A full-scale self-propulsion CFD set-up with free surface and rotating propeller has been developed and verified and validated in systematic steps in order to ensure accuracy. The reference in full-scale was the mean speed/power curve from speed trials of the six sister vessels. The scatter of the speed trials was small with most of the measurements within 3% of the mean curve. The towing tank prediction of the delivered power in full-scale was within 1% of the speed trial for all speeds. Due to this excellent accuracy of the towing tank prediction, the towing tank measurements and predictions were used to validate the CFD set-up in systematic steps. The discrepancies for resistance, propeller open-water and model scale self-propulsion CFD simulations were found to be within the model test uncertainty. However, for the full-scale self-propulsion simulation, the delivered power from CFD was underestimated with 8–12% compared to the speed trial measurements when the roughness was estimated using the standard empirical formula by Townsin and applied as a point force in the center of gravity. By including a roughness model directly into the self-propulsion simulation using a modifying wall function approach, the discrepancy was significantly reduced. The same conclusions were found for a general cargo vessel where the geometry and speed trial data are publicly available. Unfortunately, the exact roughness of the surface of the two vessels was unknown. Based on a literature study on roughness measurements on newly painted ships, a range of sand-grain equivalent roughness heights of 100–150  $\mu\text{m}$  was tested for both vessels resulting in significantly reduced discrepancies to the speed trial measurements for both cases. This indicates that using a roughness model directly into the CFD simulation is more accurate than the traditional method using empirical formulas designed for towing tanks.

## CRediT authorship contribution statement

**Henrik Mikkelsen:** Conceptualization, Methodology, Software, Validation, Formal analysis, Investigation, Writing - original draft, Writing - review & editing, Visualization, Funding acquisition. **Jens Honoré Walther:** Conceptualization, Methodology, Writing - review & editing, Supervision, Project administration, Funding acquisition.

## Declaration of Competing Interest

The authors declare that they have no known competing financial interests or personal relationships that could have appeared to influence the work reported in this paper.

## Acknowledgements

The research was supported by The Danish Maritime Fund under grant 2018-11, whose support is greatly appreciated. We would like to thank the shipyard and propeller manufacturer for providing unique and rarely shared data.

## References

- [1] IMO, Amendments to marpol annex vi on regulations for the prevention of air pollution from ships by inclusion of new regulations on energy efficiency for ships, MEPC 62/24/Add.1, Annex 19, 2011.
- [2] J. Kim, I.-R. Park, K.-S. Kim, S.-H. Van, Numerical simulation of turbulent free surface flow around a self-propelled ship, *Proc. Fifteenth Int. Offshore Polar Eng. Conf.*, Seoul, Korea, (2005), pp. 180–186.
- [3] L. Larsson, F. Stern, M. Visonneau, *Proceedings of Gothenburg 2010 - A workshop on numerical ship hydrodynamics*, (2010).
- [4] L. Larsson, F. Stern, M. Visonneau, T. Hino, N. Hirata, J. Kim, *Proceedings of Tokyo 2015 workshop on CFD In Ship hydrodynamics*, (2015).
- [5] D. Ponkratov, *Proceedings of 2016 workshop on ship scale hydrodynamic computer simulation*, Lloyd's Register, 2017.
- [6] H. Jasak, V. Vukčević, I. Gatin, I. Lalović, CFD validation and grid sensitivity studies of full scale ship self propulsion, *Int. J. Nav. Archit. Ocean Eng.* 11 (1) (2019) 33–43, <https://doi.org/10.1016/j.jnaoe.2017.12.004>.
- [7] H. Mikkelsen, M.L. Steffensen, C. Ciortan, J.H. Walther, Ship scale validation of CFD model of self-propelled ship, *Mar. 2019 Comput. Methods Mar. Eng.* VIII, (2019), pp. 718–729.
- [8] W. Sun, Q. Hu, S. Hu, J. Su, J. Xu, J. Wei, G. Huang, Numerical Analysis of Full-Scale Ship Self-Propulsion Performance with Direct Comparison to Statistical Sea Trial Results, *J. Mar. Sci. Eng.* 8 (1) (2020) 24, <https://doi.org/10.20944/preprints201912.0318.v1>.
- [9] T. Cebeci, P. Bradshaw, *Momentum transfer in boundary layers*, Hemisphere Publishing Corporation/McGraw-Hill, 1977.
- [10] S. Song, Y.K. Demirel, M. Atlar, An investigation into the effect of biofouling on the ship hydrodynamic characteristics using CFD, *Ocean Eng.* 175 (2019) 122–137, <https://doi.org/10.1016/j.oceaneng.2019.01.056>.
- [11] S. Song, Y.K. Demirel, M. Atlar, O. Turan, Validation of the CFD approach for modelling roughness effect on ship resistance, 6th Int. Conf. Adv. Model Meas. Technol. Marit. Ind. (2019).
- [12] S. Song, Y.K. Demirel, M. Atlar, Penalty of hull and propeller fouling on ship self-propulsion performance, *Appl. Ocean Res.* 94 (2020) 102006, <https://doi.org/10.1016/j.apor.2019.102006>.
- [13] IMO, ISO 15016:2015, MEPC 68/INF.14 (2015).
- [14] Siemens, STAR-CCM+ User guide, Version 2019.1.1, 2019.
- [15] J. Ferziger, M. Peric, *Computational methods for fluid dynamics*, 3rd Edition, Springer, 2002.
- [16] D. Wilcox, *Turbulence modelling for CFD*, 2nd edition, DCW. Industries, 1998.
- [17] T.-H. Shih, W.W. Liou, A. Shabbir, Z. Yang, J. Zhu, A new  $k-\epsilon$  eddy viscosity model for high Reynolds number turbulent flows, *Comput. Fluids* 24 (3) (1995) 227–238, [https://doi.org/10.1016/0045-7930\(94\)00032-T](https://doi.org/10.1016/0045-7930(94)00032-T).
- [18] R.B. Langtry, A correlation-based transition model using local variables for unstructured parallelized CFD codes, University of Stuttgart, 2006 Ph.D. thesis.
- [19] C. Hirt, B. Nichols, Volume of fluid (VOF) method for the dynamics of free boundaries, *J. Comput. Phys.* 39 (1) (1981) 201–225, [https://doi.org/10.1016/0021-9991\(81\)90145-5](https://doi.org/10.1016/0021-9991(81)90145-5).
- [20] S. Muzafarjia, M. Peric, Computation of free-surface flows using the finite-volume method and moving grids, *Numer. Heat Transf. Part B Fundam.* 32 (4) (1997) 369–384, <https://doi.org/10.1080/10407799708915014>.
- [21] I.B. Celik, U. Ghia, P.J. Roache, C.J. Freitas, H. Coleman, P.E. Raad, Procedure for estimation and reporting of uncertainty due to discretization in CFD applications, *J. Fluids Eng.* 130 (7) (2008) 078001, <https://doi.org/10.1115/1.2960953>.
- [22] L.F. Richardson, The approximate arithmetical solution by finite differences of physical problems involving differential equations, with an application to the stresses in a masonry dam, *Philos. Trans. R. Soc. A Math. Phys. Eng. Sci.* 210 (459–470) (1910) 307–357, <https://doi.org/10.1098/rsta.1911.0009>.
- [23] L.F. Richardson, J.A. Gaunt, The deferred approach to the limit. Part I. Single lattice. Part II. Interpenetrating lattices, *Philos. Trans. R. Soc. A Math. Phys. Eng. Sci.* 226 (636–646) (1927) 299–361, <https://doi.org/10.1098/rsta.1927.0008>.
- [24] P.J. Roache, Verification of codes and calculations, *AIAA J.* 36 (5) (1998) 696–702.
- [25] B.S. Bowden, N.J. Davison, Resistance increments due to hull roughness associated with form factor extrapolation methods, *Natl. Phys. Lab. Sh. Tech. Man.* 3800 (1974).
- [26] ITTC, 1978 ITTC - Performance prediction method. ITTC - Recommended procedures and guidelines, Procedure 7.5-02-03-01.4, Revision 01, 2008.
- [27] R.L. Townsin, M.A. Mosaad, The ITTC line its genesis and correlation allowance, *Nav. Archit.* 1985 (1985).
- [28] ITTC, The propulsion committee - Final report and recommendations to the 28th ITTC, *Proc. 28th ITTC*, 2017 1 (2017).
- [29] F.H. Clauser, Turbulent boundary layers in adverse pressure gradients, *J. Aeronaut. Sci.* 21 (2) (1954) 91–108, <https://doi.org/10.2514/8.2938>.
- [30] Y.K. Demirel, O. Turan, A. Incecik, Predicting the effect of biofouling on ship resistance using CFD, *Appl. Ocean Res.* 62 (2017) 100–118, <https://doi.org/10.1016/j.apor.2016.12.003>.
- [31] M.P. Schultz, K.A. Flack, The rough-wall turbulent boundary layer from the hydraulically smooth to the fully rough regime, *J. Fluid Mech.* 580 (2007) 381–405, <https://doi.org/10.1017/S00222112007005502>.
- [32] M. Leer-Andersen, L. Larsson, An experimental/numerical approach for evaluating skin friction on full-scale ships with surface roughness, *J. Mar. Sci. Technol.* 8 (1) (2003) 26–36, <https://doi.org/10.1007/s10773-003-0150-y>.
- [33] J. Nikuradse, *Stromungsgesetze in rauhen rohren*. *Forsch. Arb. Ing.-Wes.*, 361, English Transl. as NACA-TM-1292 3 (1933).
- [34] A. Lindholdt, K. Dam-Johansen, S.M. Olsen, D.M. Yebra, S. Kiil, Effects of biofouling development on drag forces of hull coatings for ocean-going ships: a review, *J. Coatings Technol. Res.* 12 (3) (2015) 415–444, <https://doi.org/10.1007/s11998-014-9651-2>.
- [35] I.K.A.P. Utama, B. Nugroho, C. Chin, M.L. Hakim, F.A. Prasetyo, M. Yusuf, I.K. Suastika, J. Monty, N. Hutchins, B. Ganapathisubramani, A study of skin friction-drag from realistic roughness of a freshly cleaned and painted ship hull, *Proc. Int. Symp. Mar. Eng.* (2017).
- [36] M.P. Schultz, Frictional resistance of antifouling coating systems, *J. Fluids Eng.* 126 (6) (2004) 1039–1047, <https://doi.org/10.1115/1.1845552>.
- [37] B. Nibbles Atencio, V. Chernoray, A resolved RANS CFD approach for drag characterization of antifouling paints, *Ocean Eng.* 171 (2018) 519–532, <https://doi.org/10.1016/j.oceaneng.2018.11.022>.
- [38] M.P. Schultz, J.M. Walker, C.N. Steppe, K.A. Flack, Impact of diatomaceous biofilms on the frictional drag of fouling-release coatings, *Biofouling* 31 (9) (2015) 759–773, <https://doi.org/10.1080/08927014.2015.1108407>.
- [39] O. Usta, E. Korkut, A study for the effect of surface roughness on resistance characteristics of flat plates, *Int. Conf. Mar. Coatings*, Royal Institution of Naval Architects, 2013, pp. 29–37.

- [40] D. Howell, B. Behrends, A review of surface roughness in antifouling coatings illustrating the importance of cutoff length, *Biofouling* 22 (6) (2006) 401–410, <https://doi.org/10.1080/08927010601035738>.
- [41] D. Owen, Y.K. Demirel, E. Oguz, T. Tezdogan, A. Incecik, Investigating the effect of biofouling on propeller characteristics using CFD, *Ocean Eng.* 159 (2018) 505–516, <https://doi.org/10.1016/j.oceaneng.2018.01.087>.
- [42] T. Adams, C. Grant, H. Watson, A simple algorithm to relate measured surface roughness to equivalent sand-grain roughness, *Int. J. Mech. Eng. Mechatronics* 1 (1) (2012) 66–71, <https://doi.org/10.11159/ijmem.2012.008>.
- [43] M.P. Schultz, Effects of coating roughness and biofouling on ship resistance and powering, *Biofouling* 23 (5) (2007) 331–341, <https://doi.org/10.1080/08927010701461974>. arXiv:1011.1669v3
- [44] ITTC, ITTC Recommended procedures and guidelines - Practical guidelines for ship self-propulsion CFD, 2014.
- [45] L. Eça, M. Hoekstra, Numerical aspects of including wall roughness effects in the SST k-epsilon eddy-viscosity turbulence model, *Comput. Fluids* 40 (1) (2011) 299–314, <https://doi.org/10.1016/j.compfluid.2010.09.035>.



## Chapter 3

### Paper B

# CFD verification and validation of added resistance and seakeeping response in regular oblique waves with varying wave length

The paper entitled "CFD verification and validation of added resistance and seakeeping response in regular oblique waves with varying wave length" is published in MARINE 2021 Computational Methods in Marine Engineering IX:

Mikkelsen, H., Shao,Y. and Walther, J. H. (2021) CFD verification and validation of added resistance and seakeeping response in regular oblique waves with varying wave length. *MARINE 2021 Computational Methods in Marine Engineering IX*, Page number 1-24.

The paper is here reproduced with permission from International Centre for Numerical Methods in Engineering, not for further re-distribution or re-use.



# CFD Verification and Validation of Seakeeping and Added Resistance of a Container Ship in Regular Oblique Waves with Varying Wave Length

MARINE 2021

Henrik Mikkelsen<sup>1,\*</sup>, Yanlin Shao<sup>1</sup> and Jens H. Walther<sup>1,2</sup>

<sup>1</sup> Technical University of Denmark (DTU)  
Department of Mechanical Engineering  
Nils Koppels Allé, Building 404, 2700 Kgs. Lyngby, Denmark.

<sup>2</sup> Swiss Federal Institute of Technology Zurich (ETH Zürich)  
Computational Science & Engineering Laboratory  
Clausiusstrasse 33, CH-8092 Switzerland

\* Corresponding author: Jens H. Walther, jhw@mek.dtu.dk

## ABSTRACT

The importance of CFD is increasing in marine hydrodynamics in studying seakeeping and added resistance of ships. While extensive numerical studies have been reported for various ships in head seas in the literature, much fewer CFD studies are found for oblique waves, which in practice is very important in, for instance, estimating required power and manoeuvrability of ships in realistic sea states. In this paper, the added resistance and motion responses for the KCS container ship in regular waves are studied and validated systematically for five wave headings and six wavelengths using CFD. The ship is free to heave, pitch, and roll. User-defined implementations in the commercial CFD code are made to effectively constrain the surge and yaw. Extensive verification of the CFD model finds the estimated spatial and temporal discretization errors to be less than 5 %. Results of the verified CFD model are compared with up to three sets of experimental data sets, Potential Flow (PF) and existing CFD results from the literature. In general, the present CFD results show significantly better agreement with the experiments than previously published CFD results. The present study shows that CFD simulations accurately can predict motion responses and added resistance in oblique regular waves. However, further experiments with smaller uncertainties in following and stern quartering sea are required, to better support future validations of CFD simulations.

**Keywords:** CFD; Added resistance in waves; Oblique waves; Validation.

## NOMENCLATURE

$a_k, b_k$	Fourier coefficients [-]	$f_{Z\theta}$	Natural heave/pitch frequency without forward speed [Hz]
$A$	Wave amplitude [m]	$f_{Z\theta, U}$	Natural heave/pitch frequency with forward speed [Hz]
$A_k$	k-th amplitude [m] or [°] or [N]	$f_e$	Encounter frequency [s <sup>-1</sup> ]
$B$	Beam of ship [m]	$k$	Turbulent kinetic energy [m <sup>2</sup> s <sup>-2</sup> ]
$C_\mu$	Empirical constant [-]	$k$	Wavenumber [m <sup>-1</sup> ]
$e_a$	Approximate relative error [-]	$k_{xx}$	Longitudinal radius of gyration [m]
$e_{ext}$	Extrapolated relative error [-]	$k_{yy}$	Transverse radius of gyration [m]
$f_i$	Body force [kg m <sup>-2</sup> s <sup>-2</sup> ]	$KG$	Vertical center of gravity (from keel) [m]
$f_e$	Encounter frequency [Hz]	$L_{pp}$	Length between perpendiculars [m]
$f_\phi$	Natural roll frequency without forward speed [Hz]	$p$	Pressure [Pa]
$f_{\phi, U}$	Natural roll frequency with forward speed [Hz]		

$p$	Apparent order of convergence [-]	$\mu_w$	Dynamic viscosity of water phase [Pa s]
$r$	Refinement ratio [-]	$\mu_t$	Turbulent viscosity [Pa s]
$R$	Resistance [N]	$\rho$	Density [kg m <sup>-3</sup> ]
$R_0$	Mean resistance [N]	$\rho_a$	Density of air phase [kg m <sup>-3</sup> ]
$R_{CW}$	Calm water resistance [N]	$\rho_w$	Density of water phase [kg m <sup>-3</sup> ]
$s$	Solution	$\sigma_{aw}$	Added resistance [N]
$s$	Sign indicator	$\tau_x$	Skin friction in the $x$ -direction [Pa]
$S_{ij}$	Mean shear rate [s <sup>-1</sup> ]	$\phi$	Roll [°]
$T$	Draft [m]	$\phi_1$	First roll amplitude [°]
$t$	Time [s]	$\phi_k$	Solution on the $k$ -th mesh [m] or [°] or [N]
$T_e$	Encounter period [s]	$\omega_k$	Angular frequency [rad s <sup>-1</sup> ]
$\mathbf{u}$	Velocity vector [m s <sup>-1</sup> , m s <sup>-1</sup> , m s <sup>-1</sup> ]	CFD	Computational Fluid Dynamics
$\mathbf{u}'$	Turbulent fluctuating part of the velocity vector [m s <sup>-1</sup> , m s <sup>-1</sup> , m s <sup>-1</sup> ]	COG	Center of Gravity
$U$	Speed [m/s]	DTC	Duisburg Test Case
$y^+$	Non-dimensional wall distance [-]	DFBI	Dynamic Fluid Body Interaction
$Z$	Heave [m]	EFD	Experimental Fluid Dynamics
$Z_1$	First heave amplitude [m]	GCI	Grid Convergence Index
$\alpha$	Volume fraction [-]	HOBEM	Higher Order Boundary Element Method
$\Delta$	Displacement [kg]	IIHR	Iowa Institute of Hydraulic Research
$\epsilon$	Turbulent dissipation rate [m <sup>2</sup> s <sup>-3</sup> ]	KCS	KRISO Container Ship
$\epsilon$	Relative error [m] or [°] or [N]	KVLCC2	KRISO Very Large Crude Carrier
$\theta$	Pitch [°]	PF	Potential Flow
$\theta_1$	First pitch amplitude [°]	STF	Salvesen-Tuck-Faltinsen
$\lambda$	Wave length [m]	URANS	Unsteady Reynolds Averaged Navier-Stokes
$\mu$	Dynamic viscosity [Pa s]	UZ	University of Zagreb
$\mu_a$	Dynamic viscosity of air phase [Pa s]	VOF	Volume Of Fluid

## 1 INTRODUCTION

For the last decades most commercial ship hulls have been designed and optimized for sailing fully loaded with full speed in calm water. Traditionally, the effects of wind and waves have been included by adding a sea margin of 15 percent (Molland et al., 2011) to the required engine power. Over the last 10 years, this single design point approach has started to change by including more draughts and speeds into the design matrix (Psaraftis and Kontovas, 2014). This has narrowed the gap between the conditions ships are design for and the conditions the ships will operate in. However, almost all ship hulls are still designed using a combination of experience, towing tank tests and Computational Fluid Dynamics (CFD), mostly in calm water. The next natural step is to include the influence of interaction with waves into the ship hull design phase. Since almost no ships are constantly sailing in calm water, optimizing the ship hull to realistic sea states in the future has significant potential to reduce fuel costs and emissions. Seakeeping tests of motion responses and added resistance in towing tanks can be expensive, time demanding and dependent on the availability of the tanks. If numerical approaches are verified and validated to become trustworthy, they could be used with confidence in the design phase of new ship hulls. Since numerical simulations only require an available computer and not a large manufactured wooden ship model or a free towing tank slot, ship designers can easily test the seakeeping capabilities of tens or hundreds of ship hulls in the design phase. The use of numerical approaches also makes it possible to study the full-scale ship (Jasak et al., 2018; Niklas and Pruszko, 2019; Mikkelsen and Walther, 2020) and thereby avoiding scale effects. The knowledge of a ship's seakeeping properties is also important for both a comfort and safety point of view. Most often, the comfort limit is reached before the motion limit for safety, especially for passenger ships.

For non-passenger ships, comfort limits related to ship motions in waves are not as strict. For these ships, the safety can sometimes be the limiting factor, e.g., for container ships, where containers can fall into the sea, if motions become too large. However, the added resistance in waves are important for all ships, since it increases fuel consumption and potentially limits the ship speed.

One of the first studies of added resistance in waves is by Storm-Tejsen et al. (1973), who conducted added resistance experiments of the series 60 ships. Fujii and Takahashi (1975) compared experiments and strip theory simulations on the S175 container ship. Most seakeeping and added resistance research has been focusing on head sea waves. Added resistance in head sea waves using CFD, has been studied intensively by e.g. Sadat-Hosseini et al. (2013), who numerically studied the KRISO Very Large Crude 2 Carrier (KVLCC2). Kim et al. (2017b) have also studied the KVLCC2 using both CFD and 3D potential flow theory. Park et al. (2016) studied the added resistance of a tanker in head sea waves at different drafts using the Salvesen-Tuck-Faltinsen (STF) strip theory (Salvesen et al., 1970) and a B-spline based time-domain Rankine panel method (Kim et al., 2011). Simonsen et al. (2013) and Wu et al. (2020) studied the added resistance of the KRISO Container Ship (KCS) in head sea waves both experimentally and using CFD.

Fewer validation studies have been conducted in oblique waves. Studying the ship-wave interaction in oblique waves is important in order to quantify the added power and maneuverability in a realistic sea, where the waves are seldomly uni-directional. Fujii and Takahashi (1975) experimentally studied the added resistance on the S175 container ship in various headings relative to the incident wave. More recently, experimental studies of the Duisburg Test Case (DTC) and the KVLCC2 were conducted by Sprenger et al. (2016). Valanto and Hong (2015) experimentally tested the added resistance of a confidential cruise ship in seven different headings identifying the  $45^\circ$  heading to give maximum added resistance. Park et al. (2019) investigated the added resistance of a confidential tanker both experimentally and numerically in oblique waves. Both strip theory and a 3D Rankine panel method were used and the 3D Rankine panel method predicted the motion in oblique waves with fair agreement. The accuracy of the 3D Rankine panel method was found to be low in predicting the added resistance. The strip method was overestimating the added resistance significantly. A study by Liu and Papanikolaou (2016) predicted the added resistance in oblique waves with a far-field method using Kochin function for a bulk carrier and the Duisburg Test Case (DTC) container ship with fair agreement with the experiments. In general the agreement between numerical results and experiments were better for the longer waves than the shorter waves. Yang et al. (2019) used a frequency-domain hybrid Higher Order Boundary Element Method (HOBEM) to predict the motion responses and added resistance of different ship types sailing in head and oblique waves. In general, good agreement between numerical and experimental results were found. Liu et al. (2018) studied the wave forces and motions of the DTC ship in oblique waves for a single short wave length. They found that the diffraction and radiation effects have significant influence on the non-linearity of wave forces. Gong et al. (2020) numerically studied added resistance and seakeeping performance of trimarans in oblique waves. The results showed that the trends of the added resistance and motion amplitudes of the trimaran in waves are significantly affected by the wave steepness and wave incident angles, which are also different from those of traditional mono-hull ships. Chuang and Steen (2013) studied the speed loss of a vessel sailing in oblique waves both numerically and experimentally. They found that the speed reduction due to added resistance and due to steering are at almost the same level for head sea and bow sea conditions for the studied tanker with twin azimuth propulsors. Mousavi et al. (2020) studied the motion response in two oblique irregular wave headings using both CFD and a strip theory. Jin et al. (2017) experimentally and numerically studied the wave induced loads and motions on two gas carriers in a regular head wave and an oblique wave, both at zero forward speed. The study found that wave diffraction around the ship becomes less profound and the water depth starts to influence the wave loads and ship motions, when increasing the wave length. The added resistance and motions responses of the S175 container ship in multiple wave headings were studied numerically by Kim et al. (2017a). Both 2D and 3D potential-flow methods were used for all headings and CFD was used for head and following seas. The study predicted the sea margin in head sea waves to be 17.2 %. However, none of the above studies systematically compared experimental and numerical re-

sults for seakeeping and added resistance for multiple headings and multiple wave length. A study by Sadat-Hosseini et al. (2015) presented experiments, potential flow, and CFD computations for added resistance for variable headings and wave lengths for the KCS. However, CFD simulations were only conducted for one wave length. They found that the potential-flow method captures the heave and pitch motions well. However, surge, roll, and added resistance were not well predicted for most cases. In general, the accuracy of the CFD simulations was better. The reason why CFD simulations were only conducted for one wave length, is that only one wave length was studied at the Tokyo 2015 CFD workshop (Hino et al., 2020). The Tokyo 2015 CFD workshop had a test case, where participants submitted CFD results of motion responses and added resistance for 5 headings and a single wavelength. Only two participants presented their CFD simulations. The first was Iowa Institute of Hydraulic Research (IIHR) using the CFD code CFDSHIP-Iowa (Sadat-Hosseini et al., 2015). The second was University of Zagreb (UZ) using Naval Hydro Pack (Vukcevic and Jasak, 2016). Both participants showed fair prediction of the motions responses, but the discrepancy of added resistance between the CFD simulations and experiments were up to 100 %. Considering the increasing popularity of CFD modelling in ship hydrodynamics and its potential capacity to model a more complex phenomenon that an ordinary PF approach cannot handle, e.g. water entry and exit, local wave breaking, viscosities etc., there is a strong need of dedicated verification and validation studies for ships in waves with various heading and wave lengths.

The aim of the present study is to conduct verification and validation studies of CFD simulations of motions responses and added resistance in oblique waves. The present study conducts CFD simulations of the KCS in five headings and six wavelengths. The validation is done by comparing the CFD results with experiments from IIHR (Sadat-Hosseini et al., 2015; Sanada et al., 2021) and FORCE Technology (Simonsen et al., 2013). Only 28 out of the 30 test cases are studied. The shortest wave length  $\lambda/L_{pp} = 0.5$  at  $135^\circ$  and  $180^\circ$  are not studied due to the excessive computational cost. Furthermore, the uncertainties of the experimental data are very large at these two test cases, making conclusion regarding agreement between CFD and experiments difficult.

## 2 METHODOLOGY

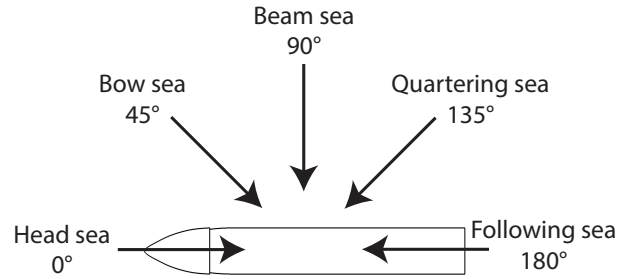
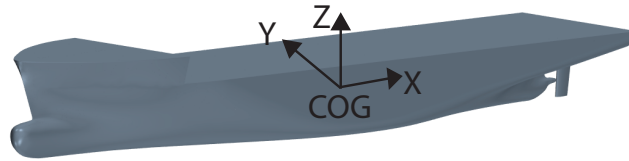
The present Unsteady Reynolds Averaged Navier-Stokes (URANS) CFD simulations are performed with the commercial CFD-code STAR-CCM+ v.2020.1 from Siemens (2020). STAR-CCM+ discretizes the governing equations using an unstructured finite-volume method. The code is widely used in the marine industry and is well known for its capabilities within marine applications. The CFD model has previously been validated for calm water resistance calculations in both model and full-scale (Mikkelsen et al., 2019; Mikkelsen and Walther, 2020).

### 2.1 KCS and Towing Tank Test

The studied ship is the KCS. The main particulars of the KCS can be seen in Table 1. The KCS is chosen since both experimental data and the hull geometry is publicly available. A definition of the five studied wave headings is illustrated in Figure 1. The present study uses the same ship-fixed coordinate system used by IIHR (Sadat-Hosseini et al., 2015; Sanada et al., 2021) and is seen in Figure 2. The towing tank tests at IIHR are conducted in a  $40\text{ m} \times 20\text{ m} \times 3\text{ m}$  wave basin (Sadat-Hosseini et al., 2015). Unless otherwise mentioned, this same model scale described in Table 1 will be used in all analyses in this paper. The towing tank tests in  $0^\circ$  heading by FORCE Technology are conducted with a longer  $L_{pp} = 4.37\text{ m}$  model in a  $240\text{ m} \times 12\text{ m} \times 5.5\text{ m}$  wave basin.

**Table 1:** Main particulars.

Name	Symbol	Value
Length between perpendiculars	$L_{pp}$	2.7 m
Beam	$B$	0.378 m
Draft	$T$	0.1268 m
Displacement	$\Delta$	84.00 kg
Speed	$U$	$1.34 \text{ m s}^{-1}$
Vertical center of gravity (from keel)	$KG$	0.168 m
Longitudinal radius of gyration	$k_{xx}$	$0.39 B$
Transverse radius of gyration	$k_{yy}$	$0.25 L_{pp}$

**Figure 1:** Studied wave headings.**Figure 2:** KCS ship geometry and coordinate system.

## 2.2 Governing Equations

The governing equations of an incompressible Newtonian fluid are the Navier-Stokes equations (Ferziger and Peric, 2002):

$$\frac{\partial u_j}{\partial x_j} = 0 \quad (1)$$

$$\rho \frac{\partial u_i}{\partial t} + \rho u_j \frac{\partial u_i}{\partial x_j} = -\frac{\partial p}{\partial x_i} + \frac{\partial}{\partial x_j} \left( 2\mu S_{ij} - \rho \overline{u'_j u'_i} \right) + f_i \quad (2)$$

where  $u_i$  is the velocity vector,  $t$  is time,  $p$  is pressure,  $\mu$  is dynamic viscosity,  $S_{ij} = \frac{1}{2} \left( \frac{\partial u_i}{\partial x_j} + \frac{\partial u_j}{\partial x_i} \right)$  is the mean strain rate,  $u'_i$  is the turbulent fluctuating part of the velocity, and  $f_i$  is body forces including gravity and wave forcing.

In order to close the problem the Reynolds stresses are modelled using a linear eddy viscosity model. The linear constitutive relationship (Wilcox, 1998) is:

$$-\rho \overline{u'_i u'_j} = 2\mu_t S_{ij} - \frac{2}{3}\rho k \delta_{ij} \quad (3)$$

where  $\mu_t$  is the turbulent viscosity,  $k$  is the turbulent kinetic energy, and  $\delta_{ij}$  is Kronecker's delta.

In this study the turbulent viscosity is calculated using the realizable  $k$ - $\epsilon$  turbulence model (Shih et al., 1995; Siemens, 2020). The  $k$ - $\epsilon$  model is a two equations model based on the turbulent kinetic energy  $k$  and the turbulent dissipation rate  $\epsilon$  (Wilcox, 1998):

$$\mu_t = \rho C_\mu \frac{k^2}{\epsilon} \quad (4)$$

where  $C_\mu$  is an empirical constant.

The free surface is resolved using the Volume Of Fluid (VOF) method in STAR-CCM+ (Hirt and Nichols, 1981; Siemens, 2020). Hence, the volume fraction  $\alpha$  is assigned and evolves in time with the following transport equation:

$$\frac{\partial \alpha}{\partial t} + \frac{\partial}{\partial x_j} (\alpha u_j) = 0 \quad (5)$$

The transport equation is solved using the High-Resolution Interface Capturing scheme (Muzaferija and Perić, 1997). The effective fluid properties are weighted using the volume fraction:

$$\rho = \alpha \rho_w + (1 - \alpha) \rho_a \quad (6)$$

$$\mu = \alpha \mu_w + (1 - \alpha) \mu_a \quad (7)$$

where  $\rho_w$  is the density of the water phase,  $\rho_a$  is the density of the air phase and  $\mu_w$  and  $\mu_a$  are the corresponding dynamic viscosities. For all simulations, the schemes for the convective and diffusive terms are 2<sup>nd</sup>-order. The solver for the temporal discretization is a second-order implicit scheme, and the convective Courant number is kept below 0.5 on the free surface. For each time step, eight inner iterations are used to ensure convergence of the non-linear equations.

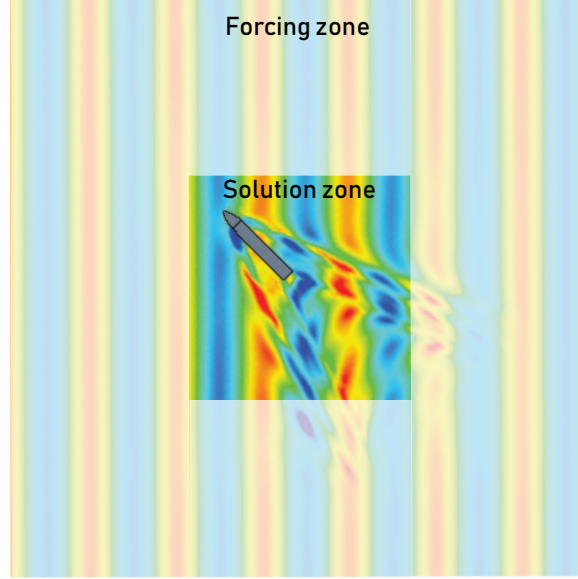


**Figure 3:** Forcing zone, solution zone and wave elevation for  $45^\circ$  heading and  $\lambda/L_{pp} = 1$ .

### 2.3 Computational Domain and Wave Generation

The shape of the CFD domain is a rectangular box. The top of the domain is set to a pressure outlet in order to allow the air flow to evolve freely. All vertical sides are velocity inlets. When all vertical sides are velocity inlets and not pressure outlets, the heading of the ship can be allowed to change in future manoeuvring simulations. The modelled water depth in the CFD model is 3 m, which is the same as that in the model tests. Since the longest wave length considered in our study is 5.4 m, it is not expected that the water depth has any important effects on the seakeeping and added resistance of the ship. Therefore, the bottom of the domain is treated as a velocity inlet.

The total computational domain contains two parts, namely the forcing zone (or relaxation zone) and the solution zone, see Figure 3 for an illustration. The forcing zone at the outer layer of the computational domain is used to generate the incident regular waves. A smooth-transition function in the form of  $\cos^2(x)$  is applied within the forcing zone, so that the flow solution is enforced to be the same as the prescribed incident waves at the outer boundaries (the 4 vertical boundaries), while the forcing becomes zero at the end of the forcing zone, i.e. close to the boundary of the solution zoom. The forcing zone also acts as a wave absorbing zone due to the relaxation of the solution towards the targeted incident wave solution at the outer boundaries. In this paper, Stokes fifth-order waves are used as input waves, which are available from the built-in wave module in STAR-CCM+. The steepness of the incident wave is 1.7% in order to match the experimental data provided in (Sadat-Hosseini et al., 2015; Sanada et al., 2021). The width of the forcing zone is equal to two times the wavelength of the incident wave. The influence of the forcing zone width has been studies in detail. It is found that a forcing zone width of two incident wavelengths is a good compromise between numerical diffusion, wave reflection and computational cost. A forcing zone width of only one incident wavelength caused significant reflection (not shown). The inner volume, where no forcing is applied, is denoted the solution zone. The size of the solution zone is slightly different for each heading because the combination of generated steady Kelvin wave pattern and unsteady diffraction and radiation waves is different for each heading. However, the size of the solution zone is the same for all wavelength for a given heading. A size of the solution zone of approximately  $3L_{pp} \times 3L_{pp}$  is chosen, so it is enough not to influence the added resistance and seakeeping.

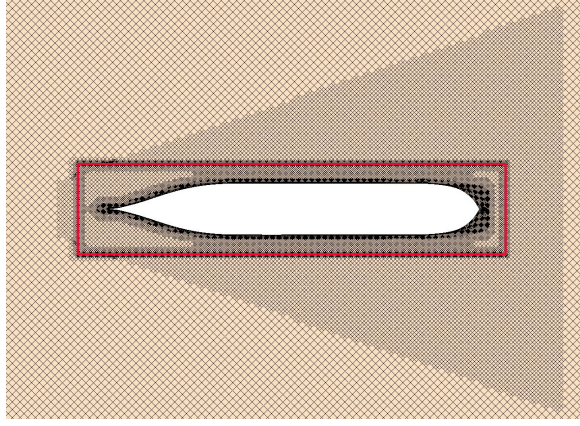


**Figure 4:** Mesh on the free surface seen from the top for  $45^\circ$  heading and  $\lambda/L_{pp} = 1$ . The overset boundary is shown in red. Volumetric refinement is seen to resolve the generated Kelvin waves.

## 2.4 Mesh

The mesh consists of a background region and an overset region. The size of the overset domain is determined, so there is always minimum 5 cells from the surface of the ship to the overset boundary. This is recommended by Siemens (2020), in order to ensure that the overset solver accurately can exchange information between the background domain and the overset domain. The size of the overset domain can be seen in Figure 4. The volume mesh consists of hexahedrons in an unstructured grid. The mesh is generated using the trimmer-mesh function in STAR-CCM+ and is aligned with the wave direction. The boundary layer mesh, also called the prism layer mesh, is used on the hull surface in order to ensure accurate estimation of the wall shear stress within the wall function approximation. Three prism layers are used on the ship hull. The quality of the prism layers are inspected to ensure high quality and good transition from the outer prism layer to the core mesh. The wall  $y^+$ -values on the hull are mostly in the range of 30–200. The mesh is refined in the important zones including the free surface, near the ship and in the overset overlapping zone. The built-in overset adaptive mesh refinement module in STAR-CCM+ is used to ensure equal cell sizes in the overlapping region between the background and overset mesh. The mesh on the free surface can be seen in Figure 4. The mesh including the ship is moving with constant horizontal speed of 1.34 m/s.

## 2.5 Motions

In the IIHR experiments (Sadat-Hosseini et al., 2015; Sanada et al., 2021), the ship is fixed in  $z$ -rotation (yaw) and  $y$ -translation (sway). A spring-mass system is used in the experiments in the  $x$ -direction (surge), as described by Sadat-Hosseini et al. (2015). However, the surge motions are small (less than  $1\%L_{pp}$ ) and for the Tokyo CFD workshop (Hino et al., 2020), which the experiments are made for, it was recommended to constrain the surge in the numerical studies. Therefore, the aim is to make a CFD model, where only the ship is free in  $z$ -translation (heave),  $y$ -rotation (pitch) and  $x$ -rotation (roll). In the CFD model, the heave, pitch, and roll motions of the vessel are solved using the Dynamic Fluid Body Interaction (DFBI) Multi Body solver in STAR-CCM+ cf. (Ohmori, 1998; Siemens, 2020) and is applied as a rigid translation and rotation of the overset domain mesh. The DFBI Multi Body solver is chosen for its stability and accuracy. Sway is constrained accurately by the motion solver in STAR-CCM+. However, the DFBI solver in STAR-CCM+ version 2020.1 is found to produce an unacceptable drift in the constrained yaw. Besides the drift, it is found that constraining the yaw motion by the built-in motion module in STAR-CCM+ makes the roll response non-physical. Therefore, the surge and yaw motions are constrained using implementations by the authors. The surge motion is constrained by applying a concentrated  $x$ -force at each time step in the center of mass equal to the integrated shear and pressure forces acting on the hull with opposite sign. With this implementation, the speed of the ship never deviates more than 0.1 % from the target ship



speed. Since the integrated  $x$ -force is calculated each time step, the implementation allows the ship speed to be non-constant in future studies of, for instance, manoeuvring simulations in waves and self-propulsion simulations in waves. The yaw motion is constrained by applying a concentrated  $z$ -moment and a torsional spring around the  $z$ -axis of the ship. The magnitude of the applied concentrated  $z$ -moment is equal to the integrated  $z$ -moment of the ship with opposite sign. The torsional spring constant is set to 20 kNm/deg in order to ensure a small yaw angle and a natural yaw frequency far from the natural frequencies of the motions and incident waves. The magnitude of the concentrated  $z$ -moment is approximately 50 times larger than the  $z$ -moment from the torsional spring. With this implementation, the simulated yaw angle never exceeds 0.01 deg and it is found not to influence the other motions.

## 2.6 Post-Processing of the Results

The main output from the simulations are time histories of heave ( $Z$ ), pitch ( $\theta$ ), roll ( $\phi$ ), and total resistance ( $R$ ). The resistance is the integrated shear stress and pressure on the hull in the  $x$ -direction. An example of a resistance time history is shown in Figure 5. From an instant, where the solution ( $s(t)$ ) has periodically steady outputs, an integer number of encounter periods ( $T_e$ ) are fitted to a 4-term Fourier series:

$$s(t) = a_0 + a_1 \cos(\omega_1 t) + b_1 \sin(\omega_1 t) + \dots + a_4 \cos(\omega_4 t) + b_4 \sin(\omega_4 t) \quad (8)$$

where  $\omega_k = 2\pi f_e k$ , and  $f_e$  is the encounter frequency. Each fit is visually inspected to ensure that the fit is representative of the time history and that the fitting window does not start before the time history has stabilized. For the time history shown in Figure 5, the fit only uses the time history for  $t/T_e = 9 - 15$ . Based on the Fourier coefficients from these fits, the amplitudes ( $A_k$ ) for heave, pitch, roll, and resistance are calculated using:

$$A_k = \sqrt{a_k^2 + b_k^2} \quad (9)$$

where  $k$  is the Fourier term.

The same procedure is used in the Tokyo workshop (Hino et al., 2020) allowing for direct comparison. The present study only focuses on the added resistance and the first amplitude of heave ( $Z_1$ ), pitch ( $\theta_1$ ), roll ( $\phi_1$ ). The added resistance ( $\sigma_{aw}$ ) is defined as

$$\sigma_{aw} = \frac{R_0 - R_{CW}}{\frac{\rho A^2 B^2}{L_{pp}}} \quad (10)$$

where  $R_0$  is the zero-th amplitude (mean) resistance using Equation (8) and  $R_{CW}$  is the calm water resistance.

For the validation, the amplitudes are non-dimensionalized with the incident wave amplitude that actually reaches the ship and not the target wave amplitude, which is specified at the domain boundaries. The added resistance will also be calculated using the actual wave amplitude.

## 2.7 Grid Convergence Index

For the verification study of the CFD model, the discretization error is estimated using the Grid Convergence Index (GCI) method (Celik et al., 2008) which is based on Richardson extrapolation, cf. (Richardson, 1910; Richardson and Gaunt, 1927). The apparent order ( $p$ ) is calculated by:

$$p = \frac{1}{\ln(r_{21})} \left| \ln \left| \frac{\epsilon_{32}}{\epsilon_{21}} \right| + q(p) \right| \quad (11)$$

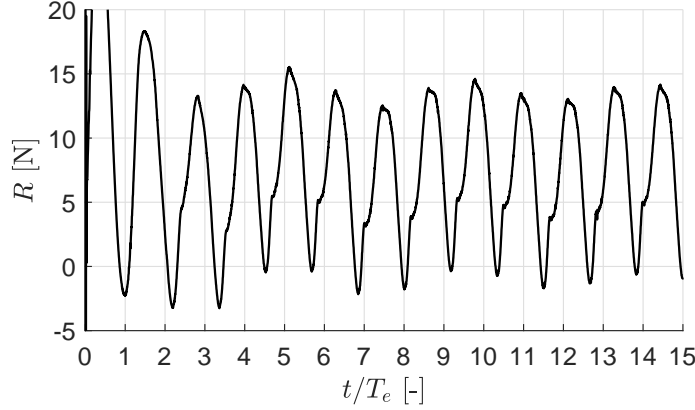


**Figure 5:** Time history of the measured resistance ( $R$ ) as function of time non-dimensionalized with encounter period ( $T_e$ ) at  $45^\circ$  heading and  $\lambda/L_{pp} = 1$ .

$$q(p) = \left( \frac{r_{21}^p - s}{r_{32}^p - s} \right) \quad (12)$$

$$s = \text{sgn}(\epsilon_{32}/\epsilon_{21}) \quad (13)$$

where  $r$  are refinement ratios,  $\epsilon_{32} = \phi_3 - \phi_2$ ,  $\epsilon_{21} = \phi_2 - \phi_1$ ,  $s$  is a sign indicator, and  $\phi_k$  denotes the solution on the  $k$ -th mesh.  $q(p) = 0$  for  $r = \text{const}$ . The extrapolated asymptotic value is calculated as:

$$\phi_{ext}^{21} = \frac{r_{21}^p \phi_1 - \phi_2}{r_{21}^p - 1} \quad (14)$$

Different error estimates can now be calculated. The approximate relative error is:

$$e_a^{21} = \left| \frac{\phi_1 - \phi_2}{\phi_1} \right| \quad (15)$$

$$e_a^{31} = \left| \frac{\phi_1 - \phi_3}{\phi_1} \right| \quad (16)$$

The extrapolated relative error is:

$$e_{ext}^{21} = \left| \frac{\phi_{ext}^{12} - \phi_1}{\phi_{ext}^{12}} \right| \quad (17)$$

The GCI for the fine and medium mesh is calculated as follows using the safety factor of 1.25 recommended by Roache (1998):

$$GCI_{Fine}^{21} = \frac{1.25 e_a^{21}}{r_{21}^p - 1} \quad (18)$$

Equation (18) is extended to the GCI for the medium and coarse mesh:

$$GCI_{Medium}^{21} = \frac{1.25 e_a^{21} r_{21}^p}{r_{21}^p - 1} \quad (19)$$

$$GCI_{Coarse}^{31} = \frac{1.25 e_a^{31} r_{31}^p}{r_{31}^p - 1} \quad (20)$$

The GCI values are used as an estimate of discretization errors, since they are a measure of the relative discrepancy between the computed value and the asymptotic numerical value. Please note that this method does not identify the exact discretization error, but just an estimate (Roache, 1998).

**Table 2:** Frequencies of the natural motions of the ship predicted by the present CFD model.

Roll, without forward speed	$f_\phi$	0.27 Hz
Roll, frequency with forward speed	$f_{\phi,U}$	0.33 Hz
Heave/pitch, without forward speed	$f_{Z\theta}$	1.11 Hz
Heave/pitch, with forward speed	$f_{Z\theta,U}$	1.05 Hz

### 3 RESULTS

This section consists of five subsections. Firstly, motion decay studies of heave, pitch, and roll. Secondly, a verification study of the estimated spatial and temporal discretization errors of the CFD model estimating the motions responses and added resistance in oblique waves. Thirdly, a verification of the wave generation in the empty CFD tank is conducted to study the loss of incident wave amplitude when progressing the waves in an empty CFD wave tank. Fourthly, the results of the verified CFD model are validated by comparison with experimental results and other available numerical results from the literature. Lastly, the present CFD results as function of the wave heading and wavelength are discussed.

#### 3.1 Motion Decay Studies

Heave, pitch, and roll decays are conducted in CFD using the input specified in Table 1. Decay tests are performed both with and without forward speed. The results of the decay tests are shown in Table 2 and the results without forward speed are similar to the results by Sanada et al. (2021). Sanada et al. (2021) does not present natural motion frequencies with forward speed. However, the natural roll period in Sadat-Hosseini et al. (2015) is 0.23 Hz, which is approximately 15 % lower than what is found in the present CFD calculations and in the experiments by Sanada et al. (2021). The reported gyroscopic radius  $k_{xx}$  is the same in all studies. The reason for this discrepancy is unknown. It is found that the natural roll frequency increases approximately 22 %, when forward speed is included. Furthermore, the natural heave and pitch frequency is decreasing with approximately 5 % with a forward speed of 1.24 m/s. The 22 % increase of the roll period is significant. Similar results are found by Irkal et al. (2019). Ikeda et al. (1978) discusses the influence of the different roll damping coefficients at forward speed. The natural frequencies together with encounter frequencies of the studies cases can be seen in Figure 6.

#### 3.2 Verification of Mesh and Time Step

The verification studies are conducted for a wavelength of  $\lambda/L_{pp} = 1.00$  at  $45^\circ$  heading. This is considered one of the most challenging test cases for the CFD solver. This test case has very large motions and added resistance partly due to fact that the encounter period is close the natural pitch and heave periods as seen in Figure 6. For both the mesh and time step convergence studies, the mean of the resistance signal and first-order amplitudes of the dimensional heave, pitch, and roll signal are analysed. The results will not be non-dimensionalized. This causes the estimated spatial and temporal discretization errors to include both the sensitivity of the resolution on the effect of loss of incident wave amplitude and on the motion responses and local flow around the ship.

##### 3.2.1 Mesh Convergence Study

Three meshes are tested to estimate the spatial discretization error using the GCI procedure described in Section 2.7. The refinement ratios are determined using the cubic root of the total cell count for each mesh. The three meshes are generated by changing the base size, which affects the size of all cells besides the prism layer cells. A constant aspect ratio of eight is chosen between horizontal and vertical

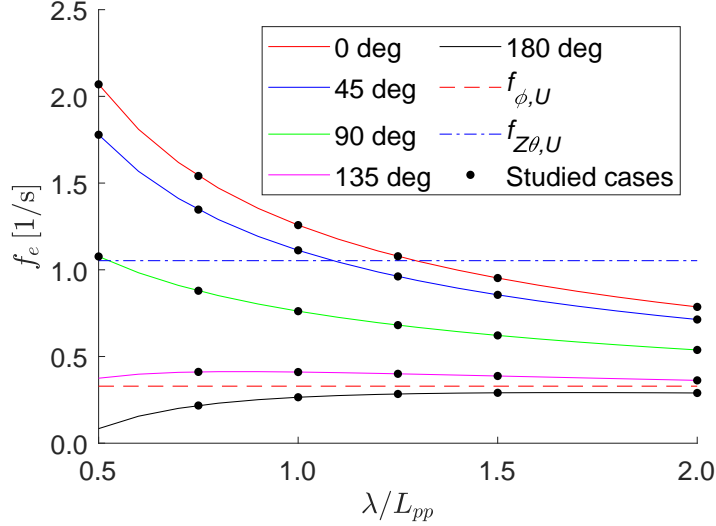


**Figure 6:** Encounter frequency ( $f_e$ ) as function of non-dimensional wave length for different headings. The horizon lines are the natural roll frequency ( $f_{\phi,U}$ ) and natural heave/pitch frequency ( $f_{Z\theta,U}$ ).

**Table 3:** Grid convergence index values for the estimated spatial discretization error for heave ( $Z_1$ ), pitch ( $\theta_1$ ), and roll ( $\phi_1$ ), respectively. The simulation time is based on 80 cores using Intel Xeon Gold 6242R CPUs.

	Number of cells	Simulation time	$Z_1$	$\theta_1$	$\phi_1$
Mesh 1	$12.7 \times 10^6$	70 hours	0.7 %	0.1 %	2.7 %
Mesh 2	$6.7 \times 10^6$	40 hours	1.7 %	0.2 %	4.4 %
Mesh 3	$1.5 \times 10^6$	6 hours	13.8 %	15.6 %	14.0 %

grid spacing in the free surface refinement zone. For all mesh convergence simulations, a time step equal to 750 time steps per incident wave period is used. With this time step size, the Courant number on the free surface for all meshes is well below the value of 0.5 as suggested by Siemens (2020). The obtained GCI's are shown in Table 3. Mesh 2 has 68 cells per wavelength and 9 cells per wave height in the free surface refinement zone. This is slightly fewer cells than what is recommended by Siemens (2020). However, Mesh 1 has 90 cells per wavelength and 12 cells per wave height and the influence on the results is less than 2 %, as seen in Table 3. Mesh 1 has approximately double as many cells as Mesh 2. Furthermore, the estimated spatial discretization errors of Mesh 2 are smaller than the average standard deviation of the experiments by Sanada et al. (2021). Because of this, it is decided to use Mesh 2 settings for all further simulations, since it is considered the best compromise between spatial discretization errors and computational cost. Please note that the mesh settings will result in a larger number of cells for the shorter waves and fewer cells for the longer waves. This is because the size of the solution zone is the same for all waves for a given wavelength, where the width of the forcing zone is equal to two incident wavelengths. The difference in resistance between Mesh 1 and Mesh 3 is less than 0.3 % even though there is more than 8 times more cells in Mesh 1. The resistance using Mesh 2 is 2.3 % higher than when using Mesh 1. This indicates a low sensitivity to the mesh. However, the GCI method considers this oscillatory convergence behaviour. With oscillatory convergence behaviour, the resulting GCIs for resistance become very large, even though the differences in resistance between the three meshes are small. However, this very large GCIs are not considered representative for the spatial discretization error for the resistance. This is an indication that the GCI approach has its limitations. As discussed in Section 2.7 and by Roache (1998), the GCI approach only gives estimations of the discretization errors and not the exact discretization errors.

**Table 4:** Grid convergence index values for the estimated temporal discretization error for heave ( $Z_1$ ), pitch ( $\theta_1$ ), roll ( $\phi_1$ ), and resistance ( $R$ ). The simulation time is based on 80 cores using Intel Xeon Gold 6242R CPUs.

Time steps per wave period	Simulation time	$Z_1$	$\theta_1$	$\phi_1$	$R$
1200	64 hours	0.2 %	0.0 %	0.2 %	0.3 %
750	40 hours	1.1 %	0.0 %	0.5 %	0.7 %
500	27 hours	5.7 %	2.4 %	0.5 %	1.3 %

### 3.2.2 Time Step Convergence Study

In order to quantify the temporal discretization error, simulations are conducted with varying time step sizes using the settings from Mesh 2 from the previous subsection. It is decided to non-dimensionalize the time step with the incident wave period and not the encounter period, since the incident wave period is independent of wave heading. Three time step sizes are tested to estimate the temporal discretization errors using the GCI procedure described in Section 2.7. The results in Table 4 show in general quite low estimated temporal discretization errors. Based on the results, it is decided to use a time step corresponding to 750 time steps per incident wave period for all cases, since the estimated temporal discretization errors are less than 1.2 % for all motion responses and added resistance in the convergence study. This time step is considered the best compromise between computational cost and temporal discretization error. To use 750 time steps per incident wave period will cause a higher number of time steps per encounter period for the  $90^\circ$ ,  $135^\circ$ , and  $180^\circ$  headings, since the encounter periods are 30 – 400 % larger for these headings. Therefore, 750 time step per incident wave period is considered a conservative choice of time step size. The encounter periods for the  $0^\circ$  heading are only 9 – 14 % smaller than for the  $45^\circ$  heading. This is considered small enough not to influence the sensitivity of the time step. Furthermore, the verification study is conducted for a test case, where the encounter frequency is close to the natural heave and pitch frequency causing complex flow phenomena and strong variation in time. The sensitivity of the time step is considered higher at this resonance test case than a non-resonance test case. The sum of the spatial and temporal discretization errors is less than 5 %, which is less than the average standard deviation of the experiments by Sanada et al. (2021).

### 3.3 Verification of empty wave tank

Numerical diffusion causing loss of incident wave amplitude is a common challenge in CFD when modeling wave propagation over a large distance. In order to quantify the amplitude of the incident wave, when it encounters the ship, simulations of the wave tank without the ship are conducted. The simulations are conducted using the mesh and time step settings found in the previous verification section. The empty wave tank domains have the same sizes and is moving with the ship speed identical to the calculations with the presence of the ship. The wave amplitude is measured at the position, where the ships center of gravity would be. The amplitude is determined using the Fourier fitting procedure described in Section 2.6. The loss of incident wave amplitude in percent can be seen in Table 5. An example of the obtained and target wave profile can be seen in Figure 7. The results show that the wave generation works quite well with the selected settings, including the size of wave forcing zone, forcing strength, computational domain size, and other settings. Besides the shortest waves, most of the test cases have a loss of wave amplitude lower than 4 %. For the shortest wave, the loss of incident wave amplitude is up to 12 %. This illustrates why it is important to non-dimensionalize the motion responses and added resistance with the obtained incident wave amplitude and not the incident wave amplitude specified on the domain boundary. There is a clear tendency that the shorter the wave length, the larger the loss of amplitude. This is because the size of the solution zone is independent of the wavelength. Therefore, the shorter the wave, the larger number of

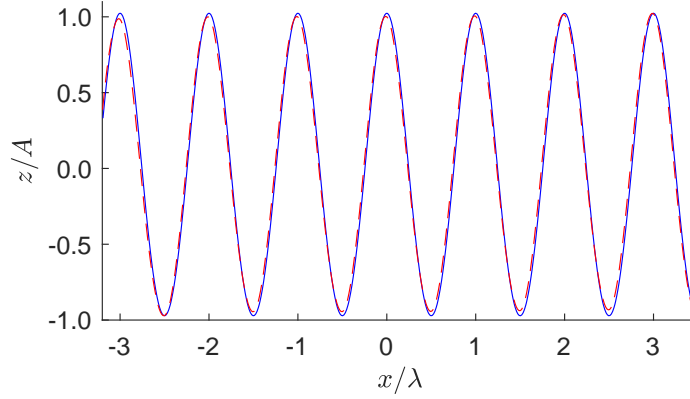


**Figure 7:** Comparison of theoretical (solid blue curve) and actual (red dashed curve) wave profile though the center plan for the  $\lambda/L_{pp} = 1$  wave at  $45^\circ$  heading.

incident waves are present in the solution zone. Due to the presence of numerical diffusion, the larger distance relative between inlet and ship, the more energy is dissipated, leading to larger loss of wave amplitude. This loss could be reduced by choosing a smaller time step and a finer mesh. However, this will increase the computational cost significantly. Another solution could be to use a smaller solution zone. In addition to resolving the unsteady waves, the computational zone has to be sufficiently large to resolve the steady waves generated by the ship and minimize the reflection of the steady waves by the computational boundaries. Since the target steepness of the incident waves are very small and that the added resistance is mainly a second-order effect in wave steepness cf. Faltinsen (1993), it is expected that the loss of incident-wave amplitude has little influences on non-dimensional added resistance (Equation (10)). Therefore, the amplitudes in Table 5 are considered acceptable.

**Table 5:** Loss of incident wave amplitudes in percent at the center of gravity position of the ship for different headings and wavelengths.

		$\lambda/L_{pp}$					
		0.50	0.75	1	1.25	1.50	2.00
Heading	$0^\circ$	12.0 %	7.2 %	3.2 %	2.1 %	1.9 %	1.3 %
	$45^\circ$	11.7 %	6.5 %	2.8 %	1.7 %	1.6 %	1.1 %
	$90^\circ$	10.2 %	3.4 %	2.1 %	0.7 %	1.0 %	0.9 %
	$135^\circ$		5.9 %	2.7 %	1.4 %	1.4 %	1.2 %
	$180^\circ$		6.1 %	2.6 %	1.4 %	1.5 %	1.1 %

### 3.4 Validation

#### 3.4.1 $0^\circ$ Heading

The present CFD model is validated for each of the five studied headings in the following five sections. The present CFD results are compared with up to three sets of Experimental Fluid Dynamics (EFD) data. For all headings, two set of experimental data are from IIHR by Sadat-Hosseini et al. (2015) and Sanada et al. (2021). The study by Sanada et al. (2021) also presents a calculated standard deviations for the  $\lambda/L_{PP} = 1.0$  waves. These standard deviations are included as error bars in Figures 8 to 12. For the  $0^\circ$  heading, results from FORCE Technology by Simonsen et al. (2013) are also included in the comparison as (FORCE). Furthermore, the present CFD results are compared with potential flow (PF) results by Sadat-Hosseini et al. (2015) who used the 3D PF code FATIMA (Bunnik, 1999). At the Tokyo CFD workshop in 2015, only two participants submitted their CFD results for the case with motion responses and added resistance in oblique waves. The first participant is IIHR using the CFD

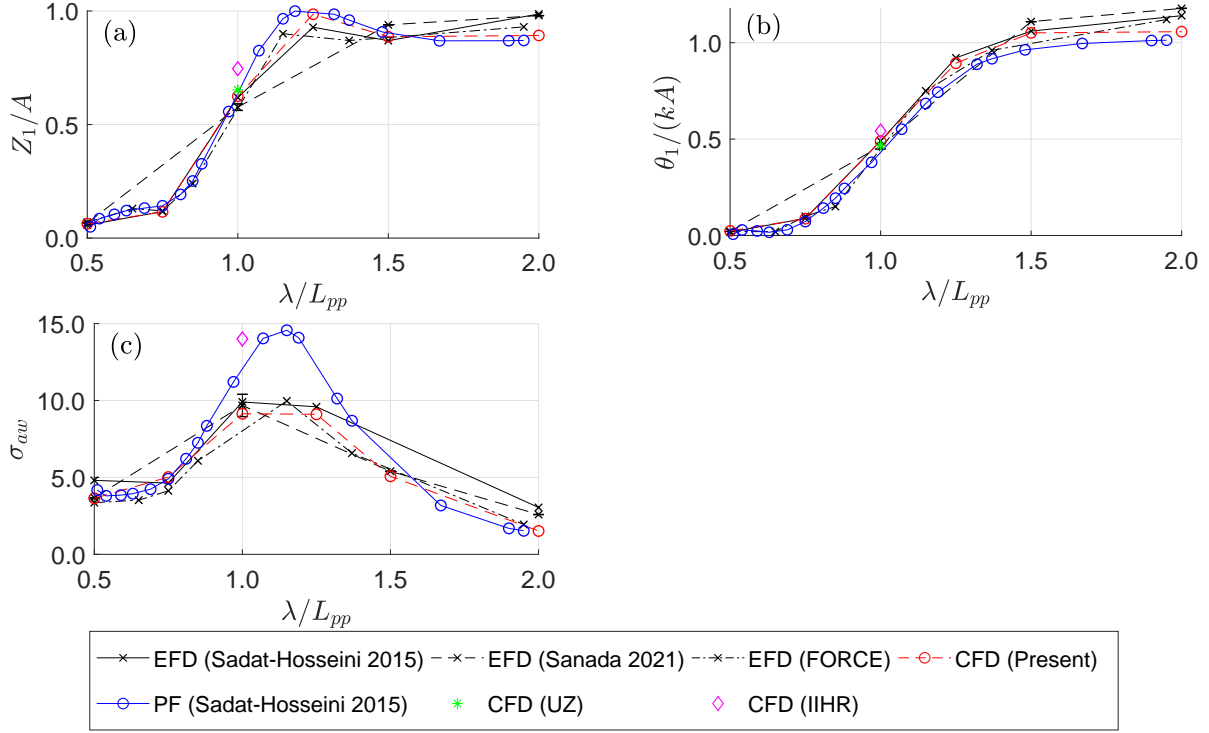


**Figure 8:** Comparison of results for  $0^\circ$  heading as function of non-dimensional wavelength ( $\lambda/L_{pp}$ ). (a) Heave, 1st amplitude ( $Z_1$ ); (b) Pitch, 1st amplitude ( $\theta_1$ ); (c) Added resistance ( $\sigma_{aw}$ ).

code CFDSHIP-Iowa Sadat-Hosseini et al. (2015). The second participant is University of Zagreb (UZ) using Naval Hydro Pack (Vukcevic and Jasak, 2016). Translatory and rotational motion responses are non-dimensionalized by the actual wave amplitude ( $A$ ) from Section 3.3 and wave steepness ( $kA$ ) respectively, where  $k = \frac{2\pi}{\lambda}$ . The added resistance is calculated using Equation (10).

The comparison of the present CFD results, previously reported CFD and PF results, and three sets of experimental data for the  $0^\circ$  heading can be seen in Figure 8. For this heading, the agreement between the three experimental data sets is good. Both the present CFD, UZ CFD and PF motions responses agree very well with the experiments. In general, the present CFD results show slightly better agreement in motion responses than the PF results, especially for the longer waves. As shown in Figure 6, the encounter frequency of the  $\lambda/L_{pp} = 1.25$  wave is very close to the natural heave and pitch frequencies causing resonance. The CFD by IIHR and the PF results overestimates the added resistance near the resonance area with approximately 45 %. However, the added resistance estimated by the present CFD model is within the standard deviation of the experiments by Sanada et al. (2021).

### 3.4.2 $45^\circ$ Heading

Figure 9 shows the comparison of the present CFD results, previously reported CFD and PF results, and two sets of experimental data for the  $45^\circ$  heading. The heave responses shown in Figure 9a, predicted by both the present CFD and PF agree very well with the experiments. The largest deviation is observed for the longest wave. However, the deviation is still smaller than the difference between the two sets of experiments. For the pitch response, shown in Figure 9b, both the present CFD and PF agree well with the experiments for the two shortest waves. For the longer waves, both the PF and the present CFD results approaches an asymptotic limit. The PF agrees excellently with the pitch found in the EFD by Sadat-Hosseini et al. (2015) for all wavelengths and approaches an asymptotic value very similar to the value found by the experiments by Sadat-Hosseini et al. (2015) at  $\lambda/L_{pp} = 2.0$ . The present CFD approaches a value similar to the value found in the experiments by Sanada et al. (2021) at  $\lambda/L_{pp} = 2.0$ . The CFD by UZ predicts the heave and pitch responses well, where the CFD by IIHR overestimates the heave and pitch responses with approximately 10 %. The roll responses

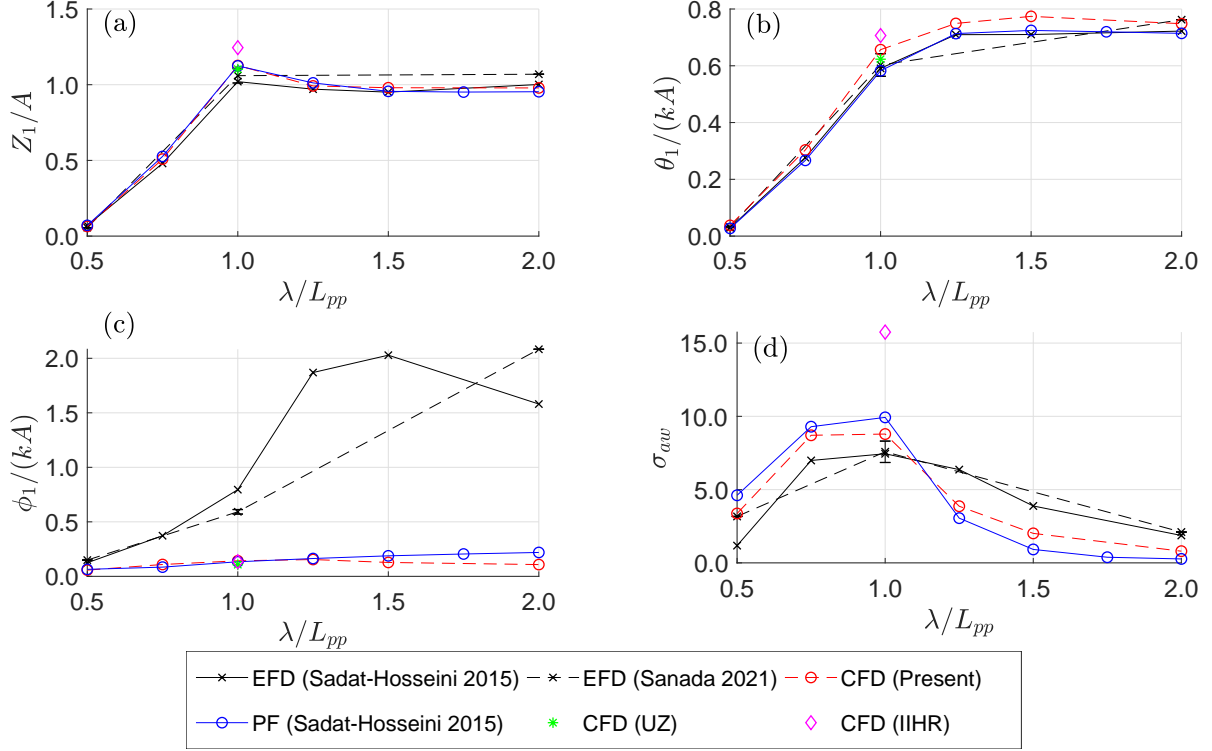


**Figure 9:** Comparison of results for  $45^\circ$  heading as function of non-dimensional wavelength ( $\lambda/L_{pp}$ ). (a) Heave, 1st amplitude ( $Z_1$ ); (b) Pitch, 1st amplitude ( $\theta_1$ ); (c) Roll, 1st amplitude ( $\phi_1$ ); (d) Added resistance ( $\sigma_{aw}$ ).

found in the experiments are much larger than any of the numerical methods as seen in Figure 9c. The roll responses predicted by the PF and all three CFD approaches agrees well with each other, but not with the experiments. Even the smallest encounter frequency of the studied waves in  $45^\circ$  heading is 0.72 Hz. This is more than double the natural roll period (0.33 Hz) with forward speed. It is not clear why the experimental roll responses are about one order of magnitude higher than numerical results. This needs more dedicated experimental studies in the future and is out of the scope of the present study. When the wavelength is increased, the encounter frequency is decreasing for the  $45^\circ$  heading as seen in Figure 6. Therefore, it is expected that the roll responses should only increase slowly while the wavelength is getting larger and the encounter frequency becomes closer to the natural roll frequency. This is the behaviour of all the numerical results in Figure 9c. In general, both the PF and the present CFD overestimates the added resistance at the shorter waves and underestimates the added resistance at the longer waves as seen in Figure 9d. However, the added resistance from the present CFD is closer to the experiments for all wavelengths than the PF results. For the  $\lambda/L_{pp} = 1.0$  wave, the CFD by IIHR overestimates the added resistance with approximately 100 %, where the present CFD overestimates the added resistance with approximately 18 %. The standard deviation of the experimental added resistance by Sanada et al. (2021) is 10.7 % at this wave.

### 3.4.3 $90^\circ$ Heading

For the  $90^\circ$  heading, the comparison of the present CFD results, previously reported CFD and PF results, and two sets of experimental data can be seen in Figure 10. The encounter frequency of the  $\lambda/L_{pp} = 0.5$  wave is close to the natural heave and pitch frequency as see in Figure 6. Therefore, it would be expected to have maximum added resistance, heave and pitch responses at this this wave. Both the present CFD and PF show this trend. However, the experiments only show maximum pitch and added resistance at  $\lambda/L_{pp} = 0.5$  as seen in Figure 10. For heave, shown in Figure 10a, the two experimental results show a maximum heave response at  $\lambda/L_{pp} = 2.0$ . Both the PF and the present



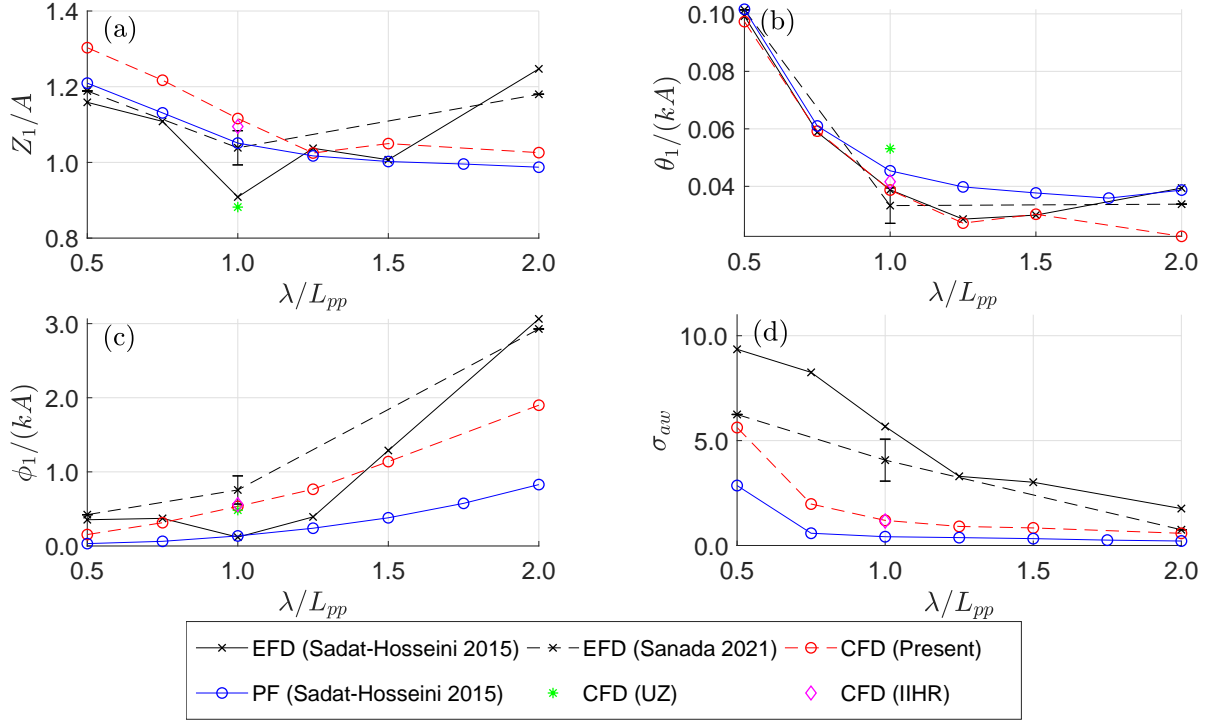


**Figure 10:** Comparison of results for  $90^\circ$  heading as function of non-dimensional wavelength. (a) Heave, 1st amplitude ( $Z_1$ ); (b) Pitch, 1st amplitude ( $\theta_1$ ); (c) Roll, 1st amplitude ( $\phi_1$ ); (d) Added resistance ( $\sigma_{aw}$ ).

CFD show a heave response approaching an asymptotic value close to unity. This is the expected behaviour for long waves that have passed the heave/pitch resonance point. For the heave response, the PF results have a slightly better agreement with the experiments than the present CFD does. However, the present CFD agrees better with the experiments than PF for pitch. The disagreement between the experiments for roll, shown in Figure 10c, is larger than for the heave and pitch. In general, PF underestimate the roll response. This is unexpected since the PF based on the work by Bunnik (1999), which does not include viscous effect and therefore viscous roll damping. It is unknown to the authors, if additional roll damping has been added to the PF calculation presented by Sadat-Hosseini et al. (2015). The roll response predicted by the present CFD are between the experimental results by Sanada et al. (2021) and Sadat-Hosseini et al. (2015) for the  $\lambda/L_{pp} = 1.0$ . The CFD by UZ slightly underestimate the heave and overestimate the pitch relative to the experimental results. The predicted roll response of the UZ CFD is very similar to the present CFD results and the CFD results by IIHR. Both PF and the present CFD underestimates the added resistance as seen in Figure 10d. However, the underestimation by the present CFD is smaller than the underestimation by PF.

#### 3.4.4 $135^\circ$ Heading

The comparison of the present CFD results, previously reported CFD and PF results, and two sets of experimental data for the  $135^\circ$  heading can be seen in Figure 11. The agreement between the two sets of experiments is fair for the three motion responses. However, for the added resistance, the disagreement is large. In general, the predicted motion responses of the three CFD approaches are similar. The heave and pitch responses are very well predicted by both the CFD and PF as shown in Figure 11a and Figure 11b. The roll responses of the shortest waves are predicted very well by the present CFD as seen in Figure 11c. However, for the longer waves, the present CFD overpredicts the roll response. As seen in Figure 6 the encounter frequencies for longer waves at  $135^\circ$  heading are getting close to the natural roll frequency of the ship. Therefore, the roll response is expected to increase, when the wavelength is increased. A possible reason for the disagreement in roll response

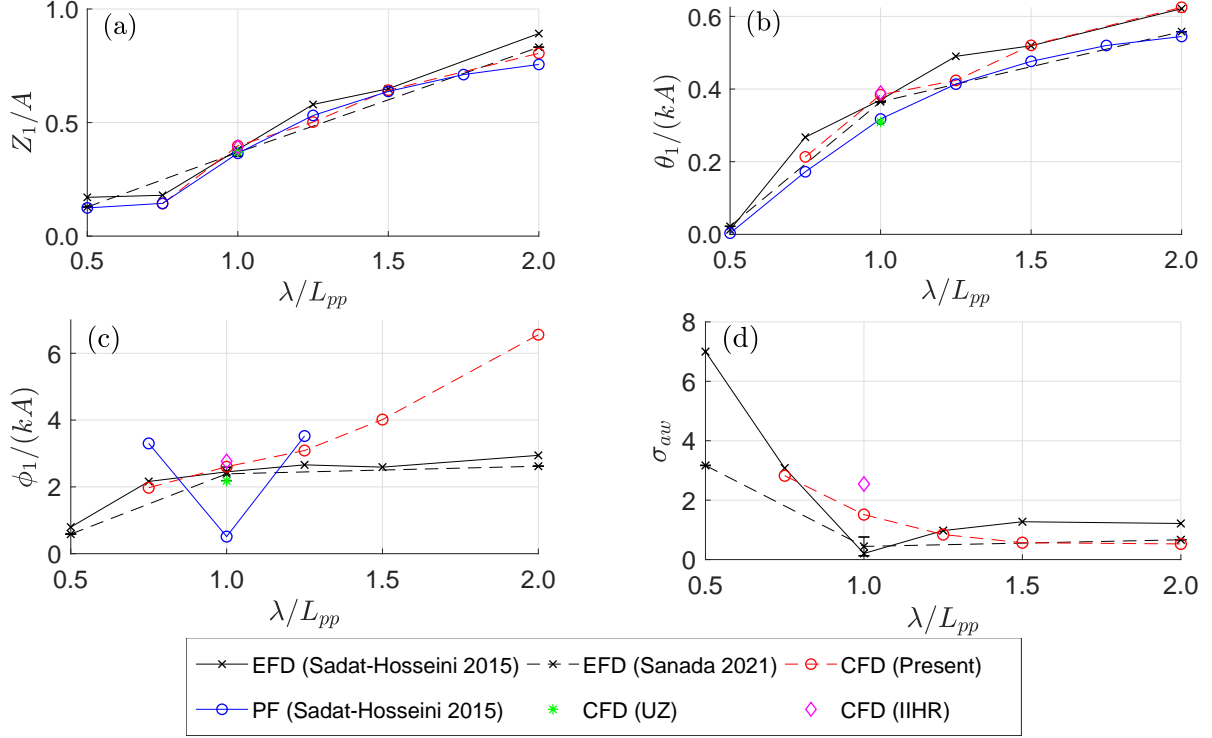


**Figure 11:** Comparison of results for  $135^\circ$  heading as function of non-dimensional wavelength; (a) Heave, 1st amplitude ( $Z_1$ ); (b) Pitch, 1st amplitude ( $\theta_1$ ); (c) Roll, 1st amplitude ( $\phi_1$ ); (d) Added resistance ( $\sigma_{aw}$ ).

between the present CFD and EFD at the long waves, is the underestimation of roll damping by the present CFD. It could also be due to a discrepancy in  $k_{xx}$  and therefore the natural roll frequency. Since the encounter frequency of the  $\lambda/L_{pp} = 2.0$  wave is close to the natural roll frequency, a small difference in the natural roll frequency can have a significant influence on the roll response. The disagreement between PF and experiments for roll responses is significant and the trend of the roll response predicted by PF is difficult to explain. In addition, for roll responses, the PF results are only available for three wave lengths, cf. (Sadat-Hosseini et al., 2015). The agreement between the present CFD and EFD for added resistance, shown in Figure 11d, is good considering the uncertainties of the experiments. Both sets of experimental results show a minimum added resistance at  $\lambda/L_{pp} = 1.0$ . The trend of the present CFD prediction is a more smooth curve approaching an asymptotic value very similar to the EFD value found by Sanada et al. (2021). The overestimation of the CFD by IIHR is larger than the overestimation by the present CFD at  $\lambda/L_{pp} = 1.0$ . PF results for added resistance in  $135^\circ$  heading are not available by Sadat-Hosseini et al. (2015).

### 3.4.5 $180^\circ$ Heading

In general, the encounter frequencies for the waves in the  $180^\circ$  heading are small. Especially the  $\lambda/L_{pp} = 0.5$  wave has a very low encounter frequency, which makes it challenging for the EFD to obtain long enough time series to extract reliable results for added resistance enough due to limited length of the tank. Figure 12 shows the comparison of the motion responses and added resistance predicted by the present CFD model, previously reported CFD and PF, and two sets of experimental data for the  $180^\circ$  heading. The agreement between the two sets of experimental results is good for the motion responses besides the shortest  $\lambda/L_{pp} = 0.5$ . Therefore, the present CFD simulations have not been conducted for the  $\lambda/L_{pp} = 0.5$  wave. The added resistance found by the two experiments are quite different as seen in Figure 12c. The experiments by Sadat-Hosseini et al. (2015) shows a trend of increasing added resistance, when the wavelength is increased, while the EFD by Sanada et al. (2021) shows the opposite trend of decreasing added resistance. Therefore, it is difficult to comment

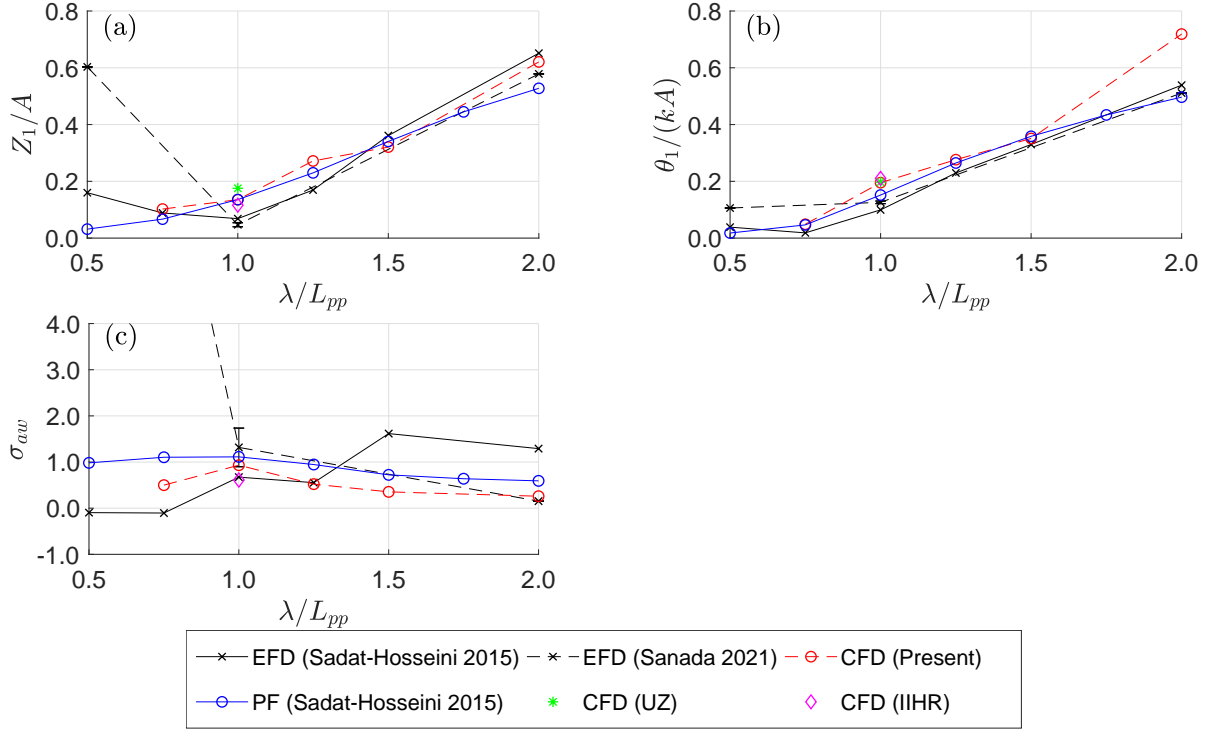


**Figure 12:** Comparison of results for 180° heading as function of non-dimensional wavelength. (a) Heave, 1st amplitude ( $Z_1$ ); (b) Pitch, 1st amplitude ( $\theta_1$ ); (c) Added resistance ( $\sigma_{aw}$ ).

on the agreement of added resistance between CFD and EFD at the 180° heading. However, it can be concluded that the discrepancy between CFD and EFD is similar or smaller than the discrepancy between the two sets of experiments. More experiments with lower uncertainty are required in order to be able to validate results of numerical tools for the 180° heading. In general, the predicted motion responses of the three CFD approaches are similar. The predicted heave and pitch responses by PF and CFD are in good agreement with the experiments as seen in Figure 12a and Figure 12b. However, the pitch response for the  $\lambda/L_{pp} = 2.0$  wave is overpredicted by the present CFD.

### 3.4.6 Influence of Wave Heading

The predicted motion responses and added resistance by the present CFD model as function of wave heading and wavelength are shown in Figure 13. The heave results seen in Figure 13a show a general trend of approaching an asymptotic value close to unity for the long waves. This is expected because when the waves are much longer than the ship, the ship will simply follow the wave elevation. When the waves are very short, the heave response will approach zero, since the waves are too short to excite the motions of the ship. The heave responses for the 90° heading have a maximum heave response at  $\lambda/L_{pp} = 0.5$ , since the encounter frequency is very close to the natural heave frequency as seen in Figure 6. If shorter waves were to be tested in the 90° heading, it would be expected that the heave response would decrease and approach zero similarly to the behaviour in other headings. The encounter frequency of the  $\lambda/L_{pp} = 1.25$  wave at the 0° heading and the  $\lambda/L_{pp} = 1.0$  wave at the 45° heading are also close to the natural heave frequency. This is why the heave responses are maximum at those waves as seen in Figure 13a. The heave responses in the 135° heading and especially the 180° heading are smaller in magnitude than the other headings since the encounter frequencies are further away from the natural heave frequency as seen in Figure 6.

The results for the pitch responses on Figure 13b show minimum pitch response at the shortest  $\lambda/L_{pp} = 0.5$  wave for all headings besides the 90° heading. As in the case for heave, this is caused by the similarity of the encounter frequency of the  $\lambda/L_{pp} = 0.5$  at the 90° heading and the natural pitch frequency, which is approximately the same as the natural heave frequency. For shorter waves than

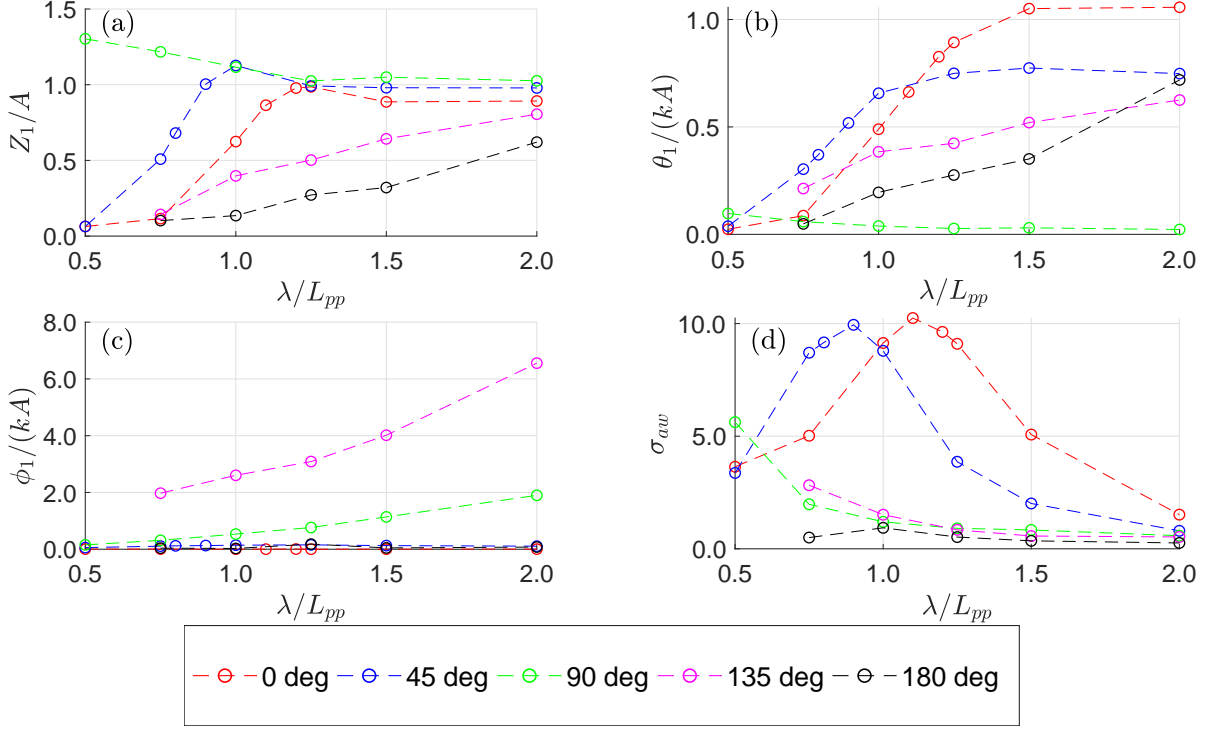


**Figure 13:** Present CFD results as function of wave heading and non-dimensional wavelength ( $\lambda/L_{pp}$ ). (a) Heave, 1st amplitude ( $Z_1$ ); (b) Pitch, 1st amplitude ( $\theta_1$ ); (c) Roll, 1st amplitude ( $\phi_1$ ); (d) Added resistance ( $\sigma_{aw}$ ).

$\lambda/L_{pp} = 0.5$ , the pitch response is expected to approach zero similarly to the other headings, since the waves become too short to cause a pitching moment to the ship. However, the magnitude of the pitch responses in  $90^\circ$  are very small, since the ship is sailing in beam sea, where the wave length is very long relative to the beam of the ship. The observed pitch is caused by the fact that the ship is not bow-stern symmetric and because the forward speed effect leads to asymmetric pressure distribution at bow and stern. For long waves, the pitch responses for the  $0^\circ$  heading approach an asymptotic value close to one. The pitch responses for the  $180^\circ$  are expected to do the same for longer waves than the ones presently studied. For long waves, the pitch responses for the  $45^\circ$  and  $135^\circ$  heading approach an asymptotic value close to  $1/\sqrt{2}$ , since only half of the wave energy contribute to pitch motion at these headings.

The roll responses in Figure 13c show very small roll responses at the  $0^\circ$  and  $180^\circ$  heading. This is consistent with the symmetry along the center plane at these headings. The roll responses for the  $45^\circ$  heading are very small, because the encounter frequencies in this heading are much smaller than the natural roll frequency as seen in Figure 6. The roll responses for the  $90^\circ$  and  $135^\circ$  headings are increasing, when the wavelength is increased. This is because the encounter frequency is getting close to the natural roll frequency, when the wavelength is increased. The roll responses for the  $135^\circ$  heading are larger than for the  $90^\circ$  since the encounter frequencies of the studied waves at the  $135^\circ$  heading are closer to the natural roll frequency than the studied waves for the  $90^\circ$  heading.

Figure 13d shows the added resistance as function of wave heading and non-dimensional wavelength. Compared with the results presented in the previous sections, two extra results for the  $0^\circ$  and  $45^\circ$  headings are also included to better capture peak values of the added resistance curves. The maximum added resistance for the  $90^\circ$  heading is observed for the  $\lambda/L_{pp} = 0.5$  wave. As mentioned previously, this wave has an encounter frequency very close to the natural heave and pitch frequencies causing large heave and pitch responses and added resistance at this wave. The maximum added resistance for the studied waves with a heading of  $135^\circ$  is found for the  $\lambda/L_{pp} = 0.75$  wave, which is the shortest wave studied at this heading. The added resistance for the studied waves at the  $180^\circ$  heading are small, however still positive.

## 4 CONCLUSION

This study presents a systematic verification and validation of seakeeping responses and added resistance of the KCS container ship in regular oblique waves by using CFD. Convergence studies of both the temporal and spatial discretization errors are presented. Discussions are made to determine affordable time steps and mesh sizes, while keeping the discretization errors acceptable. The surge and yaw motions are constrained by user-implementations in the commercial software, which consist of additions of springs and concentrated forces/moment to cancel the fluid forces and moments. The mesh and time step convergence studies show that the sum of the spatial and temporal discretization errors for an affordable calculation is less than 5 %, which is smaller than the average standard deviation of the experiments by Sanada et al. (2021). A study of the empty wave tank shows that the wave generation showed that the loss of incident wave amplitude due to numerical diffusion of less than 4 % for most of the test cases. 28 test cases are studied with different combinations of wave heading and wavelength. For each test case, the added resistance as well as the heave, pitch, and roll response are compared with previously reported potential flow and CFD results and up to three sets of experimental data. Due to the loss of incident wave amplitude caused by numerical diffusion, the motion and added resistance results are non-dimensionalized based on the actual incident wave amplitude obtained from separate runs in empty wave tank, where similar spatial and temporal discretization is used.

In most cases the discrepancy between the experiments and the present CFD results are within the uncertainty of the experiments. In some cases, especially at  $135^\circ$  and  $180^\circ$  headings, the experimental uncertainty is significant. In general, both the previously reported potential flow calculations and present CFD simulations predict the motion responses well. However, the added resistance predicted by the present CFD model is in better agreement with the experiments, than the previously reported potential flow results. Furthermore, the present CFD results in general show significantly better agreement with the experiments than previously published CFD results. The tendencies in the results of the present CFD model matches very well the expected behaviour regarding the natural motion frequencies of the ship. The study has shown that CFD simulations accurately can predict motion responses and added resistance in oblique regular waves. However, further experiments with smaller uncertainties in following sea and stern quartering sea are required, to better support future validations of CFD simulations.

## ACKNOWLEDGEMENT

The research is supported by the Danish Maritime Fund under grant 2018-11, whose support is greatly appreciated.

## REFERENCES

- Bunnik, T. H. J. (1999). *Seakeeping calculations for ships, taking into account the non-linear steady waves*. PhD thesis, Delft University of Technology.
- Celik, I. B., Ghia, U., Roache, P. J., Freitas, C. J., Coleman, H., and Raad, P. E. (2008). Procedure for estimation and reporting of uncertainty due to discretization in CFD applications. *J. Fluids Engng.*, 130:1–4.
- Chuang, Z. and Steen, S. (2013). Speed loss of a vessel sailing in oblique waves. *Ocean Engng.*, 64:88–99.
- Faltinsen, O. (1993). *Sea Loads on Ships and Offshore Structures*. Cambridge University Press.
- Ferziger, J. H. and Peric, M. (2002). *Computational methods for fluid dynamics*. Cambridge University Press, 3 edition.

- Fujii, H. and Takahashi, T. (1975). Experimental study on the resistance increase of a large full ship in regular oblique waves. *J. Soc. Nav. Archit. Japan*, 137:132–137.
- Gong, J., Yan, S., Ma, Q., and Li, Y. (2020). Added resistance and seakeeping performance of trimarans in oblique waves. *Ocean Engng.*, 216:1–19.
- Hino, T., Stern, F., Larsson, L., Visonneau, M., Hirakata, N., and Kim, J. (2020). *Numerical ship hydrodynamics: An assessment of the Tokyo 2015 workshop*. Springer-Verlag.
- Hirt, C. W. and Nichols, B. D. (1981). Volume of fluid (VOF) method for the dynamics of free boundaries. *J. Comput. Phys.*, 39(1):201–225.
- Ikeda, Y., Himeno, Y., and Tanaka, N. (1978). Components of roll damping of ship at forward speed. *J. Soc. Nav. Archit. Japan*, 143:113–125.
- Irkali, M. A. R., Nallayarasu, S., and Bhattacharyya, S. K. (2019). Effect of forward speed on roll damping of a container ship using URANS simulations. *Lect. Notes Civ. Eng.*, 22:187–201.
- Jasak, H., Vukčević, V., Gatin, I., and Lalović, I. (2018). CFD validation and grid sensitivity studies of full scale ship self propulsion. *Int. J. Nav. Archit. Ocean Eng.*, 11(1):33–43.
- Jin, Y., Chai, S., Duffy, J., Chin, C., and Bose, N. (2017). URANS predictions of wave induced loads and motions on ships in regular head and oblique waves at zero forward speed. *J. Fluids Struct.*, 74:178–204.
- Kim, M., Hizir, O., Turan, O., Day, S., and Incecik, A. (2017a). Estimation of added resistance and ship speed loss in a seaway. *Ocean Engng.*, 141:465–476.
- Kim, M., Hizir, O., Turan, O., and Incecik, A. (2017b). Numerical studies on added resistance and motions of KVLCC2 in head seas for various ship speeds. *Ocean Engng.*, 140(May):466–476.
- Kim, Y., Kim, K.-H., Kim, J.-H., Kim, T., Seo, M.-G., and Kim, Y. (2011). Time-domain analysis of nonlinear motion responses and structural loads on ships and offshore structures: development of WISH programs. *Int. J. Nav. Archit. Ocean Eng.*, 3(1):37–52.
- Liu, C., Wang, J., and Wan, D. (2018). CFD computation of wave forces and motions of DTC ship in oblique waves. *J. Offshore Pol. Eng.*, 28(2):154–163.
- Liu, S. and Papanikolaou, A. (2016). Prediction of the added resistance of ships in oblique seas. In *Proceedings of the International Offshore and Polar Engineering Conference*, pages 495–502.
- Mikkelsen, H., Steffensen, M. L., Ciortan, C., and Walther, J. H. (2019). Ship scale validation of CFD model of self-propelled ship. In *MARINE 2019 Computational Methods in Marine Engineering VIII*, pages 718–729.
- Mikkelsen, H. and Walther, J. H. (2020). Effect of roughness in full-scale validation of a CFD model of self-propelled ships. *Appl. Ocean Research*, 99:1–14.
- Molland, A., Turnock, S., and Hudson, D. (2011). *Ship resistance and propulsion*. Cambridge University Press.
- Mousavi, S. M., Khoogar, A. R., and Ghasemi, H. (2020). Time domain simulation of ship motion in irregular oblique waves. *J. Appl. Fluid Mech.*, 13(2):549–559.
- Muzaferija, S. and Perić, M. (1997). Computation of free-surface flows using the finite-volume method and moving grids. *Num. Heat Trans., B*, 32(4):369–384.
- Niklas, K. and Pruszko, H. (2019). Full-scale CFD simulations for the determination of ship resistance as a rational, alternative method to towing tank experiments. *Ocean Engng.*, 190:1–13.

- Ohmori, T. (1998). Finite-volume simulation of flows about a ship in maneuvering motion. *J. Mar. Sci. Tech.*, 3(2):82–93.
- Park, D. M., Kim, Y., Seo, M. G., and Lee, J. (2016). Study on added resistance of a tanker in head waves at different drafts. *Ocean Engng.*, 111:569–581.
- Park, D.-M., Lee, J.-H., Jung, Y.-W., Lee, J., Kim, Y., and Gerhardt, F. (2019). Experimental and numerical studies on added resistance of ship in oblique sea conditions. *Ocean Engng.*, 186:106070.
- Psaraftis, H. N. and Kontovas, C. A. (2014). Ship speed optimization: Concepts, models and combined speed-routing scenarios. *Transp. Res. Part C Emerg. Technol.*, 44:52–69.
- Richardson, L. F. (1910). The approximate arithmetical solution by finite differences of physical problems involving differential equations, with an application to the stresses in a masonry dam. *Phil. Trans. R. Soc. A*, 210:307–357.
- Richardson, L. F. and Gaunt, J. A. (1927). The deferred approach to the limit. Part I. Single lattice. Part II. Interpenetrating lattices. *Phil. Trans. R. Soc. A*, 226:299–361.
- Roache, P. J. (1998). Verification of codes and calculations. *AIAA J.*, 36(5):696–702.
- Sadat-Hosseini, H., Toxopeus, S., Kim, D. H., Sanada, Y., Stocker, M., Otzen, J. F., Toda, Y., and Stern, F. (2015). Experiments and computations for KCS added resistance for variable heading. In *5th World Maritime Technology Conference*, pages 1–15.
- Sadat-Hosseini, H., Wu, P. C., Carrica, P. M., Kim, H., Toda, Y., and Stern, F. (2013). CFD verification and validation of added resistance and motions of KVLCC2 with fixed and free surge in short and long head waves. *Ocean Engng.*, 59:240–273.
- Salvesen, N., Tuck, E., and Faltinsen, O. (1970). Ship motions and sea loads. *Trans. - Soc. Nav. Archit. Mar. Eng.*, 78:250–287.
- Sanada, Y., Simonsen, C., Otzen, J., Sadat-Hosseini, H., Toda, Y., and Stern, F. (2021). *Experimental data for KCS added resistance and ONRT free running course keeping/speed loss in head and oblique waves*, volume 94. Springer-Verlag.
- Shih, T.-H., Liou, W. W., Shabbir, A., Yang, Z., and Zhu, J. (1995). A new  $k-\epsilon$  eddy viscosity model for high Reynolds number turbulent flows. *Computers & Fluids*, 24(3):227–238.
- Siemens (2020). STAR-CCM+ user guide, version 2020.1.
- Simonsen, C. D., Otzen, J. F., Joncquez, S., and Stern, F. (2013). EFD and CFD for KCS heaving and pitching in regular head waves. *J. Mar. Sci. Tech.*, 18:435–459.
- Sprenger, F., Hassani, V., Maron, A., Delefortrie, G., Zwijnsvoorde, T. V., Cura-Hochbaum, A., and Lengwinat, A. (2016). Establishment of a validation and benchmark database for the assessment of ship operation in adverse conditions. In *35th International Conference on Ocean, Offshore and Arctic Engineering*, pages 1–12.
- Storm-Tejsen, J., Yeh, H. Y. H., and Moran, D. D. (1973). Added resistance in waves. *Trans. - Soc. Nav. Archit. Mar. Eng.*, 81:250–279.
- Valanto, P. and Hong, Y. P. (2015). Experimental investigation on ship wave added resistance in regular head, oblique, beam, and following waves. In *Proceedings of the International Offshore and Polar Engineering Conference*, pages 19–26.
- Vukcevic, V. and Jasak, H. (2016). Validation and verification of decomposition model based on embedded free surface method for oblique wave seakeeping simulations. In *Tokyo 2015: A Workshop on CFD in Ship Hydrodynamics*, pages 495–502.

- Wilcox, D. C. (1998). *Turbulence modeling for CFD*. DWC Industries, 2 edition.
- Wu, P.-C., Hossain, M. A., Kawakami, N., Tamaki, K., Kyaw, H. A., Matsumoto, A., and Toda, Y. (2020). EFD and CFD study of forces, ship motions, and flow field for KRISO container ship model in waves. *J. Ship. Res.*, 64(1):61–80.
- Yang, Y., Zhu, R., and Hong, L. (2019). A frequency-domain hybrid HOBEM for motion responses and added resistance of ships sailing in head and oblique waves. *Ocean Engng.*, 194:1–16.





## Chapter 4

### Paper C

# Numerical study of nominal wake fields of a container ship in oblique regular waves

The paper entitled "Numerical study of nominal wake fields of a container ship in oblique regular waves" is accepted by Applied Ocean Research.

Mikkelsen, H., Shao, Y. and Walther, J. H. (2021) Numerical study of nominal wake fields of a container ship in oblique regular waves. *Accepted by Appl. Ocean Research (In production)*

The paper is here reproduced with permission from Elsevier, not for further re-distribution or re-use.

# Numerical study of nominal wake fields of a container ship in oblique regular waves

Henrik Mikkelsen<sup>a</sup>, Yanlin Shao<sup>a</sup> and Jens Honoré Walther<sup>a,b\*</sup>

<sup>a</sup>*Technical University of Denmark, Department of Mechanical Engineering, Nils Koppels Allé, Building 404, 2800 Kgs. Lyngby, Denmark.*

<sup>b</sup>*Swiss Federal Institute of Technology Zurich, Computational Science & Engineering Laboratory, Clausiusstrasse 33, CH-8092 Switzerland*

\* *Corresponding author: jhw@mek.dtu.dk*

---

## Abstract

Accurate estimation of the actual nominal wake behind the ship in waves is important for propeller designers when improving efficiency and minimizing cavitation. The present CFD study investigates the nominal wake fields of the Kriso Container Ship (KCS) in regular waves with wavelength equal to the ship length in five different headings. The ship is sailing at design speed and the wave steepness is  $1/60$ . The results show that when sailing in the studied waves, the nominal wake fraction fluctuate up to 39% of the mean nominal wake fraction. The mean nominal wake fraction is higher than in calm water for all headings besides head sea waves. The maximum mean nominal wake fraction is found to occur in stern quartering sea waves, with a 16% higher mean nominal wake fraction than in calm water. It is also found that the transient bilge vortex and shadow from the skeg have a significant influence on the nominal wake field. Finally the study shows that the modified advance angle on the  $r/R = 0.7$  circle in the propeller plane varies 3.5 degrees more in port stern quartering than in calm water, increasing the risk of cavitation.

*Keywords:* Wake field, Wake field in waves, Nominal wake fraction, CFD, Oblique waves

---

## 1. Introduction

Traditionally, ship propellers have been designed to have optimum performance in calm water. This is mainly because ship building contracts are written with requirements for the speed-power performance in calm water. However, most ships only sail in calm water a very small fraction of the time. When a ship is sailing in waves, the flow around the ship changes significantly causing ship motions and added resistance.

Most experimental studies of ships sailing in waves have been conducted for head and to some extent following sea waves. This is because most towing tanks are not wide enough to allow the ship to sail with an angle to the wave maker, termed oblique waves, for long enough time to get a high quality measurement. However, a few studies have been conducted in oblique waves. One of the first experimental studies of added resistance in oblique waves is [Fujii and Takahashi \(1975\)](#) which studied the added resistance on the S175 container ship in various headings. More recently, an important research project is the SHOPERA project, where comprehensive experimental program of more than 1300 different model tests for three ship hulls of different geometry and hydrodynamic characteristics has been conducted by four maritime experimental research institutes ([Sprenger et al., 2017](#)). [Valanto and Hong \(2015\)](#) experimentally tested the added resistance of a confidential cruise ship in seven different headings identifying the  $45^\circ$  heading to give maximum added resistance. The study by [Sadat-Hosseini et al. \(2015\)](#) presented experiments, potential flow, and CFD computations for added resistance for variable headings and wave lengths for the KCS. They found that their applied potential-flow method captures the heave and pitch motions well, while surge, roll, and added resistance were not well predicted for most cases. Some of these results were also presented at the Tokyo 2015 CFD workshop ([Hino et al., 2020](#); [Stern et al., 2021](#)). However, when experimental studies in oblique waves are conducted, the ship models often need to be smaller than those used in the classical long towing tanks. This is generally resulting in higher uncertainties cf. [Chuang and Steen \(2013\)](#). In numerical studies, tank sizes and thereby model size is not an issue.

Several numerical studies of ships sailing in oblique waves have been published. [Shigunov et al. \(2018\)](#) summarizes the results of the SHOPERA international benchmark study of numerical methods for the prediction of time-average wave-induced forces and manoeuvres of ships in waves. The study illustrated the strengths and weaknesses of different numerical methods. [Gong et al. \(2020\)](#) numerically studied added resistance and seakeeping performance of trimarans in oblique waves. The results showed that the trends of the added resistance and motion amplitudes of the trimaran in waves are significantly affected by the wave steepness and wave incident angles, which are also different from those of traditional mono-hull ships. [Mikkelsen et al. \(2021\)](#) compared the motion responses and added resistance for the KCS ship in waves predicted by experiments, CFD and potential flow analyses. Various heading angles were studied, and in general the CFD results agreed well with the experiments.

Most published studies focused on the seakeeping, maneuvering and added resistance, when the ships are sailing in oblique waves. Very few studies focused on how the sailing in oblique waves influences the operation of the propeller, even though the propeller is a crucial

part of the ship. The starting point when considering the operation of the propeller is the wake field, i.e. the flow field in the propeller disk. In the present study only the nominal wake field is considered. The nominal wake field of a ship can be considered to effectively comprise three components: the potential wake, the frictional wake, and the wave-induced wake (Carlton, 2012). CFD simulations offer to include all three of these components. The wave-induced wake is due to the gravity waves generated by the ship and not related to the incident waves. The effective wake field is the nominal wake field including the hull-propeller interaction velocities. The total wake field is the effective wake field including the propeller induced velocities. Regener et al. (2018) showed that the nominal and effective wake fields are quite similar with the axial velocities being slightly higher in the effective wake field.

A few studies have investigated wake fields in waves. Longo et al. (2007) studied the nominal wake of the DTMB model 5415 ship in regular head sea waves using Particle Image Velocimetry (PIV). Wu et al. (2020) investigated the forces, ship motions, and wake field for the KCS model in head sea waves both with and without a propeller. They found that CFD results agreed well with the experiments. Kim et al. (2021) numerically and experimentally studied the propulsion coefficients of the KCS in regular waves with different headings. Their CFD predicted the stern quartering sea waves as the heading with maximum effective wake fraction. However, their experiments showed that the maximum effective wake fraction was present in following sea waves. The studies by Kim et al. (2021), Longo et al. (2007), and Wu et al. (2020) showed that wake field becomes transient, when the ship is sailing in waves. Transient wake fields are normally not considered in the propeller design phase, since a wake field in calm water is almost entirely steady-state. Two of the main objectives when designing a propeller are maximum efficiency and minimum cavitation. Cavitation can lead to vibration causing discomfort and increased wear. Furthermore, cavitation decreases the propeller thrust and can cause erosion of the blade material. When the wake field becomes transient in waves, it is interesting to investigate how sailing in waves influences the propeller efficiency, cavitation and the propeller-hull interaction. The effective wake fraction is studied by Sanada et al. (2018) and Kim et al. (2021), where added powering simulations and experiments of the KCS ship in multiple headings and wave lengths are conducted. Saettone et al. (2020) compared a fully-unsteady and a quasi-steady approach for the prediction of the propeller performance in waves. They found a good agreement between the approaches demonstrating that the less demanding quasi-steady approach can be used to compute the propeller performance in waves. Chuang and Steen (2013) experimentally and numerically studied the speed loss of a 8000DWT tanker in oblique waves. Even though converged speed cannot be achieved in every run, due to the limited length of the ocean basin, they found that maximum speed loss occurs when the wave length is equal to the ship

length. [Saettone et al. \(2021\)](#) experimentally studied the propulsive factors in following and head sea waves. They found that the effective wake fraction in head sea waves is lower than in calm water and that the effective wake fraction in following sea waves is higher than in calm water.

To the best of the authors' knowledge, no systematic study investigating the nominal wake field in multiple headings has been published. Therefore, the scope of this paper is to study how the nominal wake field is influenced by sailing in oblique waves.

The study is conducted using CFD with the KCS ship in regular waves with a steepness of  $1/60$ . The CFD model is validated with experimental results from the literature in calm water and in head sea waves. The transient nominal wake field distribution and nominal wake fraction is analyzed for five different headings.

## 2. Methodology

The present Unsteady Reynolds Averaged Navier-Stokes (URANS) CFD simulations are performed with the commercial CFD-code STAR-CCM+ v.2020.1 ([Siemens, 2020](#)). STAR-CCM+ discretizes the governing equations using an unstructured finite-volume method. The code is widely used in the marine industry and is well known for its capabilities within marine applications.

### 2.1. The studied ship

The studied ship is the 3,600 TEU Kriso Container Ship (KCS). The main particulars of the KCS can be seen in Table 1. The KCS is chosen since both experimental data and the hull geometry are publicly available. In order to study the effects of the wave heading on the wake field behind the ship at the position of the propeller, five wave headings as illustrated in Fig. 1 will be considered in this paper. The five studied cases and their encounter frequencies are seen in Fig. 2, together with the natural frequencies for heave/pitch and roll. The used propeller fixed coordinate system is seen in Fig. 3. The CFD model has previously been validated for calm water resistance calculations in both model and full scales ([Mikkelsen et al., 2019](#); [Mikkelsen and Walther, 2020](#)). The CFD setup used in the present study is based on the CFD setup used by [Mikkelsen et al. \(2021\)](#) for simulations of added resistance in oblique waves. The study by [Mikkelsen et al. \(2021\)](#) includes an extensive validation of the motions responses and added resistance. The wave length for all headings studied in Sec. 3.3 is equal to the ship length since these conditions are expected to have high motion responses, added resistance and speed loss ([Chuang and Steen, 2013](#)).

Name	Symbol	Value
Model scale		71.875
Length between perpendiculars	$L_{pp}$	3.2 m
Beam	$B$	0.448 m
Draft	$T$	0.1503 m
Displacement	$\Delta$	137.72 kg
Froude number	$Fn$	0.26
Speed	$U$	1.4567 m/s
Vertical Center of Gravity (from keel)	$KG$	0.199 m
Longitudinal radius of gyration	$k_{xx}$	$0.40 B$
Transverse radius of gyration	$k_{yy}$	$0.25 L_{pp}$
Natural heave/pitch period with constant speed	$T_{Z\theta,U}$	1.03 s
Natural roll period with constant speed	$T_{\phi,U}$	3.31 s
Propeller diameter	$D_P$	0.1099 m
Propeller hub diameter	$D_{hub}$	0.0198 m
Propeller RPM	$RPM$	$980.5 \text{ min}^{-1}$

Table 1: Main particulars.

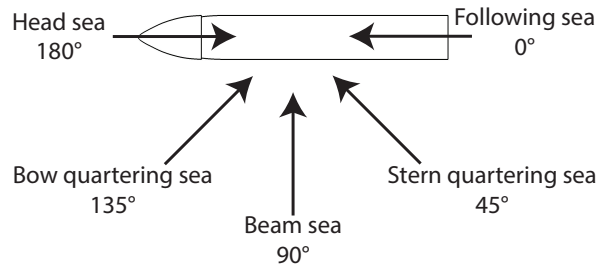


Figure 1: Studied wave headings.

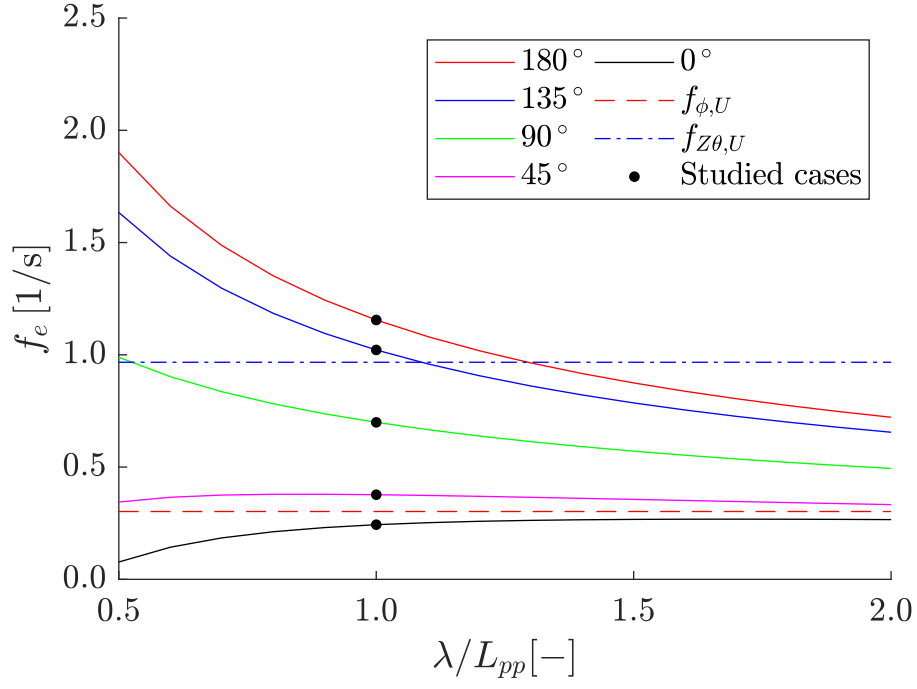


Figure 2: Encounter frequencies ( $f_e$ ) as function of wave heading and non-dimensional wave length ( $\lambda/L_{pp}$ ). Horizontal lines are the natural roll ( $f_{\phi,U}$ ) and heave/pitch ( $f_{Z\theta,U}$ ) frequencies when sailing with constant speed in calm water.

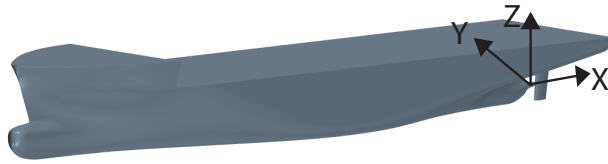


Figure 3: The coordinate system used in the present study is centered in the propeller plane in the center of hub.



## 2.2. Governing equations

The governing equations of an incompressible Newtonian fluid are the Navier-Stokes equations (Ferziger and Peric, 2002):

$$\frac{\partial u_j}{\partial x_j} = 0 \quad (1)$$

$$\rho \frac{\partial u_i}{\partial t} + \rho u_j \frac{\partial u_i}{\partial x_j} = -\frac{\partial p}{\partial x_i} + \frac{\partial}{\partial x_j} (2\mu S_{ij} - \rho \overline{u'_j u'_i}) + f_i \quad (2)$$

where  $u_i$  is the velocity vector,  $t$  is time,  $p$  is pressure,  $\mu$  is dynamic viscosity,  $S_{ij} = \frac{1}{2} \left( \frac{\partial u_i}{\partial x_j} + \frac{\partial u_j}{\partial x_i} \right)$  is the mean strain rate tensor,  $u'_i$  is the turbulent fluctuating part of the velocity, and  $f_i$  is body forces.

In order to close the problem the Reynolds stresses are modeled using a linear eddy viscosity model. The linear constitutive relationship (Wilcox, 1998) is:

$$-\rho \overline{u'_i u'_j} = 2\mu_t S_{ij} - \frac{2}{3} \rho k \delta_{ij} \quad (3)$$

where  $\mu_t$  is the turbulent viscosity,  $k$  is the turbulent kinetic energy, and  $\delta_{ij}$  is Kronecker's delta function.

In this study the turbulent viscosity is calculated using the realizable  $k$ - $\epsilon$  turbulence model (Shih et al., 1995; Siemens, 2020). The choice of turbulence model is discussed in Sec. 3.1.4. The  $k$ - $\epsilon$  model is a two equations model based on the turbulent kinetic energy  $k$  and the turbulent dissipation rate  $\epsilon$  (Wilcox, 1998) where:

$$\mu_t = \rho C_\mu \frac{k^2}{\epsilon} \quad (4)$$

where  $C_\mu$  is an empirical constant.

The free surface is resolved using the volume of fluid (VOF) method in STAR-CCM+ (Hirt and Nichols, 1981; Siemens, 2020). Hence, the volume fraction  $\alpha$  is assigned and evolves in time with the following transport equation:

$$\frac{\partial \alpha}{\partial t} + \frac{\partial}{\partial x_j} (\alpha u_j) = 0 \quad (5)$$

The transport equation is solved using the High-Resolution Interface Capturing scheme (Muzafarrija and Perić, 1997). The effective fluid properties are weighted using the volume fraction:

$$\rho = \alpha \rho_w + (1 - \alpha) \rho_a \quad (6)$$

$$\mu = \alpha\mu_w + (1 - \alpha)\mu_a \quad (7)$$

where  $\rho_w$  is the density of the water phase,  $\rho_a$  is the density of the air phase and  $\mu_w$  and  $\mu_a$  are the corresponding dynamic viscosities. For all simulations, the schemes for the convective and diffusive terms are 2<sup>nd</sup>-order. The solver for the temporal discretization is a second-order implicit scheme. A constant time step is chosen keeping the convective Courant number is kept below 0.5 on the free surface. For each time step, eight inner iterations are used to ensure convergence of the non-linear equations.

### 2.3. Computational Domain and Wave Generation

The shape of the CFD domain is a rectangular box. The top of the domain is set to a pressure boundary in order to allow the air flow to evolve freely. With a pressure outlet, a Dirichlet boundary condition is used to fix the pressure to zero gauge pressure. Furthermore, Neumann boundary conditions are used to prescribe a zero normal gradient for the velocity, and volume fraction. The five sides of the domain are velocity inlets, where Dirichlet boundary conditions are used to prescribe the velocity, and volume fraction on the inlet to be the same as the incident wave. When all vertical sides are velocity inlets with no pressure outlets, the heading of the ship can be allowed to change during a run in future manoeuvring simulations.

The computational domain is divided into two parts, namely the forcing zone (or relaxation zone) and the solution zone. The inner volume, where no forcing is applied, is denoted the solution zone. See Fig. 4 for an illustration. The forcing zone at the outer layer of the computational domain is used to generate the incident regular waves. A smooth-transition function in the form of  $\cos^2$  is applied within the forcing zone, so that the flow solution is enforced to be the same as the prescribed incident waves at the outer boundaries (the 4 vertical boundaries), while the forcing becomes zero at the end of the forcing zone, i.e. close to the boundary of the solution zone. The forcing zone also acts as wave absorbing zone due to the relaxation of the solution towards the targeted incident wave solution at the outer boundaries. In this paper, the Stokes fifth-order waves are used as input waves, which are available from the built-in wave module in STAR-CCM+. The steepness of the incident wave is 1/60 corresponding to the wave steepness in the experimental study of [Sadat-Hosseini et al. \(2015\)](#), which was used in the validation study by [Mikkelsen et al. \(2021\)](#). The width of the forcing zone is equal to two times the wavelength of the incident wave. The influence of the forcing zone width has been studied in detail (not shown). It is found that a forcing zone width of two incident wavelengths is a good compromise between numerical diffusion, wave reflection and computational cost. A forcing zone width of only

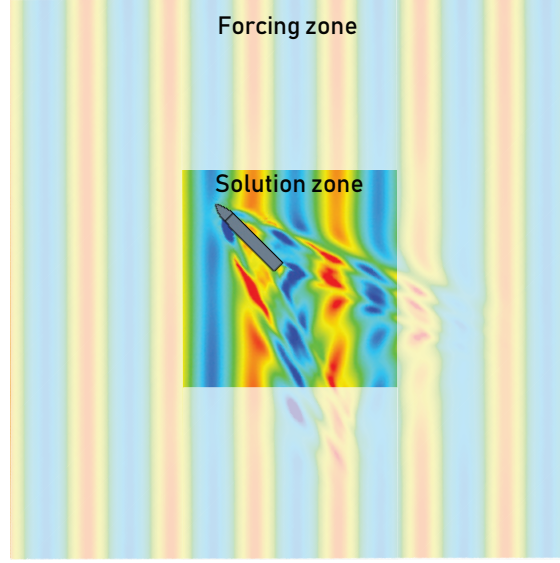


Figure 4: Wave elevation for bow quartering sea waves and  $\lambda/L_{pp} = 1$ .

one incident wavelength caused significant reflection (not shown). The size of the solution zone is  $3L_{pp} \times 3L_{pp}$ . This size is found large enough not to influence the added resistance, seakeeping responses and wake field.

#### 2.4. Mesh

The mesh consists of a background region and an overset region. The size of the overset region is determined, so there is always minimum 5 cells from the surface of the ship to the overset boundary. This is recommended by [Siemens \(2020\)](#), in order to ensure that the overset solver accurately can exchange information between the background region and the overset region. An example of the overset region for the stern quartering sea waves case can be seen in Fig. 5. The volume mesh consists of hexahedrons in an unstructured grid. The mesh is generated using the trimmer-mesh function in STAR-CCM+ and is aligned with the wave direction. The boundary layer mesh, also called the prism layer mesh, is used on the hull surface in order to ensure accurate estimation of the wall shear stress within the wall function approximation. A sensitivity study of using wall-function compared to resolving the boundary layer is presented in Sec. 3.1.3. Three prism layers are used on the ship hull. Each prism layer is 50% thicker than the previous layer, giving an expansion ratio of 1.5. The quality of the prism layers are inspected to ensure high quality and good transition from the outer prism layer to the core mesh. The wall  $y^+$ -values on the hull are mostly in the range of 30–100. The mesh is refined in the important zones including the free surface in order to resolve the incident wave and the generated Kelvin wave. Furthermore, the mesh

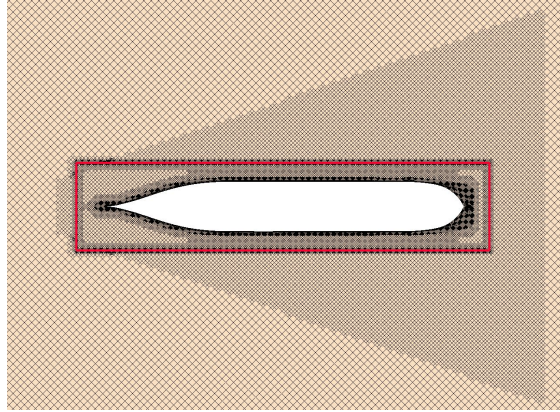


Figure 5: Mesh on the free surface seen from the top for stern quartering sea waves. The overset boundary is shown in red. Volumetric refinement is seen to resolve the generated Kelvin waves.

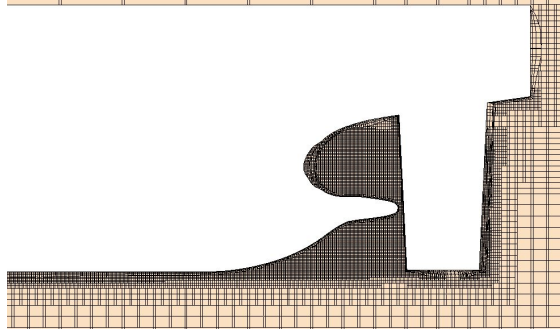


Figure 6: Mesh near aft of the ship.

is refined near the ship. The mesh near the aft can be seen in Fig. 6. The built-in overset adaptive mesh refinement module in STAR-CCM+ is used to ensure equal cell sizes in the overlapping region between the background and overset meshes. The mesh including the ship is moving with constant horizontal speed.

### 2.5. Motions

The ship is free in  $z$ -translation (heave),  $y$ -rotation (pitch), and  $x$ -rotation (roll), and fixed in  $x$ -translation (surge),  $y$ -translation (sway), and  $z$ -rotation (yaw). In the CFD model, the heave, pitch, and roll motions of the vessel are solved using the Dynamic Fluid Body Interaction (DFBI) Multi Body solver in STAR-CCM+ cf. (Siemens, 2020) and is applied as a rigid translation and rotation of the overset region. The DFBI Multi Body solver is chosen for its stability and accuracy. Sway is constrained accurately by the motion solver in STAR-CCM+. However, the DFBI solver in STAR-CCM+ version 2020.1 is found to produce an unacceptable drift in the constrained yaw. Besides the drift, constraining the

yaw motion by the built-in motion module in STAR-CCM+ makes the roll response non-physical. Therefore, the yaw and surge motions are constrained using implementations by the authors. The surge is constrained by applying a concentrated  $x$ -force each time step in the center of mass equal to the integrated resistance with opposite sign. With this implementation, the speed of the ship never deviates more than 0.1 % from the target ship speed. The yaw motion is constrained by applying a concentrated  $z$ -moment and a torsional spring around the  $z$ -axis of the ship in the center of mass. The magnitude of the applied concentrated  $z$ -moment is equal to the integrated  $z$ -moment of the ship with opposite sign. For the considered KCS ship in model scale, the torsional spring constant is set to 20 kNm/deg in order to ensure a small yaw angle and a natural yaw frequency far from the natural frequencies of the motions and incident waves. The magnitude of the concentrated  $z$ -moment is approximately 50 times larger than the  $z$ -moment from the torsional spring. With this implementation, the simulated yaw angle never exceeds 0.01 deg and it is found not to influence the other motions.

## 2.6. Grid convergence index

For the verification study of the CFD model, the discretization error is estimated using the Grid Convergence Index (GCI) method (Celik et al., 2008) which is based on Richardson extrapolation, cf. (Richardson, 1910; Richardson and Gaunt, 1927). The apparent order ( $p$ ) is calculated by:

$$p = \frac{1}{\ln(r_{21})} \left| \ln \left| \frac{\epsilon_{32}}{\epsilon_{21}} \right| + q(p) \right| \quad (8)$$

$$q(p) = \left( \frac{r_{21}^p - s}{r_{32}^p - s} \right) \quad (9)$$

$$s = \text{sgn}(\epsilon_{32}/\epsilon_{21}) \quad (10)$$

where  $r_{21}$  and  $r_{32}$  denote the refinement ratios,  $\epsilon_{32} = \phi_3 - \phi_2$ ,  $\epsilon_{21} = \phi_2 - \phi_1$ ,  $s$  is a sign indicator, and  $\phi_k$  denotes the solution on the  $k$ -th mesh.  $q(p) = 0$  for  $r_{21} = r_{32}$ . The extrapolated asymptotic value is calculated as:

$$\phi_{ext}^{21} = \frac{r_{21}^p \phi_1 - \phi_2}{r_{21}^p - 1} \quad (11)$$

Different error estimates can now be calculated. The approximate relative error is:

$$e_a^{21} = \left| \frac{\phi_1 - \phi_2}{\phi_1} \right| \quad (12)$$

$$e_a^{31} = \left| \frac{\phi_1 - \phi_3}{\phi_1} \right| \quad (13)$$

The extrapolated relative error is:

$$e_{ext}^{21} = \left| \frac{\phi_{ext}^{12} - \phi_1}{\phi_{ext}^{12}} \right| \quad (14)$$

The GCI for the fine and medium mesh is calculated as follows using the safety factor of 1.25 recommended by [Roache \(1998\)](#):

$$GCI_{Fine}^{21} = \frac{1.25e_a^{21}}{r_{21}^p - 1} \quad (15)$$

Eq. (15) is extended to the GCI for the medium and coarse mesh:

$$GCI_{Medium}^{21} = \frac{1.25e_a^{21}r_{21}^p}{r_{21}^p - 1} \quad (16)$$

$$GCI_{Coarse}^{31} = \frac{1.25e_a^{31}r_{31}^p}{r_{31}^p - 1} \quad (17)$$

The GCI values are used as an estimate of discretization errors, since they are a measure of the relative discrepancy between the computed value and the asymptotic numerical value. Please note that this method does not identify the exact discretization error, but just an estimate ([Roache, 1998](#)).

## 2.7. Post-processing

The nominal wake fraction presented in this study is the nominal Taylor wake fraction ([Carlton, 2012](#)). In order to avoid confusion between the spatially and temporally averaged nominal wake fraction, the spatially averaged wake fraction which is calculated using an area weighted averaged on the propeller disc will be described as the *nominal wake fraction* in this paper. The temporally averaged nominal wave fraction will be described as *mean nominal wake fraction*. The nominal wake fraction ( $w_T$ ) on the propeller disc is defined as ([Carlton, 2012](#)):

$$w_T = \frac{\int_{r_h}^R r \int_0^{2\pi} \left(1 - \frac{u_a(\phi, r)}{U_s}\right) d\phi dr}{\pi (R^2 - r_h^2)} \quad (18)$$

where  $U_s$  is the ship speed,  $u_a(\phi, r)$  is the axial velocity,  $R$  is the propeller radius, and  $r_h$  is the hub radius.

The mean nominal wake fraction over one encounter period is computed as:

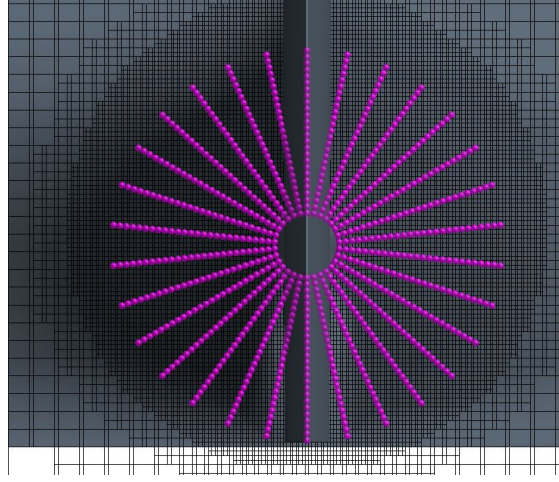


Figure 7: Purple dots are data extraction points located in propeller disc seen from aft. The black lines shows the mesh in the propeller plane.

$$\bar{w}_T = \frac{1}{T_e} \int_0^{T_e} w_T dt \quad (19)$$

The results presented in Sec. 3.2 are in an earth-fixed coordinate system since the experimental nominal wake field used in the validation are presented in an earth-fixed coordinate system. However, results in Sec. 3.1 and 3.3 are presented in a propeller-fixed coordinate system, since this is the flow the propeller will encounter. Both coordinate systems are defined in the CFD simulations and the results are extracted directly in these coordinate systems. The difference between these two coordinate systems is that propeller-fixed coordinate system is influenced by the roll, pitch and heave motions.

In section Sec. 3.3, the calm water velocity field is subtracted from the velocity field in waves. This subtraction is conducted in MATLAB. In order to export the nominal wake fields to MATLAB, the nominal wake field data in the propeller disc is exported on a polar  $30 \times 30$  grid. However only 780 out of the 900 points are used since the remaining points are inside the hub. The 780 points in which the data is exported can be seen in Fig. 7.

In order to relate the wake fields to the operation and performance of the propeller, the advance angle ( $\beta$ ) can be calculated in each location on the propeller. The advance angle ( $\beta$ ) as function of angular position ( $\phi$ ) and time along the circle  $r/R = 0.7$  on the propeller disc is defined as (Carlton, 2012):

$$\beta(\phi, t) = \tan^{-1} \left( \frac{u_a}{0.7D \pi n} \right) \quad (20)$$



where  $n$  is the propeller rotational speed in [1/s] which is set to 16.341/s in the present model scale (FORCE, 2013).

By including the effect of the tangential velocity component ( $u_t$ ), a modified angle ( $\beta_t$ ) as function of angular position and time along the circle  $r/R = 0.7$  on the propeller disc for a right handed propeller is defined as:

$$\beta_t(\phi, t) = \tan^{-1} \left( \frac{u_a}{0.7\pi n D - u_t} \right) \quad (21)$$

The difference between  $\beta$  and  $\beta_t$  is lower than 2 degrees for the studied cases.

As shown by Regener et al. (2018), the nominal and effective wake fields are quite similar. Normally, the effective wake field has a slightly larger axial velocity than the nominal wake field due to hull-propeller interaction. Since the specific propeller including pitch distribution is not known, conclusion will only be made on the difference in modified advance angle and not absolute values.

### 3. Results

The results are presented in three sections. Firstly, the CFD results are verified by conducting mesh and time step convergence studies followed by a sensitivity study of resolving the boundary layer and choice of turbulence model. Secondly, the present CFD setup is validated by comparing the results with experimental results from the literature in calm water (Gaggero et al., 2017) and in head waves (Wu et al., 2020). Lastly, the CFD results of the nominal wake fields in oblique waves are studied.

#### 3.1. Verification

In the verification study, the spatial and temporal discretization errors of the mean nominal wake fraction defined in Eq. (19) and first-harmonic amplitude of the nominal wake fraction is estimated based on the GCI method presented in Sec. 2.6. The verification studies are conducted in bow quartering sea waves. This is considered one of the most challenging test cases for the CFD solver. This test case has very large motions and added resistance partly due to the fact that the encounter frequency is close to the natural pitch and heave frequency as seen in Fig. 2.

##### 3.1.1. Mesh convergence study

In order to estimate the spatial discretization errors, simulations are conducted using three meshes and a constant time step corresponding to 750 time steps per incident wave period. With this time step size, the Courant number on the free surface for all meshes



Table 2: Grid convergence index (GCI) values for the estimated spatial discretization error for the mean wake fraction ( $\bar{w}_T$ ) and first-harmonic amplitude of the nominal wake fraction ( $w_T$ ). The simulation time is based on 80 cores using Intel Xeon Gold 6242R CPUs.

	Number of cells	Simulation time	GCI $\bar{w}_T$	GCI Amp. of $w_T$
Mesh 1	$15.6 \times 10^6$	163 hours	1.1 %	0.1 %
Mesh 2	$7.8 \times 10^6$	67 hours	2.1 %	1.0 %
Mesh 3	$3.1 \times 10^6$	40 hours	1.6 %	11.2 %

is well below the value of 0.5 as suggested by [Siemens \(2020\)](#). The refinement ratios are estimated by the cubic root of the total cell count for each mesh. The meshes are varied by changing the mesh base size, which affects the cell size everywhere in the mesh besides the prism layer mesh. The aspect ratio between the horizontal and vertical grid spacing in the free surface refinement zone for all meshes is constant and equal to eight. The results of the mesh convergence study are seen in Table 2. Both Mesh 1 and Mesh 2 show acceptable spatial discretization errors. Mesh 2 has 68 cells per wavelength and 9 cells per wave height in the free surface refinement zone. This is slightly fewer cells than what is recommended by [Siemens \(2020\)](#). However, Mesh 1 has 90 cells per wavelength and 12 cells per wave height and the influence on the results is less than 1 %, as seen in Table 2. Mesh 1 has approximately double as many cells as Mesh 2. Because of this, it is decided to use Mesh 2 settings for all further simulations, since it is considered the best compromise between spatial discretization errors and computational cost.

### 3.1.2. Time step convergence study

The temporal discretization errors are estimated based on three simulations with varying time step sizes using the settings from Mesh 2 from the previous subsection. It is decided to non-dimensionalize the time step with the incident wave period and not the encounter period, since the incident wave period is independent of wave heading. The encounter period for head sea waves is only 13 % smaller than for the bow quartering sea waves. This is considered small enough not to influence the sensitivity of the time step. The encounter periods for the beam, stern quartering, and following sea waves cases are larger than for the bow quartering sea waves case resulting in more time steps per encounter period, when using the same time step. Furthermore, the test case in the verification study has an encounter frequency, which is close to the natural heave and pitch frequency. This causes complex flow phenomena and strong variation in time. The sensitivity of the time step is considered

Table 3: Grid convergence index (CGI) values for the estimated temporal discretization error for the mean wake fraction ( $\bar{w}_T$ ) and first-harmonic amplitude of the nominal wake fraction ( $w_T$ ). The simulation time is based on 80 cores using Intel Xeon Gold 6242R CPUs.

Time steps per wave period	Simulation time	GCI $\bar{w}_T$	GCI Amp. of $w_T$
1000	98 hours	0.1 %	0.8 %
750	67 hours	0.1 %	1.3 %
500	48 hours	0.2 %	9.2 %

higher at this resonance test case than a non-resonance test case. The results of the time step convergence study are shown in Table 3. Three different temporal discretizations are considered, including 500, 750 and 1000 time steps per incident wave period. The reason why the estimated temporal discretization errors for  $\bar{w}_T$  are very small is because the variation in  $\bar{w}_T$  for the three simulations is less than 0.1%. The temporal discretization errors for both 750 and 1000 time steps per incident wave period are acceptable. For all further simulations, 750 time steps per incident wave period will be used, since the computational cost is lower than using 1000 time steps per incident wave period.

### 3.1.3. Influence of resolving the boundary layer

A comparison of simulations using wall functions and resolved boundary layer are conducted in order to study the influence of resolving the boundary layer. The simulation using wall functions has three prism layers resulting in  $30 < y^+ < 100$  on the hull. The simulation where the boundary layer is resolved has 14 prism layers resulting in  $y^+ < 1$  on the hull. The difference in the mean nominal wake fraction between the simulations is less than 1.2 % (not shown). Since resolving the boundary layer requires an approximately 30 % increase in computational cost, without notably improving the accuracy, all simulations will be conducted using wall functions.

### 3.1.4. Influence of turbulence model

A sensitivity study of the choice of turbulence model is conducted. A comparison of the two simulations using realizable  $k - \epsilon$  and  $k - \omega$  SST (Menter, 1993) turbulence models show a difference in mean nominal wake fraction of less than 2.1 % (not shown). This difference shows that the sensitivity of the choice of turbulence model is limited. All future simulations will be conducted using the realizable  $k - \epsilon$  turbulence model, since this is the model used in the previous validations (Mikkelsen and Walther, 2020) and (Mikkelsen et al., 2021).

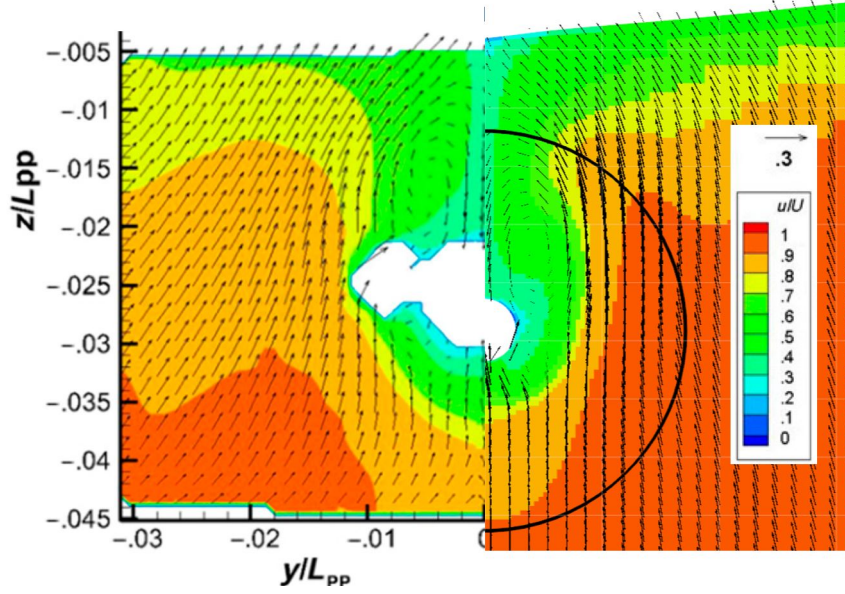


Figure 8: Comparison of the nominal wave field in calm water. Left: EFD by Wu et al. (2020). Right: Present CFD.

### 3.2. Validation

In this section the CFD setup will be validated for predicting the nominal wake field in calm water followed by a validation in regular head sea waves. The experimental results are from previously published papers by Wu et al. (2020) and Gaggero et al. (2017).

#### 3.2.1. Calm water

A comparison of the nominal wave field in calm water predicted by Experimental Fluid Dynamics (EFD) by Wu et al. (2020) and the present CFD model can be seen in Fig. 8. The agreement between EFD and CFD is good and similar to the agreement by the EFD and CFD by Wu et al. (2020) (not shown). However, there is a small difference in the vertical position of the propeller, which is also seen in the comparisons between EFD and CFD by Wu et al. (2020) (not shown). This is likely due to a small difference in the obtained steady sinkage and trim of the ship. The EFD data contains a larger white area. This white area is reported by the authors to be related to laser reflection issues. The missing data in this area makes it impossible to calculate a nominal wake fraction for the EFD data by Wu et al. (2020). However, experiments by Gaggero et al. (2017) for the same ship includes nominal wake fraction and data for the full propeller disc. The comparison of the nominal wake fraction is seen in Table 4. The wake fraction coefficient predicted by the present CFD is only 2.5 % smaller than in EFD, which is considered acceptable.

Table 4: Comparison of nominal wave fraction coefficient in calm water.

	$\bar{w}_T$
EFD by <a href="#">Gaggero et al. (2017)</a>	0.281
Present CFD	0.274
Discrepancy	-2.5 %

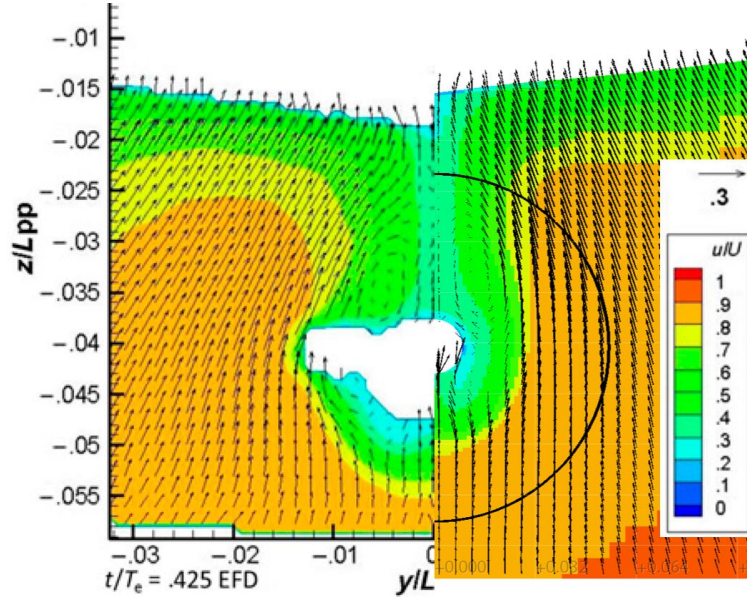


Figure 9: Comparison of the nominal wake field in head sea waves in an earth fixed coordinate system.  $\lambda/L_{PP} = 1.15$  at  $t/T_e = .425$ . Left: EFD by [Wu et al. \(2020\)](#). Right: Present CFD.

### 3.2.2. Head sea waves

Since no experimental data of the nominal wake field in oblique waves is available in the literature, validation of the nominal wake field can only be conducted in head sea waves. The EFD data is from the experiments by [Wu et al. \(2020\)](#). A comparison of the nominal wave field in head sea waves for the  $\lambda/L_{PP} = 1.15$  wave at  $t/T_e = .425$  can be seen in Fig. 9. When  $t/T_e = 0.0$  the incident wave crest is at the FP.

This comparison is presented in an earth fixed coordinate system, since this is how the EFD results are provided. It is seen that the propeller and hull in the CFD results is located higher than in the EFD. This offset of phase-lag is discussed by [Wu et al. \(2020\)](#), when they compare they CFD and EFD. They trace the offset back to the uncertainty of the experiments due to challenges measuring the distance between the wave probe and the ship. Furthermore, they documented that the wave amplitude and phase varied slightly during a run. To correct for this, the present CFD results in the comparison in Fig. 10 will be moved



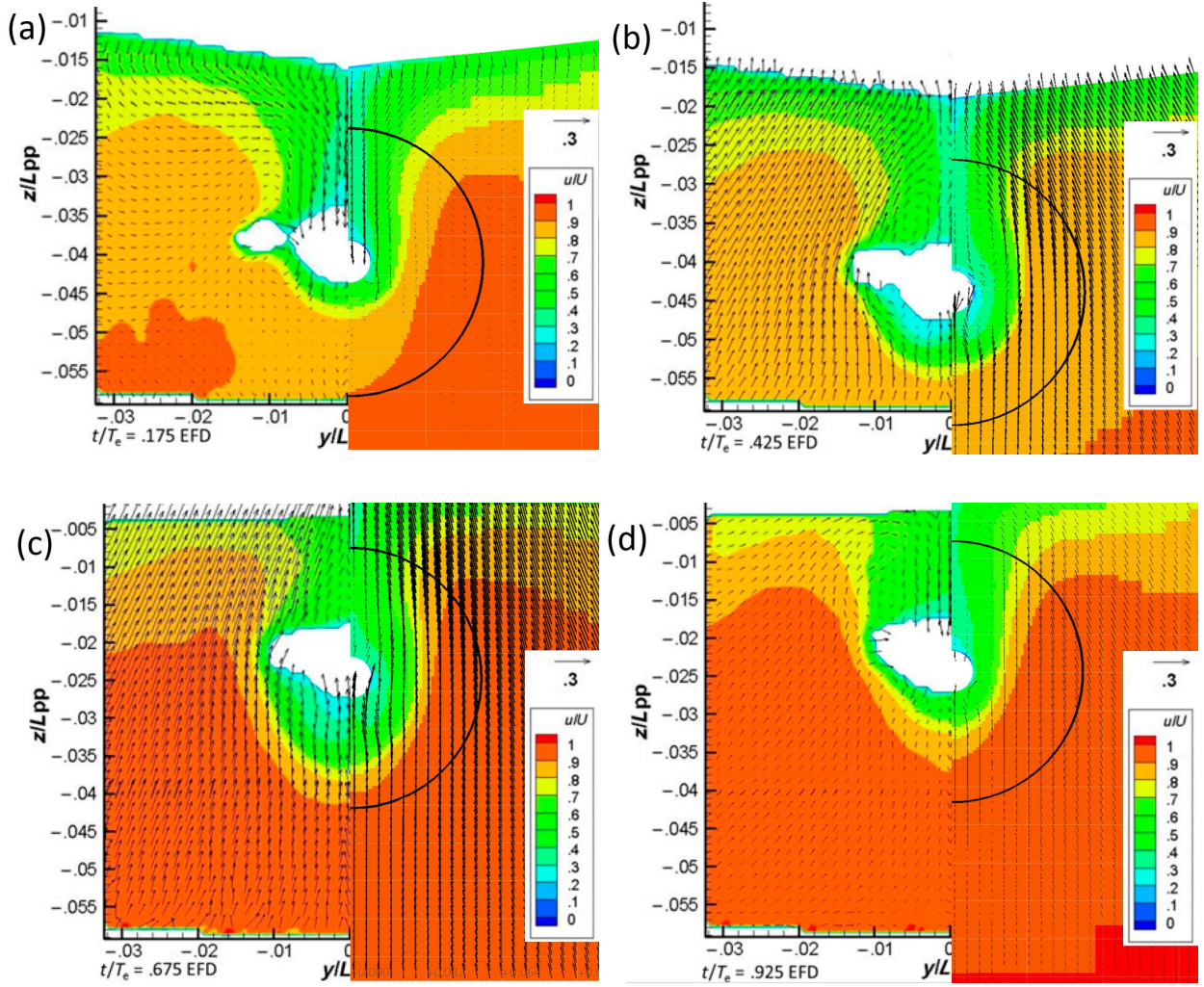


Figure 10: Comparison of the nominal wave field in head sea waves in an earth fixed coordinate system for four different times.  $\lambda/L_{PP} = 1.15$ . Left: EFD by [Wu et al. \(2020\)](#). Right: Present CFD. The CFD results have been shifted vertically so the location of the hull is the same in CFD and EFD. (a)  $t/T_e = .175$ ; (b)  $t/T_e = .425$ ; (c)  $t/T_e = .675$ ; (d)  $t/T_e = .925$ . Black circle is propeller radius.

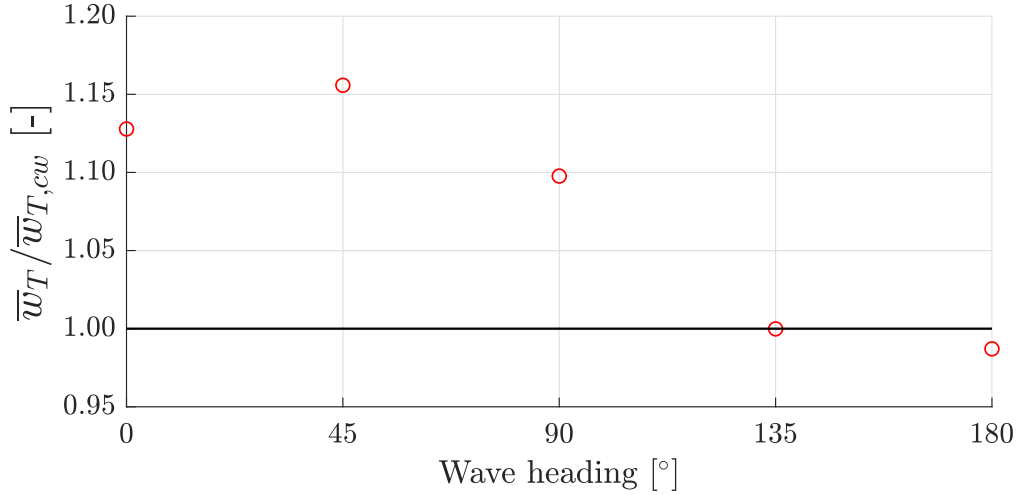


Figure 11: Mean nominal wake fraction ( $\bar{w}_T$ ) relative to mean nominal wake fraction in calm water ( $\bar{w}_{T,cw}$ ) as function of wave heading. Here  $\bar{w}_{T,cw} = 0.274$ .

vertically so the ship and propeller location match the location in the experiments. The comparison of the wake fields at four different times illustrated in Fig. 10 shows very good agreement, both for the axial and in-plane velocities.

The CFD setup is now verified and validated for accurately predicting the nominal wake field in head sea waves. Furthermore, the same CFD setup for the same ship model has been verified and validated for predicting the added resistance and motion responses in oblique waves by Mikkelsen et al. (2021). Therefore, it is considered reasonable to use the CFD setup to study the nominal wake field in oblique waves.

### 3.3. Influence of wave heading

All results in this section are presented in a propeller fixed coordinate system, since this is the velocity field the propeller will experience.

#### 3.3.1. Mean nominal wake fraction

The mean nominal wake fraction are calculated using Eq. (19) over four encounter periods to get an accurate mean nominal wake fraction. These mean nominal wake fractions for each wave headings are shown in Fig. 11. The only case with a mean nominal wake fraction lower than in calm water is the head sea waves case. Therefore, the mean axial velocity in the propeller disc will be higher in head sea waves than in calm water. The mean nominal wake fraction in bow quartering sea waves is very similar to the mean nominal wake fraction in calm water. The maximum mean nominal wake fraction for the studied cases is found in stern quartering sea waves, which 16 % higher than in calm water. The mean nominal wake

fraction in following sea waves is 13 % higher than in calm water. The experimental study in head and following sea waves by [Saettone et al. \(2021\)](#) found that effective wake fraction in head waves is lower than in calm water and that the effective wake fraction in following sea waves is larger in calm water. Furthermore, [Sanada et al. \(2018\)](#) and [Kim et al. \(2021\)](#) find that the highest effective wake fraction for the studied case is in stern quartering sea waves. This all agrees well with the present results for the nominal wake fraction. As seen in Fig. 2, the encounter frequency of stern quartering case is close to the natural roll frequency leading to significant roll motions. In order to study if the high nominal wake fraction in the stern quartering sea waves is mainly caused by large roll motions, one simulation where roll is fixed and one simulation where all motions are fixed in stern quartering sea waves are conducted. The mean nominal wake fractions for both of these simulations are 0.3106, which is only 1.9 % lower than for simulation which is free to heave, pitch and roll. Furthermore, the mean nominal wake fraction without motions is still larger than the nominal wake fraction for any of the other studied headings. Therefore, it can be concluded that the primary reason why the mean nominal wake fraction is largest at the stern quartering is not due to large motions responses. However, the dynamic part of the nominal wake field is dominated by the incident and diffracted wave effect including the bilge vortex and shadow from the skeg.

### 3.3.2. Nominal wake field distribution

To get an insight into the nominal wake field distribution, the time-averaged nominal wake field distributions for the different headings are calculated. These are shown in Fig. 12. The time-averaged nominal wake field distributions for the different headings are only slightly different. In order to compare the difference between them in more details, the calm water nominal wake field is subtracted from each of the time-averaged nominal wake field distributions in waves. The results of this subtraction are shown in Fig. 13. After the subtraction, it is easier to see the difference between different headings. Furthermore, it can be seen which areas of the propeller disc have a higher or lower average velocity. There is a general tendency of higher average axial velocities on the two sides of the propeller hub. However, above and especially below the propeller hub, lower average axial velocities are observed in general. This is also the case when the roll, pitch and heave motions are fixed. The only heading with a highly asymmetry time-averaged wake field distribution is the stern quartering sea waves seen in Fig. 13d. The asymmetry in the time-averaged nominal wake field distribution for the stern quartering sea waves case is a result of the asymmetry in the shadow from the skeg and difference in strength of the port side and starboard side bilge vortex.

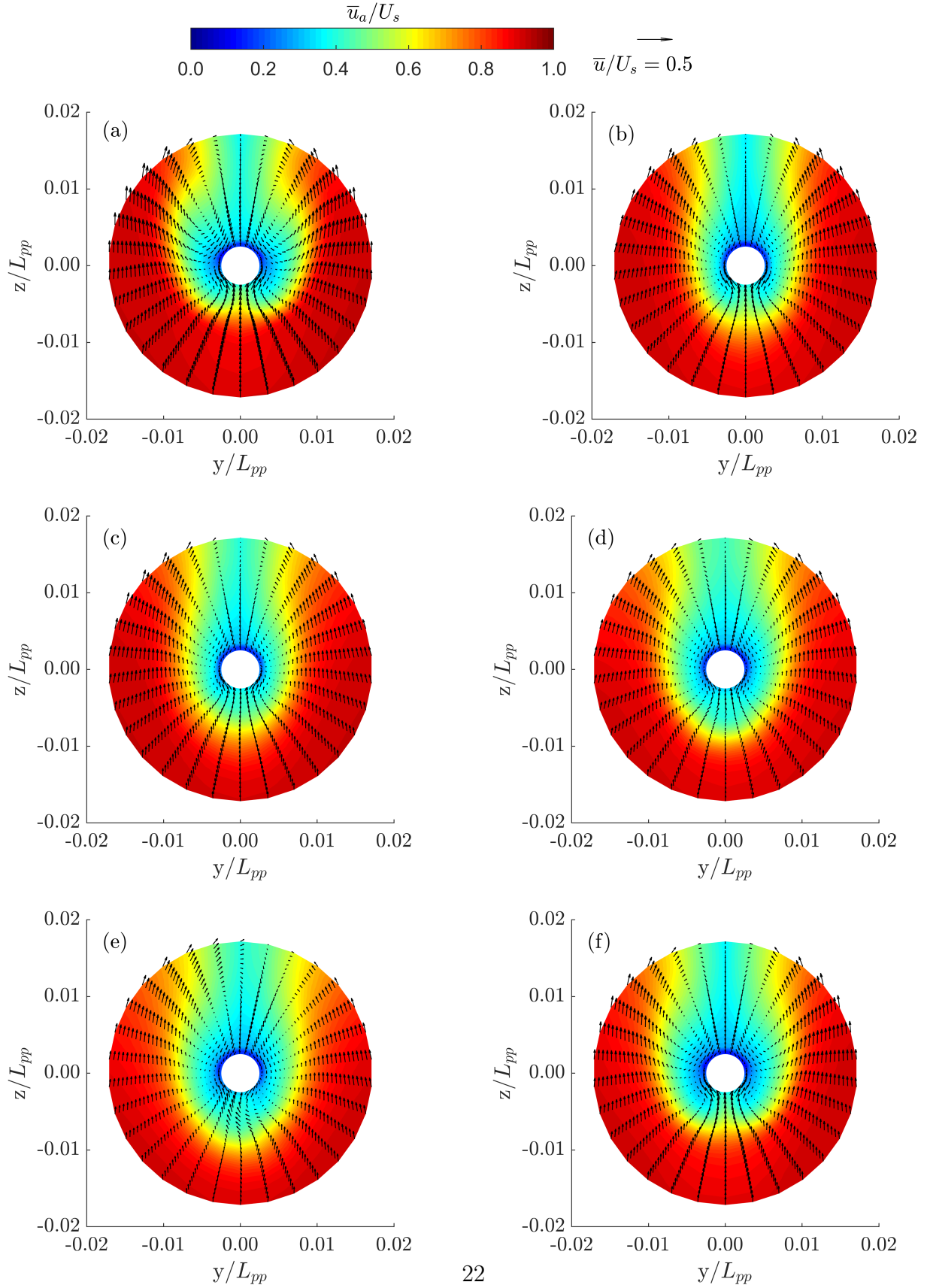


Figure 12: Time-averaged nominal wake fields for calm water and five wave headings. The arrows are the in-plane velocities.  $\bar{u}$  is the time averaged velocity,  $\bar{u}_a$  is the time averaged axial velocity, and  $U_S$  is the ship speed. (a) Calm water; (b) Head sea waves; (c) Bow quartering sea waves; (d) Beam sea waves; (e) Stern quartering sea waves; (f) Following sea waves.



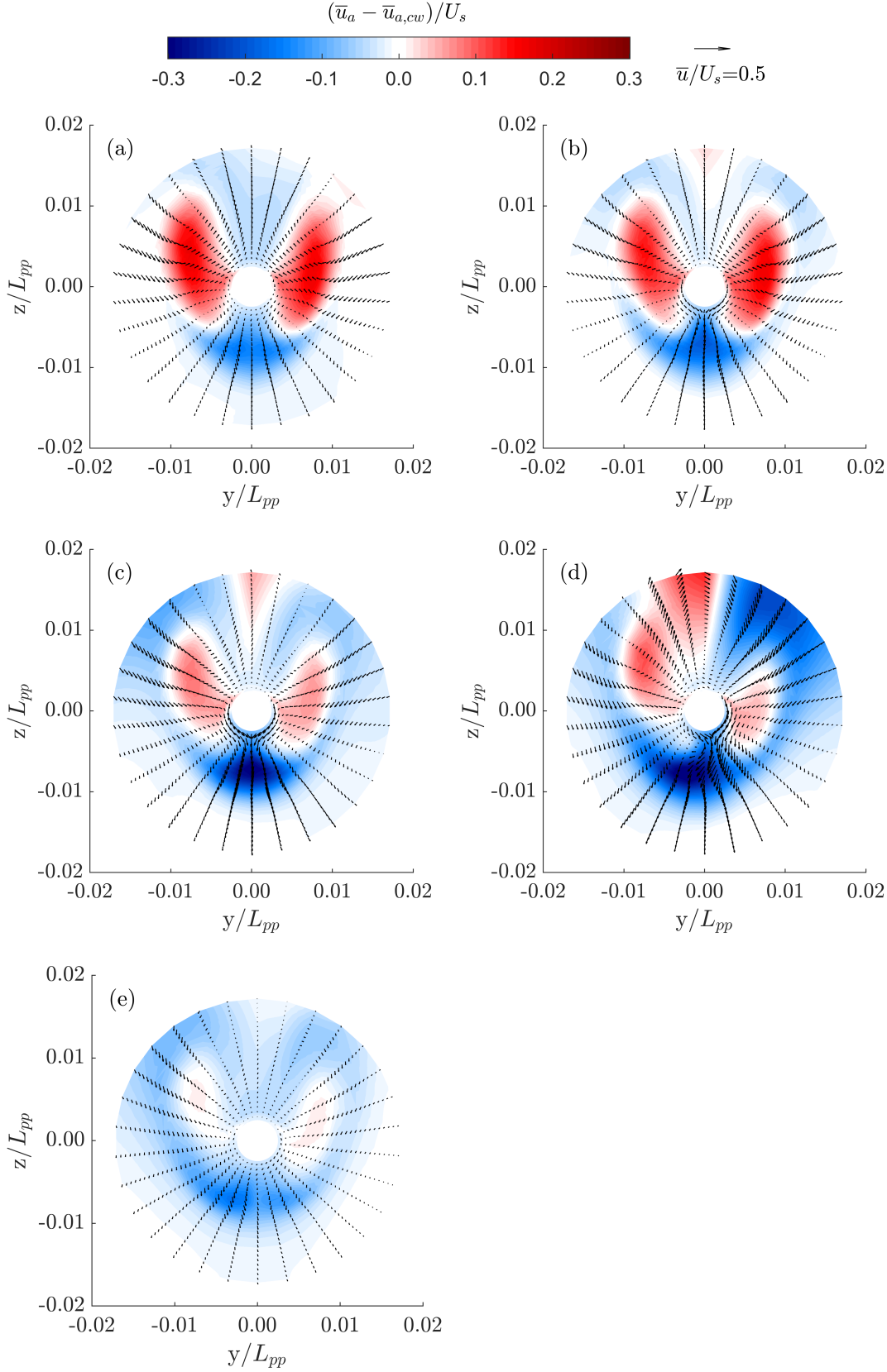


Figure 13: Difference in time-averaged nominal wake fields in waves relative to calm water. Positive value means that the time-averaged axial velocity in this area is larger than in calm water. Arrows show the difference in the in-plane velocities relative to calm water.  $\bar{u}$  is the time averaged velocity,  $\bar{u}_a$  is the time averaged axial velocity,  $\bar{u}_{a,cw}$  is the time averaged axial velocity in calm water and  $U_S$  is the ship speed. (a) Head sea waves; (b) Bow quartering sea waves; (c) Beam sea waves; (d) Stern quartering sea waves; (e) Following sea waves.

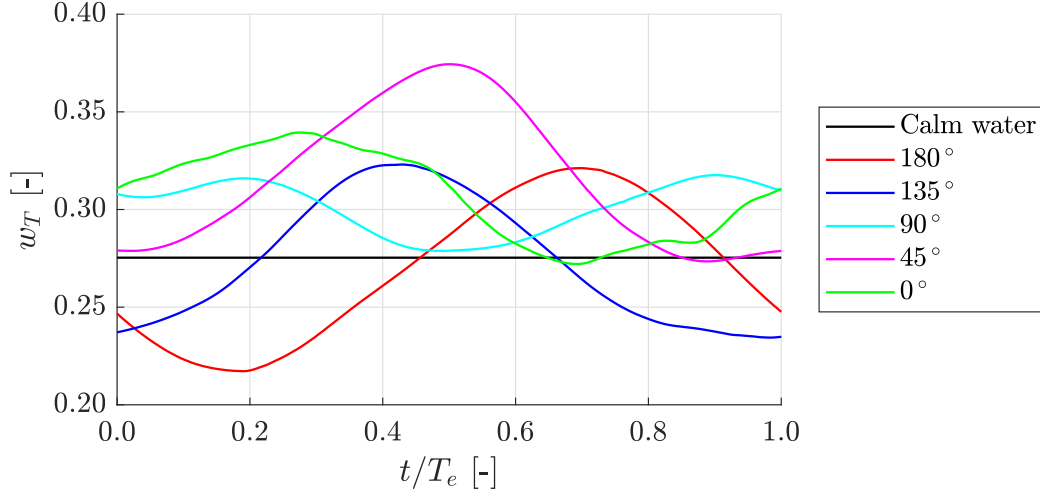


Figure 14: Nominal wake fraction ( $w_T$ ) over one encounter period  $T_e$  for different headings.

### 3.3.3. Temporal variation of the nominal wake fraction

The nominal wake fraction can be calculated at each time step using Eq. (18). The nominal wake fraction over one encounter period for the five different headings are compared in Fig. 14. When  $t/T_e = 0.0$  the incident wave crest is at the forward perpendicular. A phase shift due to the heading is observed. The phase shift between the head sea waves and following sea is approximately  $0.5 T_e$ . This is expected since in head sea waves at  $t/T_e = 0.0$  the incident wave crest is traveling from the forward perpendicular toward midship and in following sea the wave crest is traveling from the forward perpendicular and away in front of the ship. The nominal wake fraction fluctuates significantly over time. The fluctuations in nominal wake fraction over one encounter period is between 0.04–0.11 corresponding to 13–39 % of the mean nominal wake fraction. The largest fluctuations of 39 % of the mean nominal wake fraction are seen in head sea waves, where the large pitch motions contributes significantly to the variation in axial velocity. In bow quartering and stern quartering the fluctuations are 32 % of the mean nominal wake fraction.

### 3.3.4. Transient wake fields

Animations of the transient nominal wake fields for the five different headings are presented in Fig. 15. Furthermore, animations of the transient nominal wake fields in waves relative to calm water can be seen in Fig. 16. It is seen that the nominal wake field is strongly transient compared to the almost steady-state wake field in calm water shown in Fig. 8. The variations over time are significant for both the axial velocity and in-plane velocities. The variations are partly due to the ship motions, diffracted incident waves and

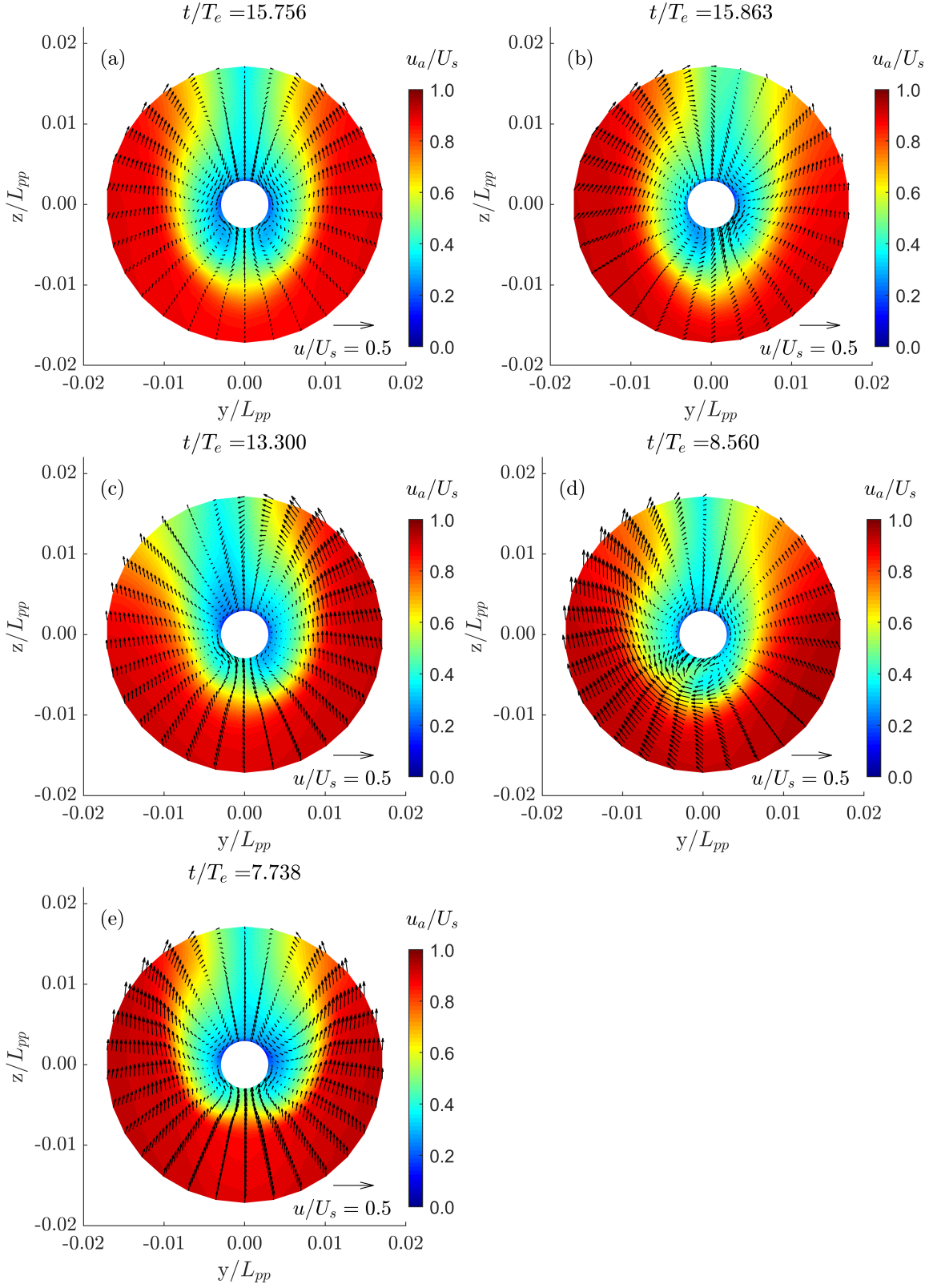


Figure 15: Animations of the transient wake fields in different wave headings over one encounter period. The arrows are the in-plane velocities. The start time of each animation is after each simulation reaches a periodic solution. The animations can be started by clicking on the figures or by using the following link: *Link is not available until published.* (a) Head sea waves; (b) Bow quartering sea waves; (c) Beam sea waves; (d) Stern quartering sea waves; (e) Following sea waves.

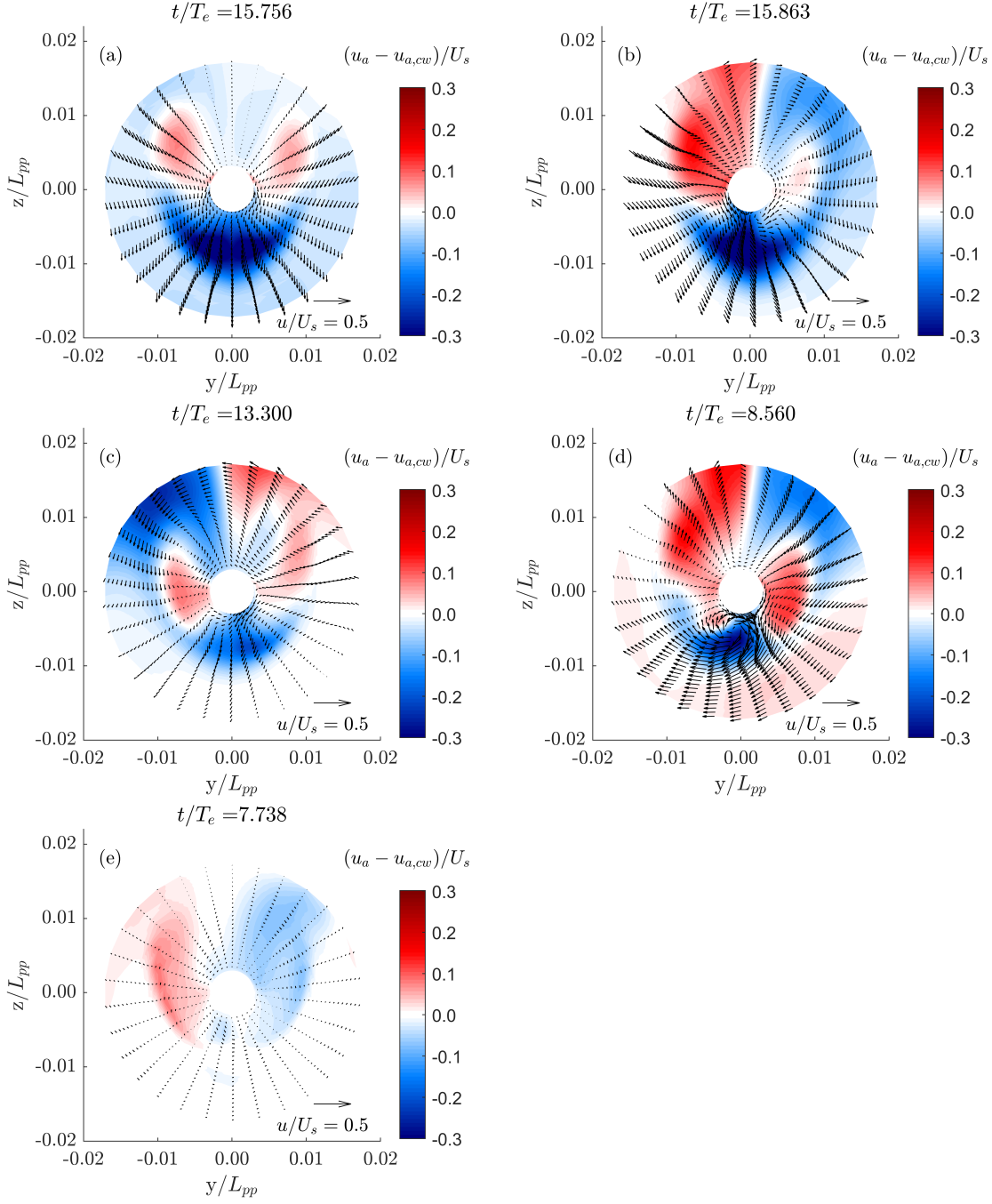


Figure 16: Animations of the transient nominal wake fields in waves relative to calm water. Positive value means that the axial velocity in this area is larger than in calm water. Arrows show the difference in the in-plane velocities relative to calm water.  $u$  is the velocity,  $u_a$  is the axial velocity,  $u_{a,cw}$  is the axial velocity in calm water and  $U_s$  is the ship speed. The start time of each animation is after each simulation reaches a periodic solution. The animations can be started by clicking on the figures or by using the following link: *Link is not available until published.* (a) Head sea waves; (b) Bow quartering sea waves; (c) Beam sea waves; (d) Stern quartering sea waves; (e) Following sea waves.

Table 5: Minimum and maximum  $\beta_t$  in the  $r/R = 0.7$  circle on the propeller disc.

	Min $\beta_t$	Max $\beta_t$	Difference in $\beta_t$
Calm water	8.4°	18.5°	10.1°
Port stern quartering sea waves	6.5°	20.1°	13.6°
Starboard stern quartering sea waves	6.4°	19.3°	12.9°

shadow behind the skeg. Furthermore, it can be seen the bilge vortex is oscillating from side to side. The animation seen in Fig. 15d shows that the port side bilge vortex is stronger than the starboard side bilge vortex. This makes the mean nominal wake field distribution asymmetric as seen in Fig. 13d.

### 3.3.5. RMS of velocity components

As seen in Fig. 15, the wake fields become transient in waves. In order to quantify the local variations in time, the Root-Mean-Square (RMS) and mean of each of the velocity components are calculated over one encounter period. The results for the stern quartering sea waves case is shown in Fig. 17. It is seen that the RMS values of the both the axial and tangential velocities are up to 15 % of the ship speed below the propeller hub. This is an indication that the propeller will experience a variation in angle of attack in this region over an encounter period. The RMS of the radial velocities are small. The RMS values are largest in the region where the bilge vortex is present. The movement of the bilge vortex over time for the stern quartering sea waves case is seen in Fig. 15d.

### 3.3.6. Modified advance angle

Even though the RMS and mean values of the velocity components provide an insight into the transient nominal wake field, it is challenging to relate these results to the operation and performance of the propeller. Therefore, the modified advance angle ( $\beta_t$ ) for a right handed propeller, which is defined in Eq. (21), is considered next.

Fig. 18 shows  $\beta_t$  for calm water and port and starboard stern quartering sea waves in the circle corresponding to  $r/R = 0.7$  on the propeller disc as function of time. A constant  $y$ -value on the plots is  $\beta_t$  in a given position over one encounter period. Please note that the propeller blade passing frequency is much higher than encounter frequency. Therefore, it is more relevant to follow a constant  $x$ -value, since it shows the  $\beta_t$  the propeller section will experience over the full  $r/R = 0.7$  circle at a specific time. As expected, the calm water results does not vary over time. The reason for the asymmetry of  $\beta_t$  around an angular position of 180 degrees is because the tangential velocity component included in  $\beta_t$

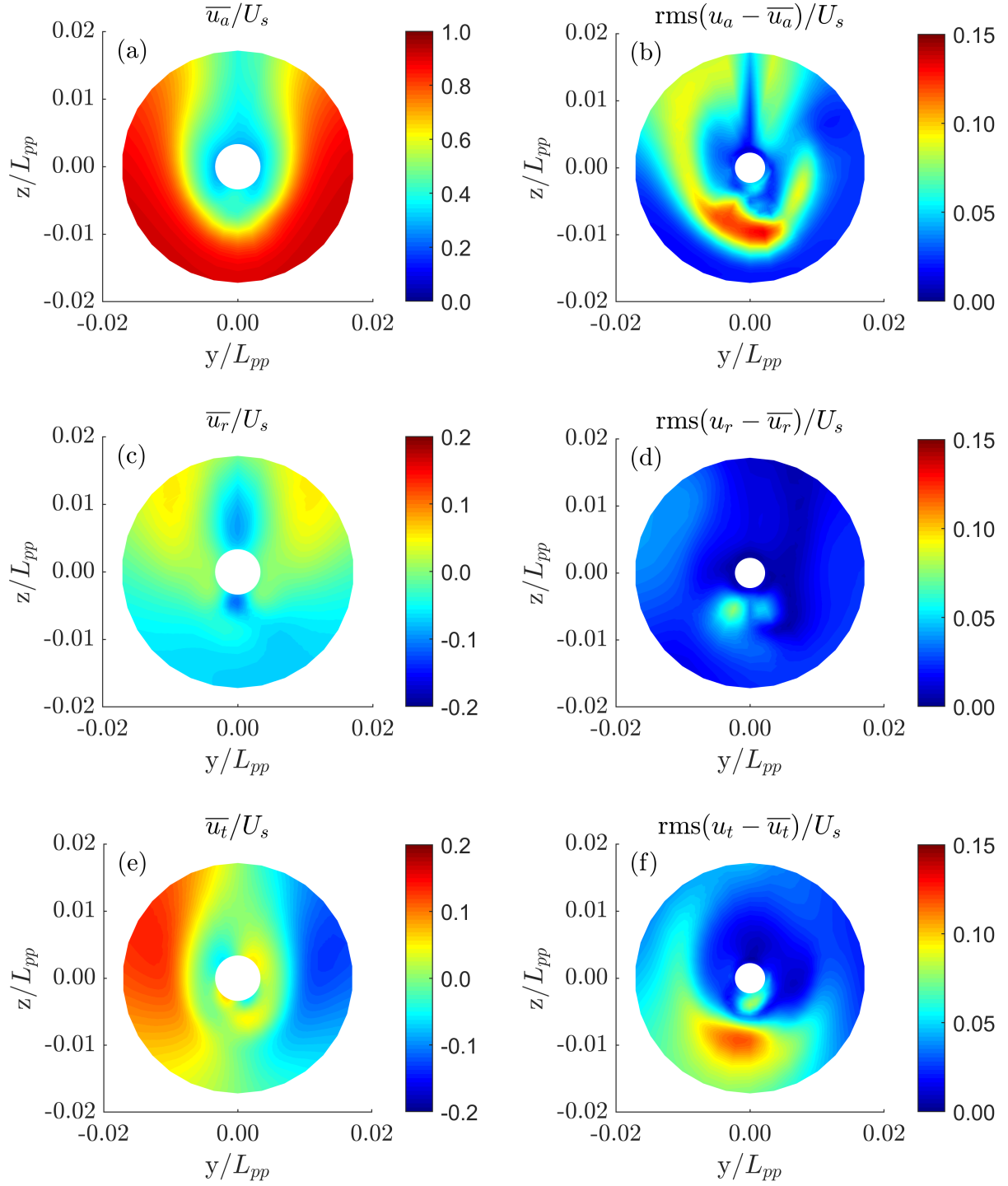


Figure 17: Distribution of mean and RMS of the components of non-dimensional velocity field for stern quartering sea waves. (a) Non-dimensional axial velocity; (b) RMS of non-dimensional axial velocity; (c) Non-dimensional radial velocity; (e) RMS of non-dimensional radial velocity; (e) Non-dimensional tangential velocity; (f) RMS of non-dimensional tangential velocity.

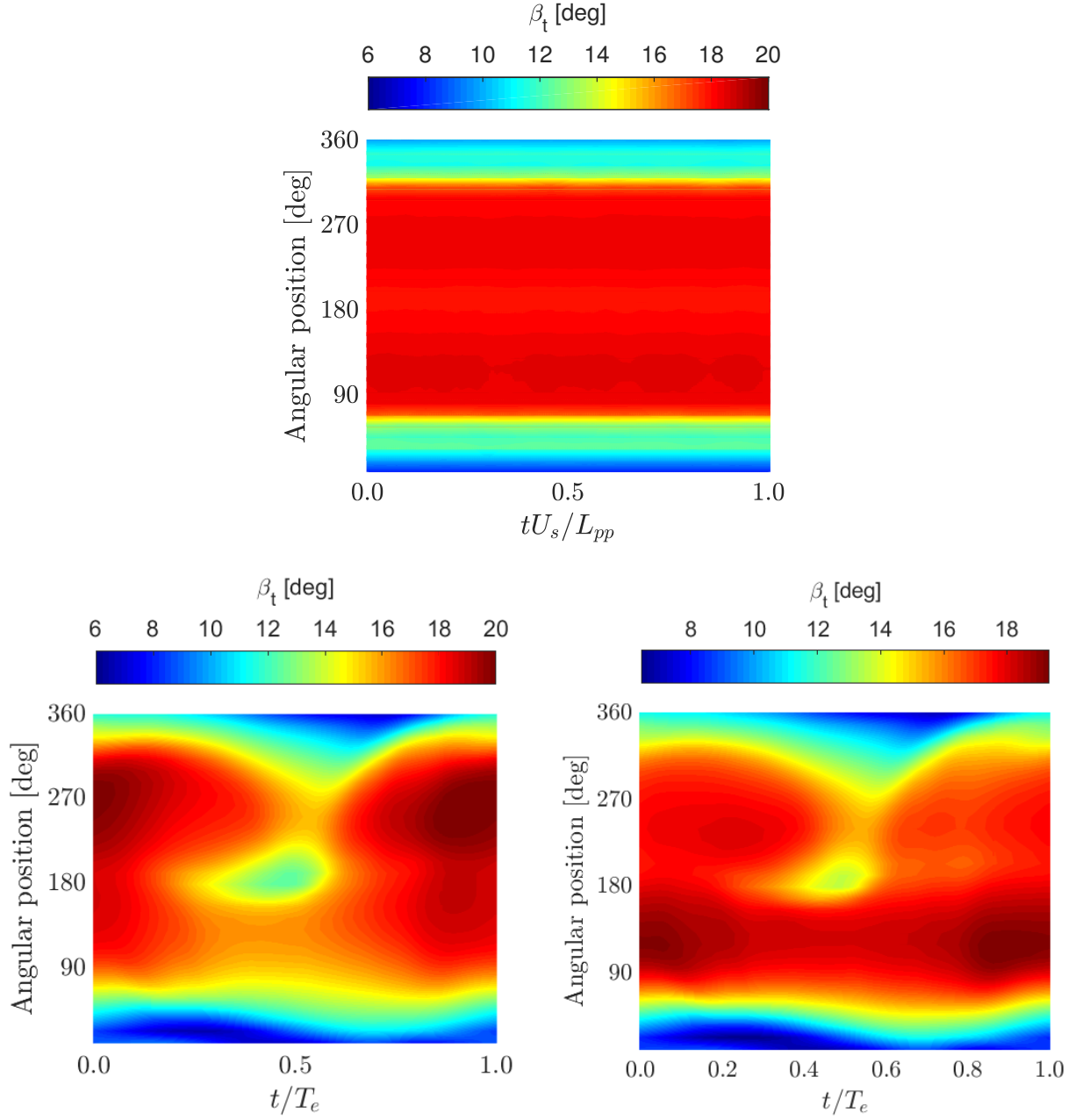


Figure 18: Modified advance angle ( $\beta_t$ ) at  $r/R = 0.7$  on the propeller disc over one encounter period. An angular position of 0/360 degrees correspond to a 12 o'clock position and 90 degrees correspond to a 3 o'clock position. Top: Calm water. Bottom left: Port stern quartering sea waves. Bottom right: Starboard stern quartering sea waves.



is asymmetric. This is illustrated in Fig. 17e, which shows the mean tangential velocities for the port stern quartering sea waves. For the starboard stern quartering sea waves, the tangential velocities will have opposite sign. The smallest  $\beta_t$  in calm water is found at 360 degrees corresponding to the 12 o'clock position. This is expected since this is the area with the lowest axial velocity as seen in Fig. 12a. This is traditionally the area with the highest likelihood for cavitation due to lowest axial velocities and lowest hydrostatic pressure from the water column. The difference between the minimum and maximum  $\beta_t$  over the  $r/R = 0.7$  circle in calm water is 10.1 degrees as seen in Table 5. The results for  $\beta_t$  in stern quartering sea waves are varying in time as seen in Fig. 18. The difference between the minimum and maximum  $\beta_t$  over the  $r/R = 0.7$  circle during the full encounter period for the port stern quartering sea waves is 13.6°, which is 3.5° more than in calm water. In starboard stern quartering sea waves, the difference in  $\beta_t$  over the  $r/R = 0.7$  circle during the full encounter period is 12.9°, which is 2.8° more than in calm water. The higher difference in  $\beta_t$  comes from both a higher maximum and lower minimum  $\beta_t$  in the stern quartering sea waves compared to calm water. A lower  $\beta_t$  will cause higher angle of attack resulting in lower pressure on the suction side of the propeller. In the stern quartering sea waves case, the water column and pressure is lowest at  $t/T_e = 0.5$  for all locations on the line through the 12/6 o'clock line in the propeller disc as seen in Fig. 19. This pressure variation, which is primarily caused by the varying water column above the propeller is important to consider, when assessing the cavitation behavior.

#### 4. Conclusion

The nominal wake fields of the KCS ship in regular waves with five different headings and a wavelength equal to the ship length have been studied using URANS CFD. The CFD setup was verified showing an estimated spatial and temporal discretization error of less than 2.5 %. A comparison of the nominal wake field in calm water and in head sea waves showed very good agreement between the present CFD results and experimental results from the literature. It was found that the nominal wake fraction fluctuated up to 39 % of the mean nominal wake fraction when sailing in waves. All headings except for head sea, had a mean nominal wake fraction higher than in calm water. The heading with maximum mean nominal wake fraction was the stern quartering sea, with a 16 % higher mean nominal wake fraction than in calm water. The motion responses did not show a significant influence on the mean wake fraction. It was found that the transient bilge vortex and shadow from the skeg have a significant influence on the nominal wake field. Finally, it was found that the modified advance angle on the  $r/R = 0.7$  circle in the propeller plane varies 3.5 degrees



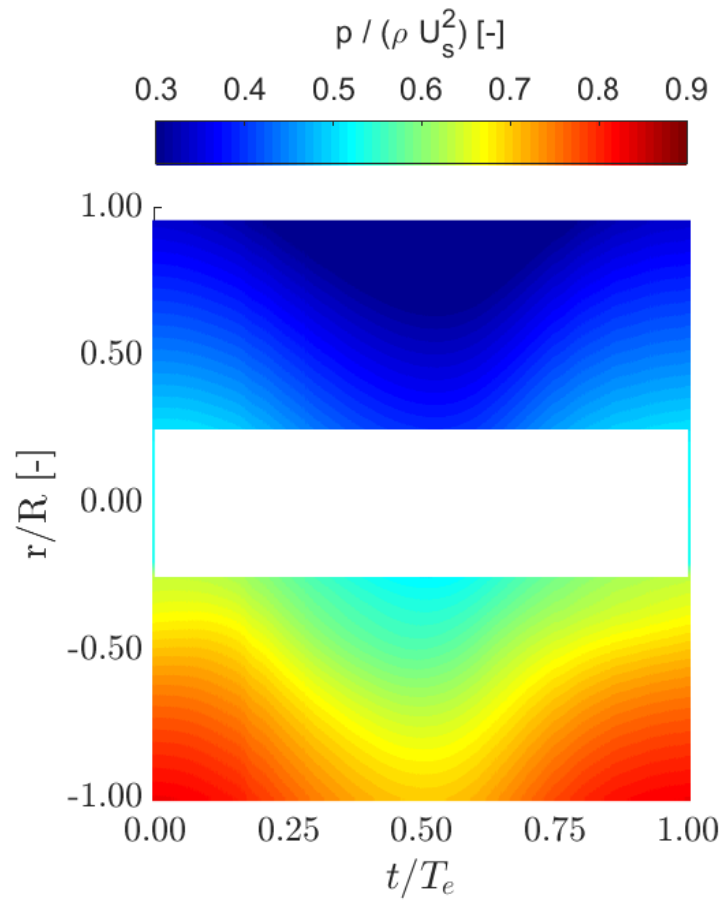


Figure 19: Non-dimensional pressure in the propeller disc through the 12/6 o'clock line over one encounter period ( $T_e$ ). The pressure is non-dimensionalized with the water density ( $\rho$ ) and ship speed ( $U_s$ ).

more in port stern quartering sea than in calm water, increasing the risk of cavitation.

The present study only considers a single wave length, ship speed, wave steepness and ship geometry. Therefore all results and conclusions are only valid for these. For future studies of the nominal wake field, it is proposed to vary the speed, wave steepness, wave length, and consider other ship geometries. It is expected that variations in these will significantly influence the nominal wake fields. Furthermore, irregular waves could be study. Finally, a next natural extension of the study, is to include propeller either using a propeller model or include the fully discretized propeller.

## 5. Acknowledgement

The research is supported by the Danish Maritime Fund under grant 2018-11, whose support is greatly appreciated. Many thanks to Mr. Wei Jin, Mr. Jens Ring Nielsen, and Dr. Keun Woo Shin from MAN Energy Solutions for providing insight as propeller designers. Special thanks to Dr. Eivind Ruth and Mr. Tormod Gjestland from DNV (formerly DNV GL) for the valuable input in our discussions.

## References

- Carlton, J. (2012). *Marine Propellers and Propulsion* (3 ed.). Butterworth-Heinemann.
- Celik, I. B., U. Ghia, P. J. Roache, C. J. Freitas, H. Coleman, and P. E. Raad (2008). Procedure for estimation and reporting of uncertainty due to discretization in CFD applications. *J. Fluids Engng.* 130, 1–4.
- Chuang, Z. and S. Steen (2013). Speed loss of a vessel sailing in oblique waves. *Ocean Engng.* 64, 88–99.
- Ferziger, J. H. and M. Peric (2002). *Computational methods for fluid dynamics* (3 ed.). Cambridge University Press.
- FORCE (2013). Experimental data for appended kcs hull in deep water. Technical report, Technical report, Data gathered by FORCE Technology for the SIMMAN2014 workshop on ship manouvering.
- Fujii, H. and T. Takahashi (1975). Experimental study on the resistance increase of a large full ship in regular oblique waves. *J. Soc. Nav. Archit. Japan* 137, 132–137.
- Gaggero, S., D. Villa, and M. Viviani (2017). An extensive analysis of numerical ship self-propulsion prediction via a coupled BEM/RANS approach. *Appl. Ocean Research* 66, 55–78.
- Gong, J., S. Yan, Q. Ma, and Y. Li (2020). Added resistance and seakeeping performance of trimarans in oblique waves. *Ocean Engng.* 216, 1–19.
- Hino, T., F. Stern, L. Larsson, M. Visonneau, N. Hirakata, and J. Kim (2020). *Numerical ship hydrodynamics: An assessment of the Tokyo 2015 workshop*. Springer-Verlag.
- Hirt, C. W. and B. D. Nichols (1981). Volume of fluid (VOF) method for the dynamics of free boundaries. *J. Comput. Phys.* 39(1), 201–225.
- Kim, D.-h., Y. Sanada, H. Sadat-hosseini, and F. Stern (2021). URANS simulations for a free-running container ship : Part 2 . Added power \*. *J. Hydrodyn.* 33, 448–467.

- Kim, D.-H., Y. Sanada, H. Sadat-Hosseini, and F. Stern (2021). URANS simulations for a free-running container ship: Part 2. Added power \*. *J. Hydrodyn.* 33(3), 448–467.
- Longo, J., J. Shao, M. Irvine, and F. Stern (2007). Phase-averaged PIV for the nominal wake of a surface ship in regular head waves. *J. Fluids Engng.* 129(5), 524–540.
- Menter, F. R. (1993). Zonal two equation  $k$ - $\omega$  turbulence models for aerodynamic flows. *AIAA J.* Paper 93-2906.
- Mikkelsen, H., M. L. Steffensen, C. Ciortan, and J. H. Walther (2019). Ship scale validation of CFD model of self-propelled ship. In *MARINE 2019 Computational Methods in Marine Engineering VIII*, pp. 718–729.
- Mikkelsen, H. and J. H. Walther (2020). Effect of roughness in full-scale validation of a CFD model of self-propelled ships. *Appl. Ocean Research* 99, 1–14.
- Mikkelsen, H., S. Y., and J. H. Walther (2021). CFD verification and validation of added resistance and seakeeping response in regular oblique waves with varying wave length. In *MARINE 2021 Computational Methods in Marine Engineering IX*.
- Muzaferija, S. and M. Perić (1997). Computation of free-surface flows using the finite-volume method and moving grids. *Num. Heat Trans., B* 32(4), 369–384.
- Regener, P. B., Y. Mirsadraee, and P. Andersen (2018). Nominal vs. effective wake fields and their influence on propeller cavitation performance. *J. Mar. Sci. Eng.* 6(2), 1–14.
- Richardson, L. F. (1910). The approximate arithmetical solution by finite differences of physical problems involving differential equations, with an application to the stresses in a masonry dam. *Phil. Trans. R. Soc. A* 210, 307–357.
- Richardson, L. F. and J. A. Gaunt (1927). The deferred approach to the limit. Part I. Single lattice. Part II. Interpenetrating lattices. *Phil. Trans. R. Soc. A* 226, 299–361.
- Roache, P. J. (1998). Verification of codes and calculations. *AIAA J.* 36(5), 696–702.
- Sadat-Hosseini, H., S. Toxopeus, D. H. Kim, Y. Sanada, M. Stocker, J. F. Otzen, Y. Toda, and F. Stern (2015). Experiments and computations for KCS added resistance for variable heading. In *5th World Maritime Technology Conference*, pp. 1–15.
- Saettone, S., B. Taskar, P. B. Regener, S. Steen, and P. Andersen (2020). A comparison between fully-unsteady and quasi-steady approach for the prediction of the propeller performance in waves: Prediction of the propeller performance in waves. *Appl. Ocean Research* 99, 1–16.
- Saettone, S., B. Taskar, S. Steen, and P. Andersen (2021). Experimental measurements of propulsive factors in following and head waves. *Appl. Ocean Research* 111, 1–12.
- Sanada, Y., D. H. Kim, H. Sadat-Hosseini, Y. Toda, C. Simonsen, and F. Stern (2018, August). Experiment and numerical simulation for KCS added powering in regular head/oblique waves. In *32nd Symposium on Naval Hydrodynamics*, pp. 1–30.
- Shigunov, V., O. el Moctar, A. Papanikolaou, R. Potthoff, and S. Liu (2018). International benchmark study on numerical simulation methods for prediction of manoeuvrability of ships in waves. *Ocean Engng.* 165, 365–385.
- Shih, T.-H., W. W. Liou, A. Shabbir, Z. Yang, and J. Zhu (1995). A new  $k$ - $\epsilon$  eddy viscosity model for high Reynolds number turbulent flows. *Computers & Fluids* 24(3), 227–238.
- Siemens (2020). STAR-CCM+ user guide, version 2020.1.
- Sprenger, F., A. Maron, G. Delefortrie, T. V. Zwijsvoorde, A. Cura-Hochbaum, A. Lengwinat, and A. Papanikolaou (2017). Experimental studies on seakeeping and maneuverability of ships in adverse weather conditions. *J. Ship. Res.* 61(3), 131–152.

- Stern, F., H. Sadat-Hosseini, T. Dogan, M. Diez, D. H. Kim, S. Park, and Y. Sanada (2021). *Assessment of CFD for KCS added resistance and for ONRT course keeping/speed loss in regular head and oblique waves*, Volume 94. Springer International Publishing.
- Valanto, P. and Y. P. Hong (2015). Experimental investigation on ship wave added resistance in regular head, oblique, beam, and following waves. In *Proceedings of the International Offshore and Polar Engineering Conference*, pp. 19–26.
- Wilcox, D. C. (1998). *Turbulence modeling for CFD* (2 ed.). DWC Industries.
- Wu, P.-C., M. A. Hossain, N. Kawakami, K. Tamaki, H. A. Kyaw, A. Matsumoto, and Y. Toda (2020). EFD and CFD study of forces, ship motions, and flow field for KRISO container ship model in waves. *J. Ship. Res.* 64(1), 61–80.



## Chapter 5

# Conclusions and future work

This chapter is partially based on the three papers presented in this thesis.

### 5.1 Conclusions

The work presented in the thesis have developed, verified and validated accurate numerical models that can help ship designers narrow a part of the gap between the the conditions ships are designed for and the conditions the ships will operate in. The main body of the thesis consisted of three papers. The first paper presented a comparison of towing tank results and full-scale self-propulsion CFD simulations with free surface and rotating propeller and full-scale measurements from the speed trials of the six sister vessels. The scatter of the speed trials was small with most of the measurements within 3 % of the mean curve. The towing tank prediction of the delivered power in full-scale was within 1 % of the speed trial for all speeds. Due to this excellent accuracy of the towing tank prediction, the towing tank measurements and predictions were used to validate the CFD set-up in systematic steps. The discrepancies for resistance, propeller open-water and model scale self-propulsion CFD simulations were found to be within the model test uncertainty. However, for the full-scale self-propulsion simulation, the delivered power from CFD was underestimated with 8–12 % compared to the speed trial measurements when the roughness was estimated using the standard empirical formula by Townsin and Mosaad (1985) and applied as a point force in the center of gravity. By including a roughness model directly into the self-propulsion simulation using a modifying wall function approach, the discrepancy was significantly reduced. The same conclusions were found for a general cargo vessel where the geometry and speed trial data are publicly available. Unfortunately, the exact roughness of the surface of the two vessels was unknown. Based on a literature study on roughness measurements on newly painted ships, a range of sand-grain equivalent roughness heights of 100–150  $\mu\text{m}$  was tested for both vessels resulting in significantly reduced discrepancies to the speed trial measurements for both cases. This indicates that using a roughness model directly into the CFD simulation is more accurate than the traditional method using empirical formulas designed for towing tanks.

Most ships are designed for sailing in calm water, even though almost no ships sail entirely in calm water. Before numerical simulations can be used to predict seakeeping responses and added resistance in waves, a systematic verification and validation is required to ensure accuracy. The second paper in this thesis presented this for the KCS container ship in regular oblique waves by using a CFD approach with turbulence modelling. Convergence studies of both the temporal and spatial discretization errors were presented. Discussions were made to determine affordable time steps and mesh sizes while to keep the discretization errors acceptable. The yaw and surge motions were constrained by user-implementations in the commercial software, which consist of additions of springs and concentrated forces/moment to cancel the fluid forces and moments. The mesh and time step convergence studies showed that the sum of the spatial and temporal

discretization errors for an affordable calculation were less than 5 %, which is smaller than the average standard deviation of the experiments from the literature. A study of the empty wave tank showed that the wave generation was successful, but caused the loss of incident wave amplitude due to numerical diffusion of less than 4 % for most test cases. 28 test cases were studied with different combinations of wave heading and wavelength. For each test case, the added resistance as well as the heave, pitch, and roll response were compared with previously reported potential flow and CFD results and up to three sets of experimental data. Due to the loss of incident wave amplitude caused by numerical diffusion, the motion and added resistance results were non-dimensionalized based on the actual incident wave amplitude obtained from separate runs in empty wave tank, where similar spatial and temporal discretization was used. In most cases the discrepancy between the experiments and the present CFD results were within the uncertainty of the experiments. In some cases, especially in stern quartering and following sea, the experimental uncertainties were significant. If experiments with smaller uncertainties become available, a better validation would be possible. It was found that the present CFD results in general had better agreement with the experiments than what previous reported CFD results had. In general, both the previously reported potential flow results and the present CFD results predicted the motion responses well. However, the added resistance predicted by the present CFD model was in better agreement with the experiments, than the potential flow results. The tendencies in the results of the present CFD model matched very well the expected behaviour regarding the natural motion frequencies of the ship.

The third paper presented in this thesis used the verified and validated CFD set-up from the second paper to study the nominal wake fields of the KCS ship in regular waves with five different headings and a wavelength equal to the ship length. The CFD setup was verified for the nominal wake fraction showing an estimated spatial and temporal discretization error of less than 2.5 %. A comparison of the nominal wake field in calm water and in head sea waves showed very good agreement between the present CFD results and experimental results from the literature. It was found that the nominal wake fraction fluctuated up to 39 % of the mean nominal wake fraction when sailing in waves. All headings except for head sea, had a mean nominal wake fraction higher than in calm water. The heading with maximum mean nominal wake fraction was the stern quartering sea, with a 16 % higher mean nominal wake fraction than in calm water. The motion responses did not show a significant influence on the mean wake fraction. It was found that the transient bilge vortex and shadow from the skeg have a significant influence on the nominal wake field. Finally, it was found that the modified advance angle on the  $r/R = 0.7$  circle in the propeller plane varies 3.5 degrees more in stern quartering sea than in calm water, increasing the risk of cavitation potentially leading to vibrations and loss of propulsive efficiency.

All three papers showed that high accuracy could be achieved, when the CFD simulations were set-up very carefully and systematic verification and validation were conducted. The results from the three papers showed that numerical simulations have a massive potential as useful tools when designing ships for the conditions, the ship will operate in.

## 5.2 Future work

Inclusion of full-scale effects, surface roughness, and waves only narrows a part of the gap between the conditions ships are designed for and the conditions the ships will operate in. For future full-scale validation studies, it is recommended to measure the hull and propeller roughness of the ship at different locations right before the speed trial. Furthermore, it would be ideal if all data of the future full-scale validation study including geometries and speed trial data would be publicly available. In this way, multiple codes and approaches could be tested and validated. For future studies related to the wave simulations, it is proposed to vary the wave steepness, wave length, and consider other ship geometries. Furthermore, irregular waves

could be study. Finally, a next natural extension of the study, is to include propeller either using a propeller model or include the fully discretized propeller.





# Bibliography

- Adams, T., C. Grant, and H. Watson (2012). A simple algorithm to relate measured surface roughness to equivalent sand-grain roughness. *Int. J. Mech. Eng. Mechatronics* 1(1), 66–71.
- Bowden, B. S. and N. J. Davison (1974). Resistance increments due to hull roughness associated with form factor extrapolation methods. *Natl. Phys. Lab. Sh. Tech. Man.* 3800, –.
- Carlton, J. (2012). *Marine Propellers and Propulsion* (3 ed.). Butterworth–Heinemann.
- Cebeci, T. and P. Bradshaw (1977). *Momentum transfer in boundary layers*. Hemisphere Publishing Corporation/McGraw-Hill.
- Chuang, Z. and S. Steen (2013). Speed loss of a vessel sailing in oblique waves. *Ocean Engng.* 64, 88–99.
- Clauser, F. H. (1954). Turbulent boundary layers in adverse pressure gradients. *J. Aeronaut. Sci.* 21(2), 91–108.
- Demirel, Y. K., O. Turan, and A. Incecik (2017). Predicting the effect of biofouling on ship resistance using CFD. *Appl. Ocean Research* 62, 100–118.
- Faltinsen, O. (1993). *Sea Loads on Ships and Offshore Structures*. Cambridge University Press.
- Ferziger, J. H. and M. Peric (2002). *Computational methods for fluid dynamics* (3 ed.). Cambridge University Press.
- Fujii, H. and T. Takahashi (1975). Experimental study on the resistance increase of a large full ship in regular oblique waves. *J. Soc. Nav. Archit. Japan* 137, 132–137.
- Gong, J., S. Yan, Q. Ma, and Y. Li (2020). Added resistance and seakeeping performance of trimarans in oblique waves. *Ocean Engng.* 216, 1–19.
- Hino, T., F. Stern, L. Larsson, M. Visonneau, N. Hirakata, and J. Kim (2020). *Numerical ship hydrodynamics: An assessment of the Tokyo 2015 workshop*. Springer-Verlag.
- Hirt, C. W. and B. D. Nichols (1981). Volume of fluid (VOF) method for the dynamics of free boundaries. *J. Comput. Phys.* 39(1), 201–225.
- Howell, D. and B. Behrends (2006). A review of surface roughness in antifouling coatings illustrating the importance of cutoff length. *Biofouling* 22(6), 401–410.
- IMO (2011). Amendments to marpol annex vi on regulations for the prevention of air pollution from ships by inclusion of new regulations on energy efficiency for ships, MEPC 62/24/Add.1, Annex 19. Technical report.
- ITTC (2008). 1978 ITTC - Performance prediction method. ITTC - Recommended procedures and guidelines, Procedure 7.5-02-03-01.4, Revision 01. Technical report.

- ITTC (2017). The propulsion committee - Final report and recommendations to the 28th ITTC. Technical report.
- ITTC (2021). ITTC recommended procedures and guidelines, 1978 ITTC performance prediction method. Technical report.
- Jin, Y., S. Chai, J. Duffy, C. Chin, and N. Bose (2017). URANS predictions of wave induced loads and motions on ships in regular head and oblique waves at zero forward speed. *J. Fluids Struct.* 74, 178–204.
- Kim, D.-H., Y. Sanada, H. Sadat-Hosseini, and F. Stern (2021). URANS simulations for a free-running container ship: Part 2. Added power \*. *J. Hydrodyn.* 33(3), 448–467.
- Kim, J., I.-R. Park, K.-S. Kim, and S.-H. Van (2005). Numerical simulation of turbulent free surface flow around a self-propelled ship. In *Proc. Fifteenth Int. Offshore Polar Eng. Conf.*, pp. 180–186.
- Kim, M., O. Hizir, O. Turan, S. Day, and A. Incecik (2017). Estimation of added resistance and ship speed loss in a seaway. *Ocean Engng.* 141, 465–476.
- Kim, M., O. Hizir, O. Turan, and A. Incecik (2017). Numerical studies on added resistance and motions of KVLCC2 in head seas for various ship speeds. *Ocean Engng.* 140(May), 466–476.
- Kim, Y., K.-H. Kim, J.-H. Kim, T. Kim, M.-G. Seo, and Y. Kim (2011). Time-domain analysis of nonlinear motion responses and structural loads on ships and offshore structures: development of WISH programs. *Int. J. Nav. Archit. Ocean Eng.* 3(1), 37–52.
- Larsson, L., F. Stern, and M. Visonneau (2010). Proceedings of Gothenburg 2010 - A workshop on numerical ship hydrodynamics.
- Larsson, L., F. Stern, M. Visonneau, T. Hino, N. Hirata, and J. Kim (2015). Proceedings of Tokyo 2015 workshop on CFD in ship hydrodynamics.
- Leer-Andersen, M. and L. Larsson (2003). An experimental/numerical approach for evaluating skin friction on full-scale ships with surface roughness. *J. Mar. Sci. Tech.* 8(1), 26–36.
- Lindholdt, A., K. Dam-Johansen, S. M. Olsen, D. M. Yebra, and S. Kiil (2015). Effects of biofouling development on drag forces of hull coatings for ocean-going ships: a review. *J. Coatings Technol. Res.* 12(3), 415–444.
- Liu, C., J. Wang, and D. Wan (2018). CFD computation of wave forces and motions of DTC ship in oblique waves. *J. Offshore Pol. Eng.* 28(2), 154–163.
- Liu, S. and A. Papanikolaou (2016). Prediction of the added resistance of ships in oblique seas. In *Proceedings of the International Offshore and Polar Engineering Conference*, pp. 495–502.
- Longo, J., J. Shao, M. Irvine, and F. Stern (2007). Phase-averaged PIV for the nominal wake of a surface ship in regular head waves. *J. Fluids Engng.* 129(5), 524–540.
- Molland, A., S. Turnock, and D. Hudson (2011). *Ship resistance and propulsion*. Cambridge University Press.
- Mousavi, S. M., A. R. Khoogar, and H. Ghasemi (2020). Time domain simulation of ship motion in irregular oblique waves. *J. Appl. Fluid Mech.* 13(2), 549–559.
- Muzaferija, S. and M. Perić (1997). Computation of free-surface flows using the finite-volume method and moving grids. *Num. Heat Trans., B* 32(4), 369–384.

- Niebles Atencio, B. and V. Chernoray (2019). A resolved RANS CFD approach for drag characterization of antifouling paints. *Ocean Engng.* 171, 519–532.
- Nikuradse, J. (1933). Stromungsgesetze in rauhen rohren. *Forsch. Arb. Ing.-Wes.*, 361. *English Transl. as NACA-TM-1292*.
- Owen, D., Y. K. Demirel, E. Oguz, T. Tezdogan, and A. Incecik (2018). Investigating the effect of biofouling on propeller characteristics using CFD. *Ocean Engng.* 159, 505–516.
- Park, D. M., Y. Kim, M. G. Seo, and J. Lee (2016). Study on added resistance of a tanker in head waves at different drafts. *Ocean Engng.* 111, 569–581.
- Park, D.-M., J.-H. Lee, Y.-W. Jung, J. Lee, Y. Kim, and F. Gerhardt (2019). Experimental and numerical studies on added resistance of ship in oblique sea conditions. *Ocean Engng.* 186, 106070.
- Pérez Arribas, F. (2007). Some methods to obtain the added resistance of a ship advancing in waves. *Ocean Engng.* 34(7), 946–955.
- Ponkratov, D. (2017). Proceedings of 2016 workshop on ship scale hydrodynamic computer simulation. Lloyd’s Register.
- Psaraftis, H. N. and C. A. Kontovas (2014). Ship speed optimization: Concepts, models and combined speed-routing scenarios. *Transp. Res. Part C Emerg. Technol.* 44, 52–69.
- Regener, P. B., Y. Mirsadraee, and P. Andersen (2018). Nominal vs. effective wake fields and their influence on propeller cavitation performance. *J. Mar. Sci. Eng.* 6(2), 1–14.
- Sadat-Hosseini, H., S. Toxopeus, D. H. Kim, Y. Sanada, M. Stocker, J. F. Otzen, Y. Toda, and F. Stern (2015). Experiments and computations for KCS added resistance for variable heading. In *5th World Maritime Technology Conference*, pp. 1–15.
- Sadat-Hosseini, H., P. C. Wu, P. M. Carrica, H. Kim, Y. Toda, and F. Stern (2013). CFD verification and validation of added resistance and motions of KVLCC2 with fixed and free surge in short and long head waves. *Ocean Engng.* 59, 240–273.
- Saettone, S., B. Taskar, P. B. Regener, S. Steen, and P. Andersen (2020). A comparison between fully-unsteady and quasi-steady approach for the prediction of the propeller performance in waves: Prediction of the propeller performance in waves. *Appl. Ocean Research* 99, 1–16.
- Saettone, S., B. Taskar, S. Steen, and P. Andersen (2021). Experimental measurements of propulsive factors in following and head waves. *Appl. Ocean Research* 111, 1–12.
- Salvesen, N., E. Tuck, and O. Faltinsen (1970). Ship motions and sea loads. *Trans. - Soc. Nav. Archit. Mar. Eng.* 78, 250–287.
- Sanada, Y., D. H. Kim, H. Sadat-Hosseini, Y. Toda, C. Simonsen, and F. Stern (2018, August). Experiment and numerical simulation for KCS added powering in regular head/oblique waves. In *32nd Symposium on Naval Hydrodynamics*, pp. 1–30.
- Schultz, M. P. (2004). Frictional resistance of antifouling coating systems. *J. Fluids Engng.* 126(6), 1039–1047.
- Schultz, M. P. (2007). Effects of coating roughness and biofouling on ship resistance and powering. *Biofouling* 23, 331–341.
- Schultz, M. P. and K. A. Flack (2017). The rough-wall turbulent boundary layer from the hydraulically smooth to the fully rough regime. *J. Fluid Mech.* 580, 381–405.

- Schultz, M. P., J. M. Walker, C. N. Steppe, and K. A. Flack (2015). Impact of diatomaceous biofilms on the frictional drag of fouling-release coatings. *Biofouling* 31, 759–773.
- Shih, T.-H., W. W. Liou, A. Shabbir, Z. Yang, and J. Zhu (1995). A new  $k$ - $\epsilon$  eddy viscosity model for high Reynolds number turbulent flows. *Computers & Fluids* 24(3), 227–238.
- Siemens (2020). STAR-CCM+ user guide, version 2020.1.
- Simonsen, C. D., J. F. Otzen, S. Joncquez, and F. Stern (2013). EFD and CFD for KCS heaving and pitching in regular head waves. *J. Mar. Sci. Tech.* 18, 435–459.
- Song, S., Y. K. Demirel, and M. Atlar (2019). An investigation into the effect of biofouling on the ship hydrodynamic characteristics using CFD. *Ocean Engng.* 175, 122–137.
- Song, S., Y. K. Demirel, and M. Atlar (2020). Penalty of hull and propeller fouling on ship self-propulsion performance. *Appl. Ocean Research* 94, 102006.
- Song, S., Y. K. Demirel, M. Atlar, and O. Turan (2019). Validation of the CFD approach for modelling roughness effect on ship resistance. In *6th Int. Conf. Adv. Model Meas. Technol. Marit. Ind.*
- Sprenger, F., V. Hassani, A. Maron, G. Delefortrie, T. V. Zwijnsvoorde, A. Cura-Hochbaum, and A. Lengwinat (2016). Establishment of a validation and benchmark database for the assessment of ship operation in adverse conditions. In *35th International Conference on Ocean, Offshore and Arctic Engineering*, pp. 1–12.
- Storm-Tejse, J., H. Y. H. Yeh, and D. D. Moran (1973). Added resistance in waves. *Trans. - Soc. Nav. Archit. Mar. Eng.* 81, 250–279.
- Townsin, R. L. and M. A. Mosaad (1985). The ITTC line – its genesis and correlation allowance. *Nav. Archit.*
- UNCTAD (2019). Review of Maritime Transport 2019. Technical report, United Nations Conference on Trade and Development.
- Usta, O. and E. Korkut (2013). A study for the effect of surface roughness on resistance characteristics of flat plates. In *Marine Coatings*, pp. 29–37. Royal Institution of Naval Architects.
- Utama, I. K. A. P., B. Nugroho, C. Chin, M. L. Hakim, F. A. Prasetyo, M. Yusuf, I. K. Suastika, J. Monty, and N. Hutchins (2017). A study of skin friction-drag from realistic roughness of a freshly cleaned and painted ship hull. In *Proc. Int. Symp. Mar. Eng.*
- Valanto, P. and Y. P. Hong (2015). Experimental investigation on ship wave added resistance in regular head, oblique, beam, and following waves. In *Proceedings of the International Offshore and Polar Engineering Conference*, pp. 19–26.
- Vukcevic, V. and H. Jasak (2016). Validation and verification of decomposition model based on embedded free surface method for oblique wave seakeeping simulations. In *Tokyo 2015: A Workshop on CFD in Ship Hydrodynamics*, pp. 495–502.
- Wilcox, D. C. (1998). *Turbulence modeling for CFD* (2 ed.). DWC Industries.
- Wu, P.-C., M. A. Hossain, N. Kawakami, K. Tamaki, H. A. Kyaw, A. Matsumoto, and Y. Toda (2020). EFD and CFD study of forces, ship motions, and flow field for KRISO container ship model in waves. *J. Ship. Res.* 64(1), 61–80.

- Yang, Y., R. Zhu, and L. Hong (2019). A frequency-domain hybrid HOBEM for motion responses and added resistance of ships sailing in head and oblique waves. *Ocean Engng.* 194, 1–16.







DTU Mechanical Engineering  
Section of Fluid Mechanics, Coastal and Maritime Engineering  
Technical University of Denmark

Nils Koppels Allé, Bld. 403  
DK-2800 Kgs. Lyngby  
Denmark  
Tlf.: +45 4525 1360  
Fax: +45 4525 1961

[www.mek.dtu.dk](http://www.mek.dtu.dk)

December 2021

ISBN: 978-87-7475-667-5

**DCAMM**  
**Danish Center for Applied Mathematics**  
**and Mechanics**

Nils Koppels Allé, Bld. 404  
DK-2800 Kgs. Lyngby  
Denmark  
Phone (+45) 4525 4250  
Fax (+45) 4525 1961

[www.dcammm.dk](http://www.dcammm.dk)

DCAMM Special Report No. S304

ISSN: 0903-1685